U.PORTO
FEUP FACULDADE DE ENGENHARIA
UNIVERSIDADE DO PORTO

University of Porto

Faculty of Engineering

Computational study of atmospheric flows over Perdigão: terrain resolution and domain size

Carlos Alberto Madureira da Silva

MSc in Mechanical Engineering

Supervisor: Prof. José Laginha Palma

Dissertation submitted to the University of Porto
in partial satisfaction of the requirements for the
degree of Master in Mechanical Engineering.

June 2018

Contact information:
Carlos Silva
email: up201302901@fe.up.pt

Abstract

The computational modelling of atmospheric flows depends on the terrain and land cover description, so it is important to quantify the errors associated with the digital terrain model (DTM), the resolution of the numerical mesh, and the impact of these parameters on the numerical results of the flow field. In the case of Perdigão, an aerial survey was made using LiDAR technology to produce a high resolution DTM (HRMap), motivating the definition of the spatial requirements for the computational model of the area.

HRMap was compared with a version of the Shuttle Radar Topography Mission (SRTM), a public domain DTM, with different mesh resolutions (80×80, 40×40, 20×20 m and 10×10 m). By means of a basic statistical analysis, the impact of the DTM and the resolution was quantified in the elevation and slope values of the terrain. Land cover information was also obtained from the LiDAR data and through Corine Land Cover to produce a variable roughness map and inclusion of a canopy model. The impact of the DTM, mesh resolution and surface cover model was evaluated in the horizontal velocity, direction and turbulent kinetic energy of the flow.

The SRTM is limited to a resolution of 30 m and it did not bring advantages when used with higher resolution meshes, so it is recommended to use HRMap for future works. Only HRMap-based meshes were able to reproduce the high frequency content in a spectral analysis. With a 40×40 m mesh based on the HRMap, an elevation error of less than 1 m was achieved at five reference points and a RMSE of less than 1.5 m, whereas with the SRTM the RMSE was not lower than 4 m. The maximum and minimum slope were about twice as high with a resolution of 20×20 m, when compared to a resolution of 80×80 m. A 40×40 m resolution based on HRMap was enough to represent the terrain accurately.

Flow patterns showed that, near the valley's surface, the flow is approximately perpendicular to the prevailing wind directions in the area. Wind direction was the less sensitive variable to DTM and mesh refinement. For southwesterly winds, mesh refinement led to a decrease in horizontal velocity and increase in turbulent kinetic energy. The impact of the DTM was greater at higher resolutions. In locations affected by the complexity of valley flow (Tower 25 and 29), the response to mesh refinements for different DTMs was different, diverging with the SRTM and stabilizing with the HRMap. For northeasterly winds, Tower 37 showed differences of 2 $m\ s^{-1}$ in horizontal velocity and 0.5 $m^2\ s^{-2}$ in turbulent kinetic energy, when using HRMap instead of SRTM.

Resumo

A modelação computational de escoamentos atmosféricos depende da descrição do terreno e da sua cobertura, logo é importante quantificar os erros associados ao modelo digital de terreno (DTM), à resolução da malha numérica, e o impacto destes parâmetros nos resultados numéricos do escoamento. No caso de Perdigão, foi feito um levantamento aéreo com recurso a tecnologia LiDAR para a produção de um DTM de elevada resolução (HRMap), motivando a definição dos requisitos espaciais para o modelo computacional da área.

Comparou-se o HRMap com uma versão do Shuttle Radar Topography Mission (SRTM), um DTM de domínio público, com diferentes resoluções de malha (80×80, 40×40, 20×20 m e 10×10 m). Através de uma análise estatística básica, quantificou-se o impacto do DTM e da resolução nos valores da elevação e inclinação do terreno. Informação de cobertura do terreno foi também obtida pelos dados do LiDAR e através do Corine Land Cover para produção de um mapa de rugosidade variável e inclusão de um modelo de canópia. O impacto do DTM, resolução da malha e cobertura do terreno foi avaliada na velocidade horizontal, direção e energia cinética turbulenta do escoamento.

O SRTM está limitado a uma resolução de 30 m e não trouxe vantagens quando utilizado com malhas de resolução mais elevada, portanto recomenda-se a utilização do HRMap para trabalhos futuros. Apenas malhas baseadas no HRMap conseguiram reproduzir, numa análise espetral, o conteúdo de alta frequência. Com uma malha de 40 ×40 m baseada no HRMap alcançou-se um erro de elevação inferior a 1 m em cinco pontos de referência e um RMSE inferior a 1.5 m, enquanto que com o SRTM o RMSE não foi inferior a 4 m. A inclinação máxima e mínima foi cerca de duas vezes maior com uma resolução de 20×20 m, quando comparada com uma resolução de 80×80 m. Uma resolução de 40×40 m baseada no HRMap foi suficiente para representar o terreno com precisão.

Padrões de escoamento mostraram que, próximo da superfície do vale, o escoamento é aproximadamente perpendicular às direções de vento predominantes na área. A direção do vento foi a variável menos sensível ao DTM e resolução. Para ventos de sudoeste, o refinamento da malha levou a uma diminuição na velocidade horizontal e aumento na energia cinética turbulenta. O impacto do DTM foi maior para resoluções mais elevadas. Em locais afetados pela complexidade do escoamento no vale (Torre 25 e 29), a resposta aos refinamentos de malha para diferentes DTM foi diferente, divergindo com o SRTM e estabilizando com o HRMap. Para ventos de nordeste, a Torre 37 mostrou diferenças de 2 $m\ s^{-1}$ na velocidade horizontal e 0.5 $m^2\ s^{-2}$ na energia cinética turbulenta ao usar o HRMap em vez do SRTM.

Acknowledgements

I am deeply grateful to Prof. José Laginha Palma for his supervision, guidance and all shared knowledge. His suggestions were crucial to the elaboration of this work.

I would like to thank Vítor Gomes for all the patience and constant advice, whose input was very important to steer this work in the right direction. I would also like to acknowledge Prof. Alexandre Lopes for his valuable comments on this thesis and helping me overcome many challenges.

Finally I would like to thank my family for their unmeasurable support and Rita for her continuous encouragement. This accomplishment would not have been possible without them.

Contents

List of Figures

List of Tables

Nomenclature

Greek symbols

ϵ	Dissipation rate of turbulent kinetic energy	$\mathrm{m}^2\ \mathrm{s}^{-3}$
ρ	Fluid density	$kg\ m^{-3}$
τ_{ij}	Reynolds stress	Pa
θ	Potential temperature	$^\circ C$
k	Turbulent kinetic energy	$\mathrm{m}^2\ \mathrm{s}^{-2}$

Roman symbols

d	Displacement height	m
k	von Karmán constant	
LAD	Leaf area density	$\mathrm{m}^2\ \mathrm{m}^{-3}$
LAI	Leaf area index	
n_i	Number of nodes in the i direction	
n_j	Number of nodes in the j direction	
n_k	Number of nodes in the k direction	
P	Pressure	Pa
P_0	Reference pressure	Pa
T	Temperature	$^\circ C$
t_{CPU}	Duration of simulation run	h
u	Wind velocity	$\mathrm{m\ s}^{-1}$
u_*	Friction velocity	$\mathrm{m\ s}^{-1}$
x	Local coordinate	m
y	Local coordinate	m
z	Height above ground level	m

z_0	Roughness length	m
AOI	Area of Interest	
CLC	Corine Land Cover	
DTM	Digital Terrain Model	
HRMap	High Resolution Map	
RMSE	Root mean square error	
SRTM	Shuttle Radar Topography Mission	

Chapter 1

Introduction

The utilization of computational tools for wind resource assessment is an industry standard. However, the wind energy industry still shows considerable differences between predicted and measured energy production values and operating conditions. Although linear CFD models are the most commonly utilized tool for the assessment - since computational effort is lower when compared with non-linear models - there are many limitations to their use, such as the inability to predict flow separation and thus having great difficulties when dealing with complex terrain (Palma et al., 2008). A more complete computational model can describe features that linear models cannot take into account as it assumes many simplifications to the flow equations. The decreasing number of ideal sites to install wind farms has caused the pursuit of terrains of increasing topographic complexity and the possibility of installation of wind turbines near or within forested terrains (da Costa et al., 2006), which imply the use of tools that can fully describe the flow in those locations.

The New European Wind Atlas (NEWA) project aims to develop a high-value data bank from a series of wind measurement campaigns. It also aims to develop methodologies and improve advanced models for wind farm development and wind turbine design (determining the wind conditions with a very low uncertainty) and atmospheric flow experiments in various kinds of complex terrain to validate the models (Mann et al., 2017). One valuable contribution to the project is the double hill experiment at Perdigão. This experiment had the main goal of studying how an upstream hill with flow separation affects the mean wind speed and turbulence at a down-stream hill, and how and if the presence of a wind turbine on the upstream hill will affect the flow separation behind the hill. Field experiments are very important for resource assessment but also to validate and improve flow modelling and numerical techniques (Vasiljević et al., 2017). The complexity of the flow over a double ridge still lacks some numerical validation and the Perdigão campaign results allow a more precise comparison between simulations and the real flow over the double ridge. This flow modelling depends on the terrain description, thus a thorough analysis should be performed to the variety of available map sources for elevation and surface cover to achieve an accurate representation of the terrain, given the large impact it has on the numerical results.

1.1 Atmospheric flows

The study of atmospheric flows adds a great contribute to many areas of atmospheric sciences such as meteorology (that includes the atmosphere's chemistry, physics and dynamics with a focus on weather forecasting) and climatology, and is a very relevant research area to the wind industry for wind resource assessment and wind turbine siting.

1.1.1 Atmospheric boundary layer

The atmospheric boundary layer (Figure 1.1) is the layer of the atmosphere that is closest to the Earth's surface, up to a few kilometers above ground, transporting atmospheric properties both horizontally and vertically (Kaimal and Finnigan, 1994). Its depth is variable in space and time, and the main parameters that influence its structure are surface friction, evaporation, heat transfer, pollutant emission and terrain orography (Stull, 1988).

The surface layer, approximately 10% of the boundary layer's height, is the relevant region to portray in this document and is characterized by a turbulent exchange of heat, mass and momentum due to the surface friction. Turbulence is associated with a time scale from less than one second to several days and a spatial scale from some millimetres to several kilometres, affecting all atmospheric processes. In this region of the atmosphere, wind speed and direction varies strongly with height due to surface friction and temperature gradient, unlike the geostrophic winds that are dominant above the boundary layer, also called free atmosphere, where flow is mostly influenced by the Earth's rotation, but also by thermal effects.

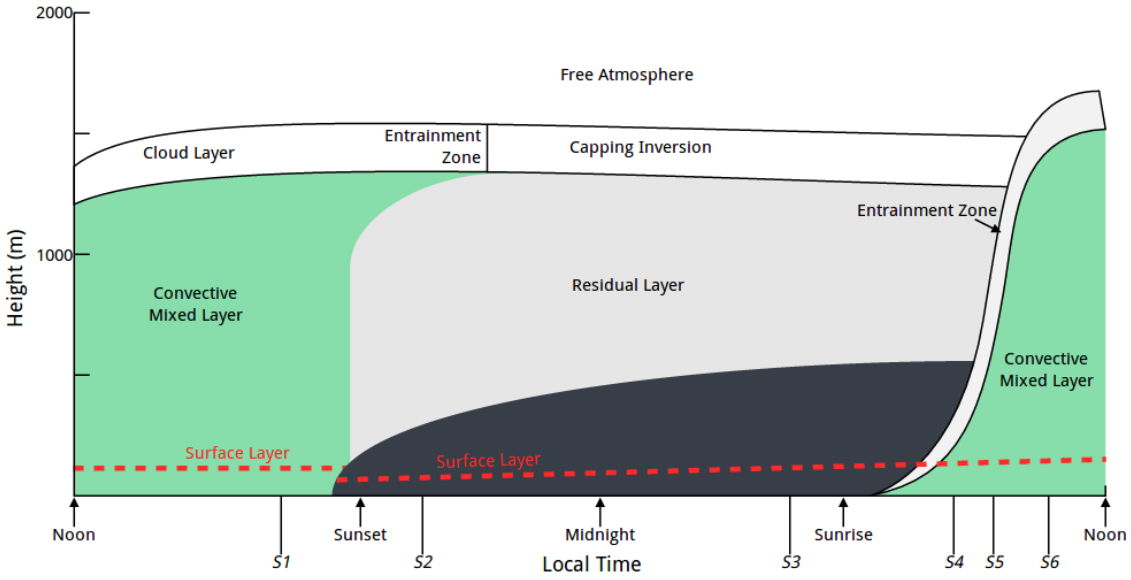

Figure 1.1: Different regions of the atmospheric boundary layer.

Thermal stratification exists in the atmosphere as the Earth's surface temperature

differs from the air above (heated and cooled via radiation) and thus heat transfer mechanisms make the atmosphere deviate from its adiabatic state. The atmosphere's stratification stability can be assessed by evaluating the potential temperature in equation 1.1 (Oke, 1987) and its rate of change:

- $\frac{\partial\theta}{\partial z} < 0$, unstably stratified atmosphere, when the potential temperature decreases with height, potentiating vertical convective movements;
- $\frac{\partial\theta}{\partial z} = 0$, neutrally stratified atmosphere, when the potential temperature is vertically uniform;
- $\frac{\partial\theta}{\partial z} > 0$, stably stratified atmosphere, when the potential temperature increases with height, weakening vertical convective movements.

$$\theta = T\left(\frac{P_0}{P}\right)^{\frac{R}{c_p}} \tag{1.1}$$

The boundary layer is not static in time, changing dramatically during the course of each day, as observed in Figure 1.1. The daily evolution of the atmospheric boundary layer is characterized by the mixed layer, the residual layer and the stable boundary layer. As the sun rises, absorption of solar radiation and subsequently emission by the Earth's surface are responsible of air heating and the turbulence motion becomes driven by convection, causing the growth of the mixed layer, reaching its maximum in the late afternoon. As the sun sets, the solar heating of the surface and the convection and associated turbulent eddies cease, named the nocturnal stable layer. The middle portion of the nocturnal atmospheric boundary layer, called the residual layer, is characterized by weak sporadic turbulence and above it is the capping inversion, that separates boundary layer air from the free atmosphere.

1.1.2 Velocity profile and roughness parameters

The wind velocity (u) profile inside the boundary layer for neutrally stable atmosphere can be represented by the Prandtl's logarithmic law (1.2):

$$\frac{u(z)}{u^*} = \frac{1}{k} ln\left(\frac{z}{z_0}\right) \tag{1.2}$$

where z is the height above ground and z_0 is the surface roughness length (the height above ground where in the mean the wind speed is zero), and u^* and k are the friction velocity and the von Karmán constant.

Higher surface roughness length values lead to higher surface friction causing a momentum sink. To compensate for the displacement of the momentum sink from the surface, the displacement height d is introduced to match observed wind profiles at relatively small distances above a layer of vegetation (Shaw and Pereira, 1982) that deviate from the logarithmic wind profile. Variables z_0 and d are the main parameters

for roughness description and are highly dependent on the vegetation height, its density and structure, and are determined by wind profile fitting to experimental data or numerical models. The modified wind velocity profile is the following:

$$\frac{u(z)}{u^*} = \frac{1}{k} ln \left(\frac{z-d}{z_0} \right) \tag{1.3}$$

Surface roughness characterization is agilized by attributing characteristic z_0 values to different landscape classifications. Many roughness classifications exist and one of the most common is the proposed by Wieringa (1992), a revised classification of the Davenport roughness scale as can be consulted in Table A.1.

1.1.3 Flow over complex topography

Topography and surface cover have a great impact on the flow. This notion of complex terrain is usually associated with areas with mountains (high elevation differences and slopes) or forests (dense and tall vegetation) (Bingöl, 2010).

The flow over complex terrain is usually associated to flow separation (Figure 1.2), high shear factors and turbulence levels. In a simplified hill topography the flow accelerates to the top where it reaches maximum velocity and, for steep hills, can separate yielding a highly turbulent wake region downstream. Real examples of complex topography are generally composed by sequences of mountains, valleys and other geological formations that induce a highly non-linear behaviour to the flow.

The changes in surface elevation can alter the pressure field of the hill region, which affect the local flow field (Kaimal and Finnigan, 1994). The main areas of importance for consideration are hill shape, length scale, and the turbulent effects caused by the topography changes. Depending on the atmospheric conditions, internal gravity waves can also play an important role when stably stratified flow is forced over an obstacle.

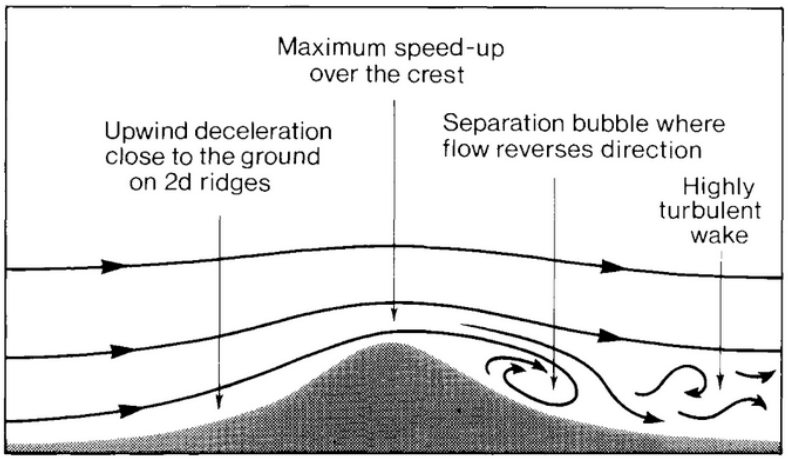

Figure 1.2: Flow over a 2D isolated hill. (Kaimal and Finnigan, 1994)

Extensive studies have been done for different types of topography. Some examples are the reference sites of the Askervein experiment in Scotland (Taylor and Teunissen, 1987; Castro et al., 2003; Silva Lopes et al., 2007) for the study of boundary-layer

flow over low hills, and the Bolund field campaign in Denmark (Bechmann et al., 2009; Diebold et al., 2013) that includes steep slopes and cliffs and aims to increase the understanding of boundary layer flow in complex terrain.

1.2 Perdigão site and campaign overview

Serra do Perdigão is located in Vila Velha de Ródão, district of Castelo Branco, in the centre of Portugal. The site can be generally described as two parallel ridges (Figure 1.3) with Southeast-Northwest orientation, distanced around 1.5 km from each other, that measure about 4 km lengthwise and are 500 m high at their summit (above valley floor). The mentioned area is characterized by having some orographic complexity with forested hilly terrain, with a mixture of farming areas and patches of eucalyptus, being surrounded by the Ocreza river just north of the double ridge and the Tejo river on the south.

Figure 1.3: 3D representation of Serra do Perdigão (View from Google Maps).

The wind rose (Figure 1.4) represents the processed wind speed and direction data from the entire Perdigão campaign in a reference meteorological station located in the south ridge (Tower 37, coordinates in Table 3.3).

The ridges are approximately perpendicular to the two predominant wind directions on that region (SW and NE), assuring a largely two-dimensional flow. The site has the characteristic of having a single wind turbine (Enercon 2 MW; 82 m diameter) on the southern ridge, which leaves the possibility of studying with more depth the wake and double hill interactions, plus power output dependence on the atmospheric conditions.

The Perdigão campaign, set to collect reference data at an unprecedented spatial resolution, has the ultimate goal of replacing the data from the study of the flow over a

single isolated hill in Scotland (Askervein experiment), that has been used for 3 decades to develop and evaluate flow modelling.

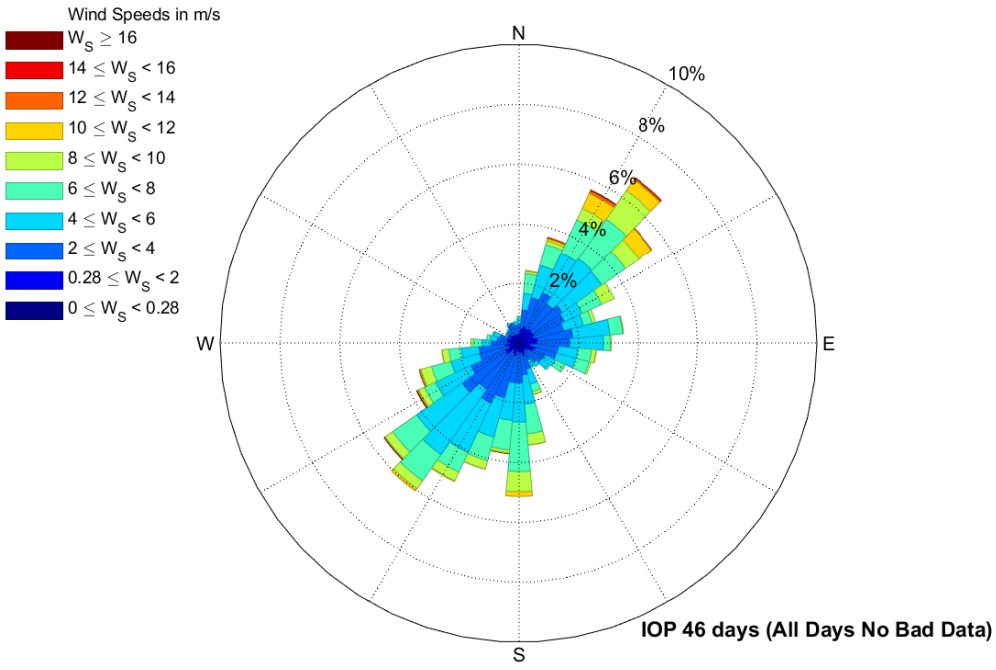

Figure 1.4: Wind regime in Serra do Perdigão. (Vilaça, 2018)

1.2.1 Terrain database

LiDAR (Light Detection and Ranging) technology consists of an active remote sensing technique for the acquisition of high density and accurate data of various parameters, such as wind speed, temperature or elevation. For the latter, pulses of light travel to the ground. When the pulse of light bounces off its target and returns to the sensor, it records the time difference between the emission and the reflection and calculates the variable distances between the sensor and the various surfaces present on the ground (Bachman, 1979). LiDAR delivers a massive point cloud filled of varying elevation values, but height can come from the top of buildings, tree canopy, powerlines and other features, so there is a need for a careful post-processing.

In the preparation of the *Perdigão-2015 field campaign*, a helicopter-based laser mapping mission in 2015 using LiDAR technology and ortophotos enabled the most accurate and detailed description of the field site, including orography, canopy and other surface characterization variables. The area of interest (20 km^2) was scanned with a density of about 45 points per square meter. Orthophotos with a resolution of 5 and 20 cm of the same area were acquired along with the derived point cloud (Vasiljević et al., 2017).

1.2.2 Flow database

Different platforms and databases are currently in use to hold different types of information on the Perdigão campaign: reports, operation plans, weather briefings, instrumentation status, logbooks and product links.

One of the main platforms is WindsP, a Web application that supports the activities of the preparation and execution of the experiments included in NEWA Joint Programme, in particular the Double hill experiment at Perdigão. WindsP supports the work of Experiment managers and participant institutions alongside the experiment's phases, from design and preparation to execution and dissemination of the results. The objective of this Web application is to provide a tool for design and management of the field campaign and archive all the relevant information, such as personnel, instrumentation location, reports and results. Other currently available platforms are NCAR/EOL or Rodeo DTU.

The campaign united a large number of universities and institutions worldwide, and was 46 days long. The setup includes more than 50 masts with instrumentation to measure wind speed, direction, temperature, humidity and other factors, both along and perpendicular to the ridges. Short term campaigns using meteorological balloons were also performed.

1.3 Terrain and land cover model

1.3.1 Digital elevation models (DEM)

A Digital Terrain Model (DTM) or Digital Elevation Model (DEM) is a digital representation of the Earth's surface topography, i.e., terrain elevation at regularly spaced horizontal intervals. The terrain description and ultimately the flow modelling depend on quality of the digital terrain model. The accuracy of a DTM depends on the techniques employed (and the associated sampling density and data collection method) and its post-processing (such as the utilized grid resolution and interpolation algorithms).

There are many ways to obtain a digital terrain model. Most often this data is obtained using remote sensing equipment, by satellite interferometry (such as *SRTM - Shuttle Radar Topography Mission* (Farr et al., 2007) - or *ASTER - Advanced Spaceborne Thermal Emission and Reflection Radiometer* (Yamaguchi et al., 1998) - which are available for free (GisGeography DEM) or photogrammetry (a 3-dimensional coordinate measuring technique that uses photographs as the fundamental medium for measurement).

SRTM has the widest cover and most widespread application and the main objective was to study the Earth's topography by producing digital elevation models of the planet surface with a high resolution (Farr et al., 2007). This mission used technology based on SAR (Synthetic Aperture Radar) and interferometry techniques (Rodriguez and Martin, 1992) mounted on an orbiting space shuttle. The first version of the results was published in 2003 with a 1 arc-second (1″) horizontal resolution (around 30 m at the Equator) for the United States region, and 3 arc-second (3″) for the remaining of the Earth's surface covered by the mission (around 90 m horizontal resolution). In 2014

there was a new version published with 1″ horizontal resolution on most of the planet's surface, as seen in Figure 1.5, corresponding to about 23.75 m resolution at Perdigão's latitude. The first version mentioned above (v2.1 3″, 2003) will be called SRTM 90 m and the second one (V3.0 1″, 2014) will be called SRTM 30 m in the present document. The estimated errors of the SRTM data are summarized in Table 1.1.

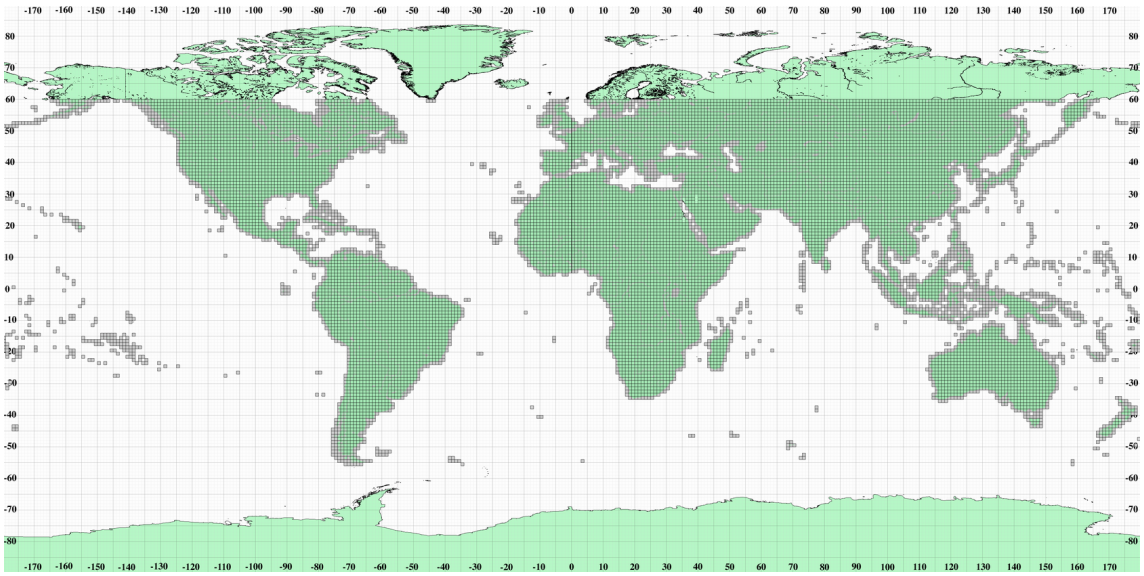

Figure 1.5: Surface of the Earth covered by the SRTM.

	Africa	Australia	Eurasia	N. America	S. America
Absolute geolocation	11.9	7.2	8.8	12.6	9.0
Absolute height	5.6	6.0	6.2	9.0	6.2
Relative height	9.8	4.7	8.7	7.0	5.5
Long-wavelength height	3.1	6.0	2.6	4.0	4.9

Table 1.1: SRTM DEM estimated errors (in meters).

1.3.2 Surface cover

The surface cover is also an important part of the terrain modelling and it is composed by roughness, forests and buildings that affect surface friction. In lower layers of the atmosphere the flow is highly influenced by the friction against the Earth's surface. However, at high above ground levels that influence becomes negligible. Roughness can be characterized by the roughness length z_0 (section 1.1.2) for low vegetation or via canopy model for forests.

This information can be found on Digital Surface Models (DSM, which measure the height values of the first surface on the ground including terrain features, buildings, vegetation, power lines, etc.) such as the one produced by the 2015 airborne survey in Perdigão, allowing the analysis of the site vegetation height and density, along with other features. Geo-referenced data of land cover is another source of information on

terrain surface cover and is becoming increasingly available for locations around the globe, with more detail and accuracy. Some free global land cover / land use data sets can be consulted in GisGeography Land Cover.

Although the LiDAR scanning previously mentioned already contains information about the roughness, another source for the surface cover model was the CORINE Land Cover (CLC) (Bossard et al., 2000) data. CLC is a geographic land cover data source for most of Europe's surface and was elaborated based on the visual interpretation of satellite images. The first version dates of 1990 and updates have been produced in 2000, 2006 and 2012, consisting of an inventory of land cover/land use in 44 classes. The CLC nomenclature is hierarchical, including five major groups: artificial surfaces, agricultural areas, forests and semi-natural areas, wetlands and water bodies, as represented in Table A.2. This version has a minimum mapping unit of 25 ha and a geometric accuracy of under 100 m. The map was obtained by extracting the desired region from the source and has the disadvantage of having a descriptive nature, needing a conversion from the CLC land use classes to numerical data (roughness length), with different conversion tables available.

1.4 Influence of terrain description on numerical modelling

It is very important to quantify the errors associated with changes in digital terrain models and spatial resolution, and the impact they have on the computational terrain representation and flow field numerical results.

Some work has been done in quantifying the impact of using different DTMs and resolution on terrain attributes, such as elevation, slope, plan and profile curvature, topographic wetness index, but few have focused on the impact of those attributes on the numerical flow results, such as wind speed, direction and turbulent kinetic energy.

Mahalingam and Olsen (2016) indicates that DEMs are often obtained and resampled without considering the influence of its source and data collection method and concludes that finer meshes do not necessarily mean higher accuracy in prediction (with examples for landslide mapping where terrain slope has a great influence) with the DEM source being an important consideration with significant influence on the accuracy of a landslide susceptibility analysis.

DeWitt et al. (2015) compares several DEMs (USGS, SRTM, a statewide photogrammetric DEM and ASTER) to a high-accuracy LiDAR DEM to quantitatively and qualitatively assess their differences in rugged topography through elevation, basic descriptive statistics and histograms. Root mean square error values found ranged from 3 (using photogrammetric DEM) to circa 15 (using SRTM) or 17 m (using ASTER). Al Harbi (2009) evaluates the reliability of DEMs generated from InSAR (ERS-1/2) and ASTER data over a sparsely vegetated drainage system. Based on the representation of terrain characteristics against a number of check points collected using GPS data, it finds that InSAR and ASTER reach root mean square errors above 6 and 13 m, respectively.

Deng et al. (2007) indicates that the mesh resolution can change not only terrain attributes in specific points but also the topographic meaning of attributes at each point,

and that spatially aggregated statistical analysis (averaged across the study area) can not capture DEM resolution impact on terrain attributes with accuracy and that spatially explicit approaches need to be used. It concludes that variation of terrain attributes were consistent with resolution change and that the response patterns were dependent on the landform classes of the area.

Florinsky and Kuryakova (2000) develops an experimental three-step statistical method to determine an adequate resolution in DEM to represent topographic variables and landscape properties at a micro-scale (exemplified by soil moisture) by performing a set of correlation analysis between resolutions.

Lange et al. (2017) studies the influence of topography and terrain description on the flow field by comparing a round and a sharp edge of a cliff in a wind tunnel showing that the flow with the sharp edge gives an annual energy production of a wind turbine near the escarpment that is 20% to 51% of the round-edge case. Numerical modelling with different spatial resolutions for the same case (Diebold et al., 2013) shows that change in resolution (1 m to 2 m) can result in doubling the mean-wind error between simulated and measured results. Lange et al. (2017) concludes that ”even if accurate terrain descriptions are available, it is unclear whether any numerical model can predict the observed flow measured in the terrain”.

1.5 Computational modelling of atmospheric flows

The many different processes that occur in the atmosphere and its evolution are governed by a set of second order non-linear differential equations that describe the fluid dynamics, commonly known as the Navier-Stokes (NS) equations. Different approaches and mathematical models have been developed for an approximate solution of those equations.

1.5.1 CFD

Computational fluid dynamics (CFD) is a branch of fluid mechanics that makes use of different numerical methods, mathematical models and software tools (solvers, pre and post-processing utilities) in order to analyze and solve problems involving fluid flows that are governed by the NS equations. CFD allows an insight into flow patterns that are difficult, expensive or impossible to obtain using experimental techniques or analytic solutions and is now a part of the standard engineering design environment of many industries, being normally more cost-effective than physical testing.

Software like WAsP (Mortensen et al., 1993), the industry standard for wind resource assessment and siting of wind turbines, rely on the linearized form of the NS equations. However, different studies concluded that the use of linear, simple, mathematical models of fluid flow equations is questionable, specially when describing flow motion in complex terrain, because of its inability to predict flow separation (Palma et al., 2008).

CFD codes based on the solution of non-linearized NS equations allow the simulation of turbulent atmospheric boundary layer flows over complex terrain without some

of the limitations of linear models such as its inability to predict flow separation and any non-linear phenomena. The disadvantages of such codes are the intensive computer resources and time needed.

1.5.2 Discretization

The discretization is the process of substituting the continuous domain by a discrete one using a mesh where each flow variable is defined only at each mesh point and the transformation of the partial differential equations that govern the fluid flow into a set of algebraic equations that contain the variables that are of unknown value at each node. The values at other locations are determined by interpolating the values at the mesh points. There are many methods to the discretization process such as the finite-difference method or the finite-volume method, with focus on the last one for this document. The finite-volume method divides the domain into a number of control volumes (CV) where the variable of interest is located at the centroid of the CV, applying the integral form of the governing equations to each one and describing the variation of quantities between cell centroids by different interpolation techniques. The solution satisfies the conservation of quantities such as mass, momentum, energy, and species for each CV and in their sum, for the entire computational domain.

1.5.3 Solving N-S equations

Different methods to computationally solve turbulent flows are RaNS (Reynolds averaged Navier-Stokes), LES (Large eddy simulations) and DNS (Direct numerical simulation), ordered by increasing need of computational effort. RaNS deals with time-averaged equations of motion for fluid flow, and is part of the approach used in the remaining document. With LES, large eddies are solved directly while small eddies are modelled using a sub-grid scale model. DNS resolves all turbulent phenomena at every length and time scales by numerical solving the continuity and momentum equation.

Turbulence can be seen as the overlap of a mean flow with a rapidly fluctuating flow with a mean value of zero, which is called a Reynolds decomposition. By inserting this approach in the continuity and momentum equation, one can obtain the RaNS equation, which leads to the appearance of a new term, named as the Reynolds stress $\tau_{ij} = -\rho\overline{u_j' u_i'}$. The number of unknowns is larger than the number of equations (ten opposed to four) and thus a turbulence model has to be introduced to achieve closure, such as one-equation, two-equation or Reynolds stress models.

1.6 Objectives

The main purpose of the present work is to elaborate on the computational flow model of Perdigão and its spacial requirements. It also aims to evaluate different digital terrain models available and its comparison to conclude on the best topographic representation of the site by different parameters, such as elevation and slope. A numerical mesh analysis and a parametric study of the boundary positions has the goal of observing

the impact on wind speed, direction and turbulent kinetic energy provided by different simulation results.

The addition of complexity to the terrain and atmospheric flow modelling by representing the surface cover (via increased roughness or explicit canopy model) also required an evaluation of different information sources and aims to determine the level of detail and the surface cover parameters that best describe the terrain, and its influence on the numerical results.

Ultimately, it is also an objective to compare some experimental data from the Perdigão campaign with the simulation results for both predominant wind directions on the region.

1.7 Outline of the thesis

This document is organized into 5 chapters. Chapter 1, the introduction, lists the main objectives, and briefly reviews the most relevant topics. The mathematical model and numerical techniques are the subject of Chapter 2. The results are organized in two different chapters (3 and 4).

The terrain model in chapter 3, showing the main differences between the different digital terrain models considered and the influence of the numerical mesh in its description. Land cover information sources are also described in order to produce a roughness map to use on further simulations.

Results on the flow modelling are in Chapter 4, such as the simulation results in terms of profiles and contours that describe the flow, comparing digital terrain model and land cover sources and the impact it has on physical variables. A brief description on relevant results specifically for the wind turbine location are also presented.

Chapter 5 summarizes the main conclusions along with suggestions for future work.

Chapter 2

Mathematical model and numerical techniques

The present chapter describes the mathematical model used in the present work for fluid flow modelling and is divided in three sections: a brief description of the software used is made in section 2.1 and the fundamental equations are displayed in section 2.2. Discretization techniques and boundary conditions are exposed in section 2.3.

2.1 Wind flow simulation

The equations and models defined in this chapter pertain to the VENTOS®/2 (Castro, 1997; Castro et al., 2003) software, a computational fluid dynamics computer code used in the course of this work. It is tuned for atmospheric flows over complex terrain, solving RaNS set of equations for a steady turbulent flow, with a terrain-following structured mesh. The software allows the simulation of forested and unforested terrains by explicitly modelling canopy and with the possibility of modelling the presence of operating wind turbines and the associated wake flow.

The transport equations software are discretised with the finite-volume technique, which substitutes the continuous domain by a discrete one and transforms the partial differential equations above into a set of algebraic equations (Patankar, 1980). The set of equations is then solved by the SIMPLE (Semi-Implicit Method for Pressure Linked Equations) algorithm (Patankar and Spalding, 1972).

2.2 Flow and turbulence model equations

The fundamental mathematics governing fluid flow, the Navier-Stokes equations, were solved in their Reynolds averaged form (RaNS). At their core are the equations for conservation of mass (2.1) and momentum (2.2), which in their Cartesian form and in tensor notation are:

$$\frac{\partial \rho \overline{U_i}}{\partial x^i} = 0 \ , \tag{2.1}$$

$$\rho \frac{\partial \overline{U_j U_i}}{\partial x^j} = -\frac{\partial \overline{P}}{\partial x^i} + \frac{\partial}{\partial x^j}\left(\sigma_{ij} + \tau_{ij}\right) + F_i \ , \tag{2.2}$$

where x^i is the i-th Cartesian coordinate, $\overline{U_i}$ is the i-th component of the mean flow velocity field, ρ is the fluid density, $\overline{P}$ is the mean pressure and τ_{ij} and σ_{ij} are the viscous (2.3) and Reynolds (2.4) stress tensors respectively. F_i is the aerodynamic force-per-unit-volume due to the presence of canopy.

$$\tau_{ij} = \mu \left(\frac{\partial \overline{U_i}}{\partial x^j} + \frac{\partial \overline{U_j}}{\partial x^i} \right) \tag{2.3}$$

$$\sigma_{ij} = -\rho \overline{u_i' u_j'} \tag{2.4}$$

Turbulence model

To obtain closure for the RaNS equations and model the Reynolds stresses $\overline{u_i' u_j'}$ the $k-\epsilon$ model is employed. Based on the turbulent viscosity approximation, the Reynolds stresses are modeled (2.5) using the turbulent viscosity scalar (2.6) and two additional transport equations are solved for turbulent kinetic energy k (2.7) and its dissipation rate ϵ (2.8).

$$\sigma_{ij} = -\rho \overline{u_i' u_j'} = -2/3 \rho k \delta_{ij} + \mu_t \left(\frac{\partial \overline{U_i}}{\partial x^j} + \frac{\partial \overline{U_j}}{\partial x^i} \right) \tag{2.5}$$

$$\mu_t = \rho C_\mu \frac{k^2}{\varepsilon} \tag{2.6}$$

$$\rho \frac{\partial \overline{U_j} k}{\partial x^j} = \frac{\partial}{\partial x^j} \left[\left(\mu + \frac{\mu_t}{\sigma_k} \right) \frac{\partial k}{\partial x^j} \right] \mathcal{P}_k - \rho \varepsilon + S_k \tag{2.7}$$

$$\rho \frac{\partial \overline{U_j} \varepsilon}{\partial x^j} = \frac{\partial}{\partial x^j} \left[\left(\mu + \frac{\mu_t}{\sigma_\varepsilon} \right) \frac{\partial}{\partial x^j} \right] + \frac{C_1}{k} \mathcal{P}_k - \frac{C_2 \rho \varepsilon^2}{k} + S_\varepsilon \tag{2.8}$$

The turbulent kinetic energy production term is defined by equation 2.9, and the constants associated to the $k-\varepsilon$ are presented in Table 2.1.

$$\mathcal{P}_k = \sigma_{ij} \frac{\partial U_i}{\partial x^j} \tag{2.9}$$

C_μ	C_1	C_2	σ_k	σ_ϵ
0.033	1.44	1.92	1.00	1.85

Table 2.1: $k-\epsilon$ model constants for atmospheric flows.

Canopy model

Forest canopy produces an aerodynamic drag force that can be explicitly modeled in the momentum (2.2) and turbulence (2.7,2.8) equations. The terms for momentum loss F_i and production/destruction of turbulent quantities S_ϵ and S_k are parametrized by equations (2.10), (2.11) and (2.12):

$$F_i = -\frac{1}{2}\rho\alpha C_D|\overline{U}|\overline{U_i} \tag{2.10}$$

$$S_k = \rho C_z\left(\beta_p|\overline{U}|^3 - \beta_d|\overline{U}|k\right) \tag{2.11}$$

$$S_\epsilon = \rho C_z\left(C_{\varepsilon 4}\beta_p\frac{\varepsilon}{k}|\overline{U}|^3 - C_{\varepsilon 5}\beta_d|\overline{U}|\varepsilon\right) \tag{2.12}$$

The canopy model terms include the local mean velocity module $|\overline{U}|$, the local foliage area per unit volume α and the canopy drag coefficient C_D, with the later two depending on the canopy type. Associated to the terms are also the model constants, presented in Table 2.2.

β_p	β_d	$C_{\epsilon 4}$	$C_{\epsilon 5}$
0.0	4.0	0.0	0.9

Table 2.2: Canopy model constants for the $k-\epsilon$ equation terms.

2.3 Domain discretization

The model topography is obtained from the input topography using bi-linear interpolation techniques. The central part of the domain is resolved with uniform horizontal resolution, expanding towards the domain boundaries (Figure 2.1). The vertical meshing ensures the first CV has the intended height, expanding towards the top boundary similarly to the horizontal mesh (Figure 2.2).

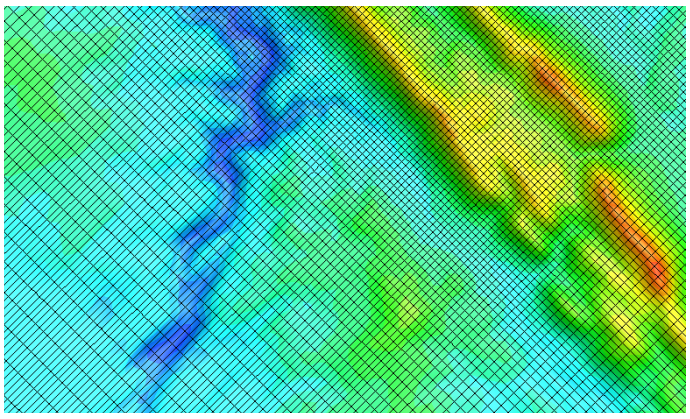

Figure 2.1: Portion of a domain mesh resolved with a constant horizontal resolution, expanding towards domain boundaries.

Both horizontal and vertical mesh expansions are obtained from geometrical expansion, where the ratio between consecutive grid nodes is kept constant, or in other words

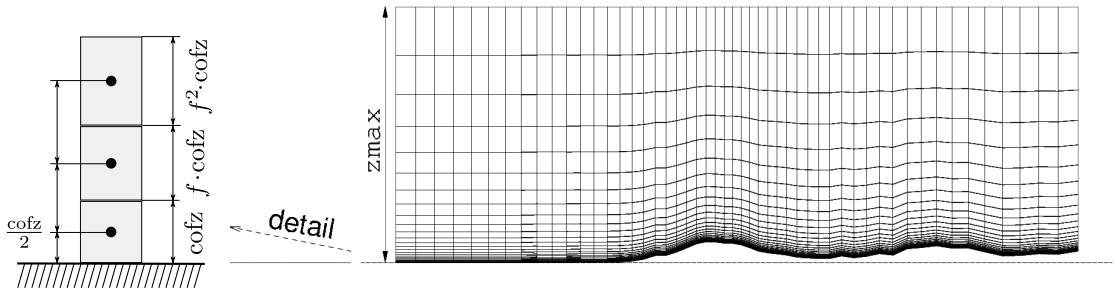

Figure 2.2: Example section of the vertical mesh, expanding from the terrain-following surface towards the top boundary. On the left the near surface vertical mesh dimensions are represented.

the distance between grid nodes increases at a constant rate. To maintain the numerical discretization errors to a minimum this ratio is kept close to 1.

Boundary conditions

The flow model employs static boundary conditions, mimicking a wind-tunnel flow: one inlet and one outlet boundary, with specific conditions for lateral, top and bottom boundaries. The orientation of the domain determines the main flow direction, while the inlet, bottom and top boundary conditions control the inflow of momentum and turbulence quantities. Any set of boundary conditions applied to a CFD simulation must be coherent between them and either be or quickly settle into equilibrium conditions, so as to avoid stream-wise gradients.

At the inlet a log-law profile is set (2.13). To ensure an equilibrium shear stress profile (linearly decreasing with height), the k profile is approximated in that it decreases with the square of height above ground level (a.g.l.), so turbulent quantity inlet profiles are as in equations 2.14 and 2.15.

$$u = \frac{u_*}{\kappa} \ln\left(1 + \frac{z}{z_0}\right) , \tag{2.13}$$

$$k = C_\mu^{-1/2} u_*^2 \left(1 - z/\delta_m\right)^2 , \tag{2.14}$$

$$\varepsilon = \frac{C_\mu^{3/4} k^{3/2}}{\kappa \left(z + z_0\right)} , \tag{2.15}$$

To limit the need for vertical resolution near the ground, a wall function is applied to the bottom boundary condition. It is modelled as a rough surface, with the log-law (1.2) defining the velocity at the node closest to the ground. As part of the wall function, the turbulence model quantities k and ε (plus associated turbulence model terms) are also defined.

At the top of the domain a zero shear stress condition is used. Since the domain height is typically greater than the boundary layer height, the inlet profile's development is caped at the boundary layer's limit, all quantities in equations (2.13) through (2.15)

being constant above that height. At the lateral boundaries a simple symmetry condition is applied to all solved quantities.

Chapter 3

Terrain and land cover model: results and discussion

In this chapter different digital models of terrain and surface of the Perdigão site are analyzed. The terrain height and slope given by different combinations of terrain data sources and meshes are compared with the terrain height and slope measured by the LiDAR.

The chapter is made of two major sections: section 3.1 related with the representation of the terrain and section 3.2 dealing with the terrain cover. The chapter ends (section 3.3) with the main conclusions and the recommendations on which data basis and horizontal resolution are most appropriate in the computational modelling of the flow over Perdigão.

3.1 Digital terrain model comparison

Gomes (2012), in the first computational modelling of Perdigão, used the SRTM 90 m as DEM. New and improved sources have come up since then. The sources considered in this document are the following:

1. Aerial LiDAR scanning, 2015 (section 1.2.1);
2. SRTM v2.1 3″, 2003 (section 1.3.1);
3. SRTM V3.0 1″, 2014;

The aerial LiDAR survey of 2015 scanned Serra do Perdigão (Vasiljević et al., 2017), with a density of *circa* 45 points/m^2, covering an area of 4×5.4 km (Figure 3.1a) encompassing the whole site experiment. The products of this scanning are the terrain orography, vegetation height, leaf area index, roughness length and building height.

3.1.1 Terrain model over an enlarged area

To obtain a regularly spaced and shaped map (10 × 10 km) of the DTM, the area covered by the LiDAR scanning (Figure 3.1a) was complemented by terrain data of Portuguese military topographic survey (10×10 m horizontal resolution) and SRTM 30 m topography data. This final map (Figure 3.1b) will be from this point forward called HRMap (High Resolution Map).

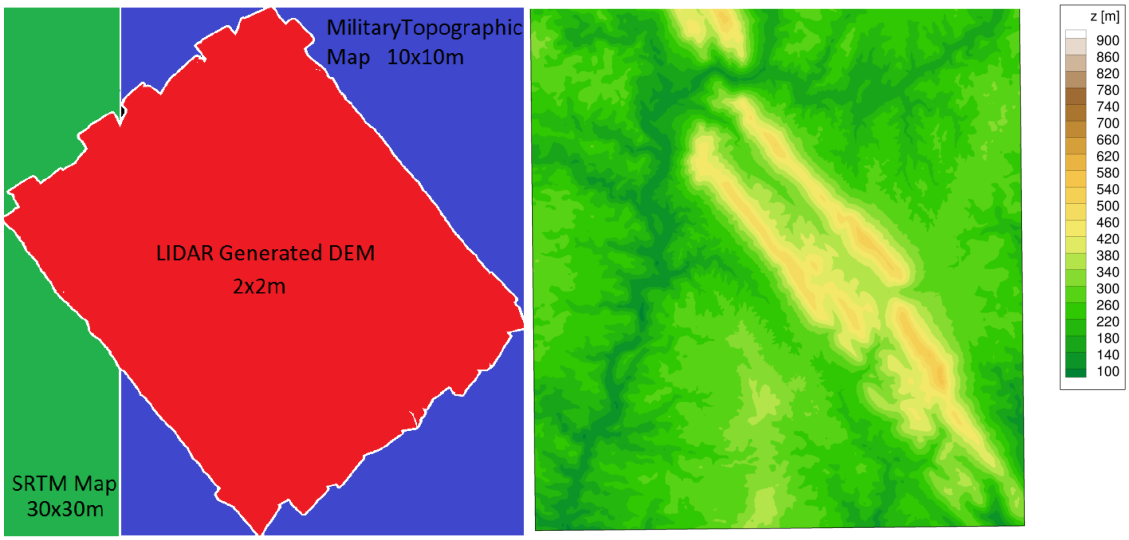

(a) HRMap composition Santos et al. (2017) (b) HRMap

Figure 3.1: Area covered by the high resolution map (HRMap) and its composition.

Because the HRMap was the most accurate representation of the terrain in Perdigão, this map was used throughout the present document to judge the accuracy of alternative terrain data sources, and their impact on the terrain meshes generated for computational modelling of the flow over the Perdigão area.

SRTM 30 m topography data was used as a complement to the HRMap outside its area of coverage, including a maximum area of circa 40×40 km centred around Perdigão. Figure 3.2 shows the superposition of the DEM with the surrounding landscape.

3.1.1.1 SRTM 30 m *versus* LiDAR terrain scanning

The spectral analysis in Figure 3.3 shows the higher resolution achieved by HRMap, by more than an order of magnitude when compared to SRTM30 m. In the overlapping section of the two maps spectra agreement is good, implying equivalent DEM data. The figure also displays two scaling ranges, typical of global topographies (Nikora and Goring, 2004) with exponents equal to -7/4 and -11/3.

The elevation histogram (Figure 3.4) shows this higher resolution of the HRMap has a greater impact on the lower elevation values. As the resolution increases (Table 3.1), the maximum (z_{max}) increases (548, 557 and 563 m) and the minimum (z_{min}) decreases (110, 104 and 85 m), whereas the average (z_{aver}) value (260 m) hardly changes.

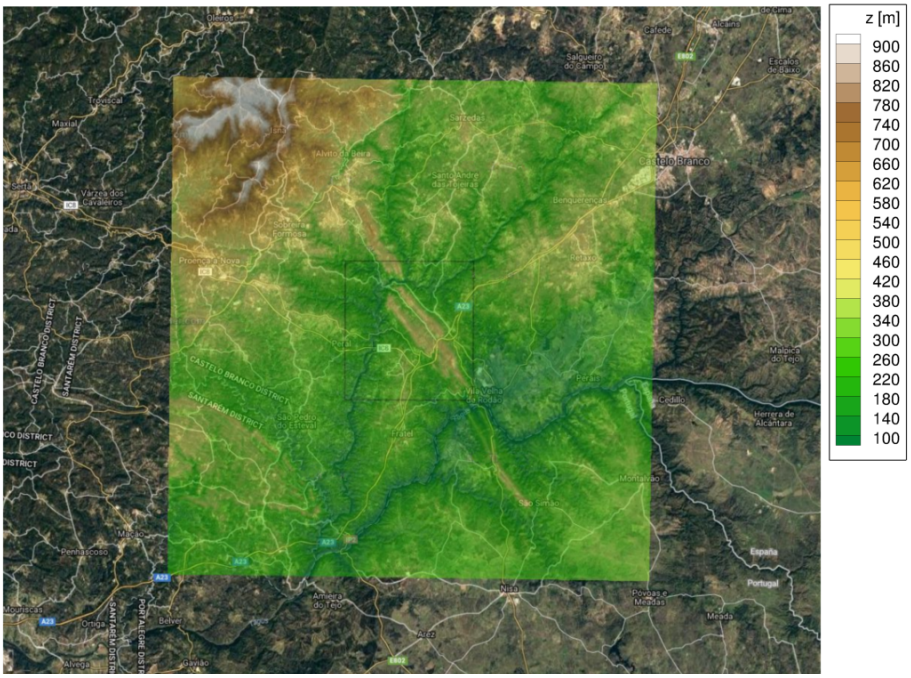

Figure 3.2: Superposition of the SRTM 30 m DEM with the surrounding landscape.

	z_{max}	z_{min}	z_{aver}
SRTM 90m	548.00	110.00	260.80
SRTM 30m	557.00	104.00	260.86
HR Map	562.93	85.24	259.92

Table 3.1: Maximum, minimum and average of DTM elevation values.

Santos et al. (2017) also compares the terrain elevation in both LiDAR and the SRTM 30 m DTM and reported a mean error (LiDAR DTM minus SRTM) of less than 1 m (table 3.2) but with a high standard deviation (circa 5 m), with maximum and minimum equal to 34.546 and -40.177 m and 0.947 correlation between maps. Positive errors tend to be located along the ridges, whereas the northeast side of the northeast ridge seems to be mostly affected by negative errors (Figure 3.5).

Indicator	Value
Mean	-0.792 [m]
Standard deviation	4.667 [m]
Maximum Value	34.564 [m]
Minimum Value	-40.177 [m]
Correlation	0.947

Table 3.2: Elevation error mapping of SRTM 30 m relative to LiDAR DTM.

A topographic survey also took place on site to thoroughly register the elevation data from most of the instrumentation that was installed. When comparing all 17 GPS measured points with the LiDAR DEM, a RMSE of 1.58 m is registered, while the comparison with the SRTM30 for those same points reveals a RMSE of 3.24 m. An extensive

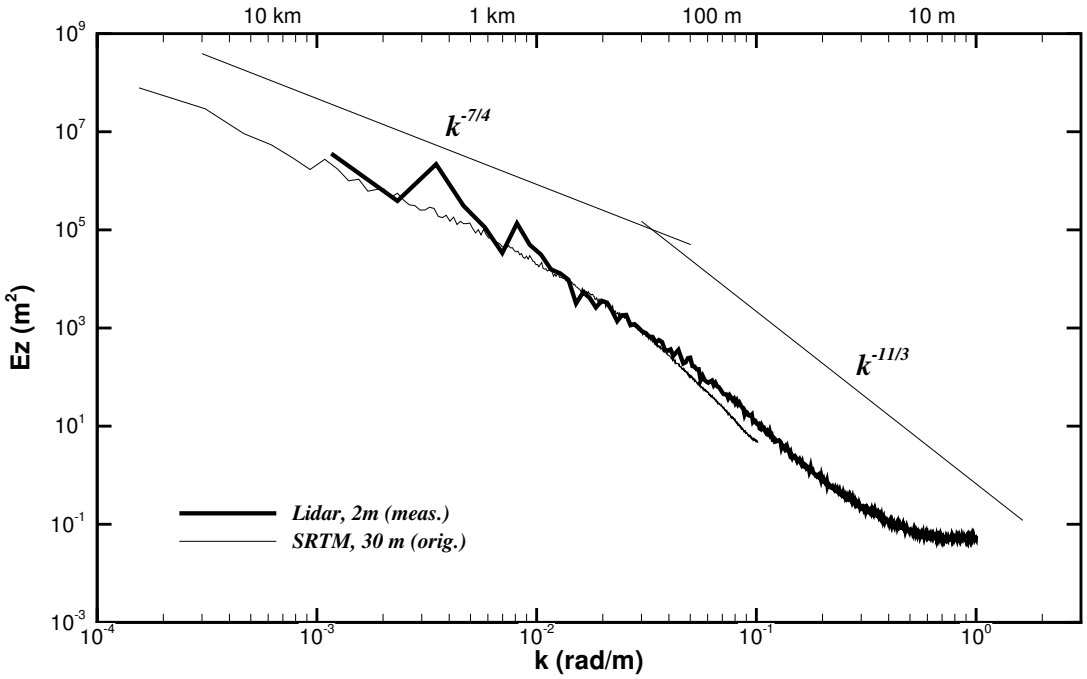

Figure 3.3: Spectra analysis for HRMap (10×10 km) and SRTM30 (40×40 km).

description on that data and the associated error for each of the instruments can be found in B.1.

3.1.2 Area of interest (AOI) and reference locations

To compare the different DTMs and quantify the detail needed an area of interest (AOI) was defined (Figure 3.6). Note that the coordinate system was converted from ETRS89 PT-TM06 (original source) to ED50 UTM29 and will be used throughout the document as Eastings and Northings. Some figures will be displayed in x and y coordinates, a local coordinate system centered in a center point where the domain is rotated in order to x being aligned with the predominant flow direction.

This area, measuring 4×6 km centred near station 131[1] (LiDAR instrument installed at an orange groove), included the double ridge, the valley and the location of most of the instrumentation deployed in Perdigão. Five critical locations (table 3.3) of the Perdigão layout were selected for DTM comparison:

1. Climatological Tower 37/rsw06 (60 m height);
2. Wind turbine;
3. Tower 20/tse04 (100 m height);
4. Tower 25/tse09 (100 m height);

[1]Station number as in Perdigão web site, https://perdigao.fe.up.pt/

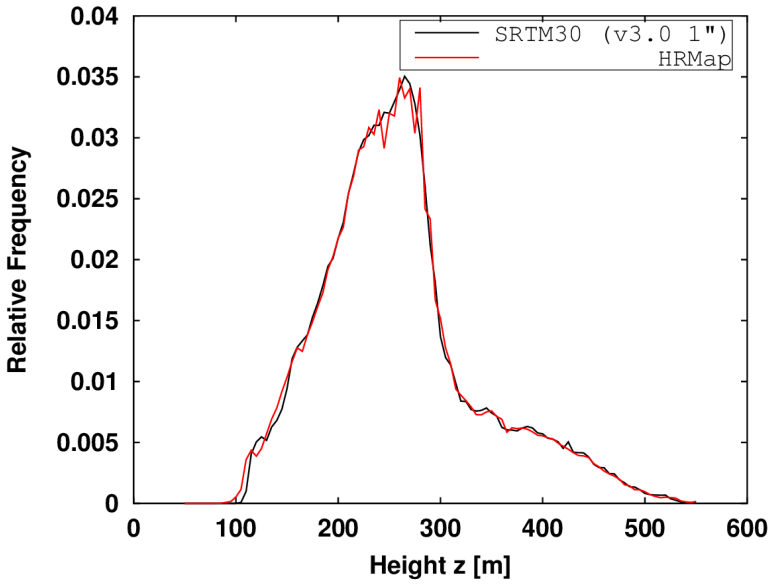

Figure 3.4: DTM frequency histogram of elevation values.

5. Tower 29/tse13 (100 m height).

Location number 1 corresponds to the extensively instrumented climatological tower and provides a clearer view of the whole site; number 2 is the wind turbine location selected for its wind energy relevance, while numbers 3, 4 and 5 are the 100 m meteorological towers comprising a transect crossing the whole site in the dominant flow axis. Numbers 1, 2 and 3 are locations along the SW ridge, whereas 3, 4 and 5 are the reference locations of the terrain profile in Perdigão.

	Tower 20	Tower 25	Tower 29	Tower 37	Wind turbine
Eastings [m]	607818	608571	608948	607507	607702
Northings [m]	4396091	4396684	4396955	4396515	4396262

Table 3.3: Location of the five reference points

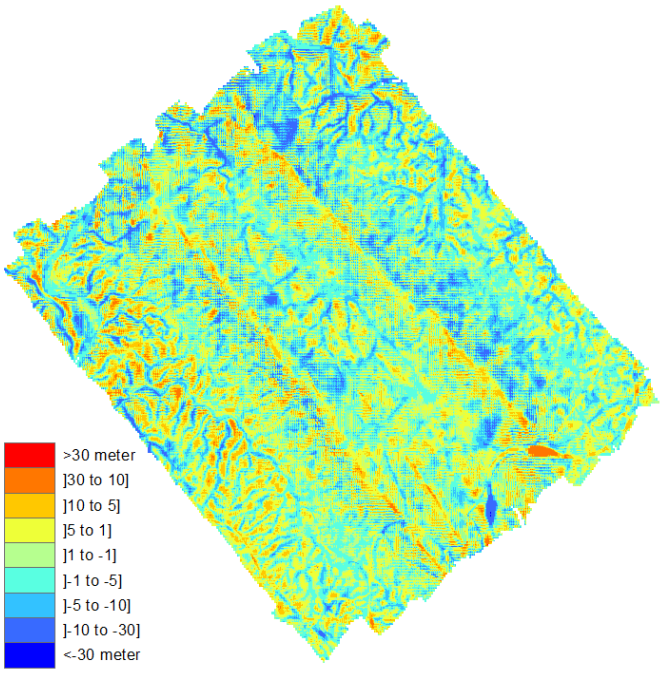

Figure 3.5: Elevation error mapping of SRTM 30 m relative to LiDAR DTM. Santos et al. (2017)

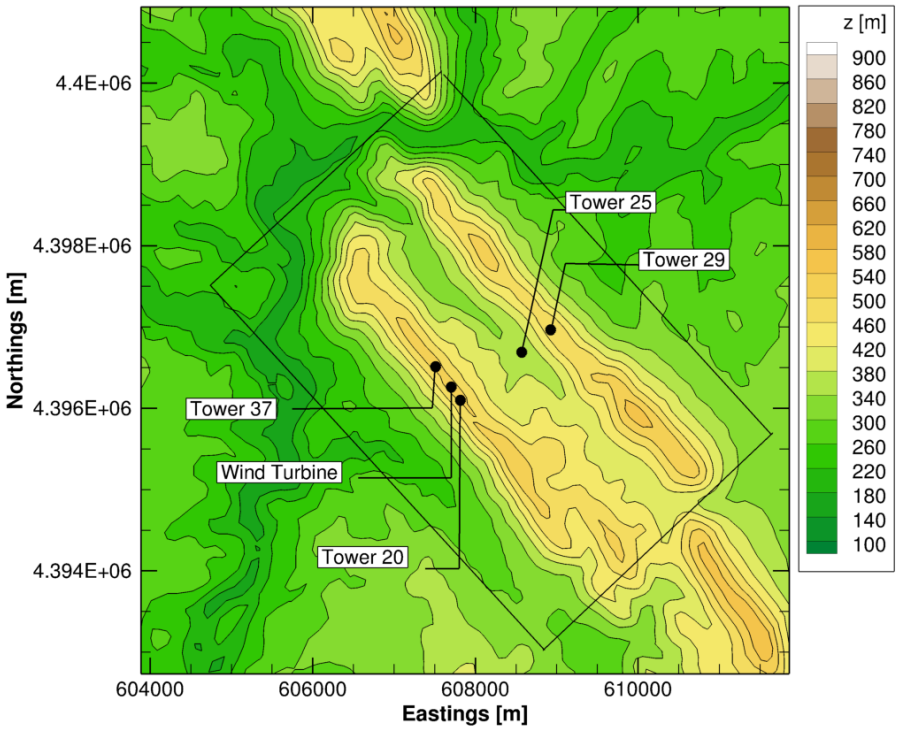

Figure 3.6: Representation of the area of interest (full line rectangle and five critical locations).

3.1.2.1 Computational meshes based on SRTM 30 and LiDAR terrain scanning

When producing the computational meshes, the DTM data is resampled to a larger horizontal resolution. To find the resolution that satisfactorily represents the terrain, based on both the HRMap and SRTM30 data, regularly spaced meshes were generated with 80×80, 40×40, 20×20 and 10×10 m horizontal resolution. Each mesh includes all the points of the coarser ones, meaning they are directly comparable.

A spectral analysis was also performed to the different horizontal resolution meshes of both DTM sources (Figure 3.7). This analysis showed the increase in spectra range, as horizontal resolution increases, and a perfect overlap between meshes with HRMap. Beyond 40×40 m, SRTM30 performs higher order interpolations as it exceed its horizontal resolution, showing greater decay for higher frequencies that linear refinements beyond the source's resolution cannot correct. Only meshes based on the HRMap have the ability to reproduce the high-frequency range ($7 \times 10^{-2}\ rad/m < k < 1\ rad/m$).

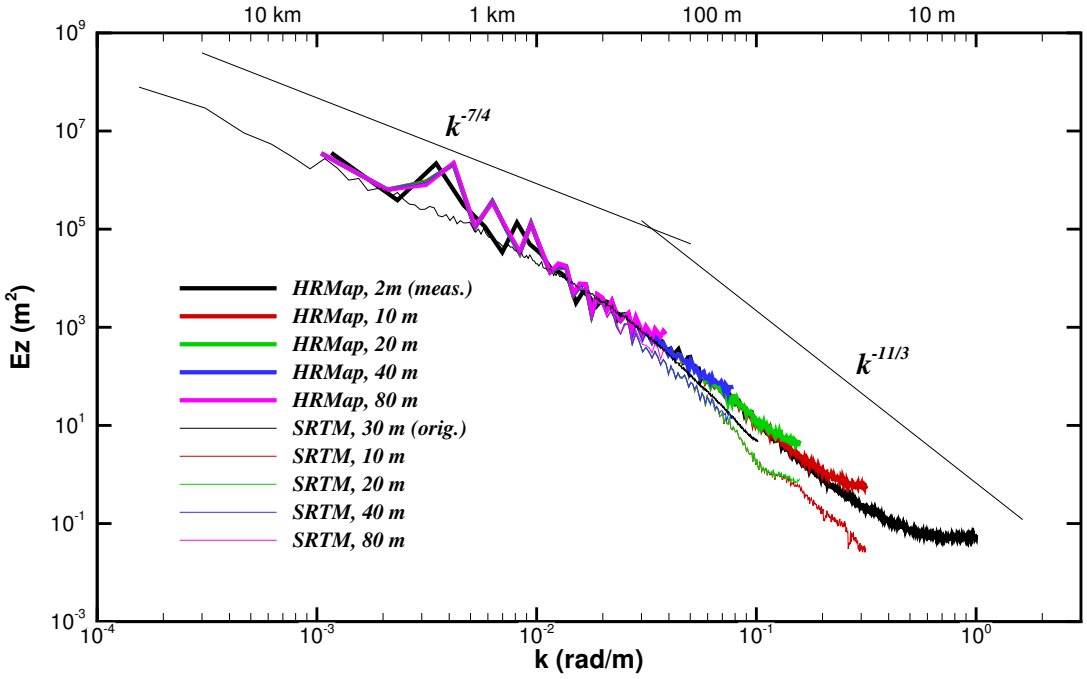

Figure 3.7: Spectra analysis for both DTM sources and with different resolution meshes.

The basic statistics (Table 3.4) show that mesh quality was as good as the terrain data source. SRTM30 is restricted to around 30 m resolution and meshes 20×20 and 10×10, with identical z_{max} and z_{min} (531 and 107 m), are naturally unable to replicate the HRMap measured values, z_{max} and z_{min}.

A 2×2 m horizontal resolution mesh, based on the HRMap was used as reference against which the elevation root-mean square error (RMSE) of any other mesh in the AOI was determined (Figure 3.8a). In the case of the SRTM30, the error tends to a constant value close to the standard deviation as determined by Santos et al. (2017), whereas if based on the HRMap it decreases with the mesh refinement, reaching a value equal to 0.27, for a resolution of 10×10 m. This limitation of the SRTM30 terrain data can also be

	z_{max}		z_{min}		z_{aver}	
	SRTM30	HRMap	SRTM30	HRMap	SRTM30	HRMap
80×80	528.48	537.73	110.53	106.39	309.07	308.07
40×40	530.22	537.73	107.64	105.80	310.26	309.26
20×20	531.13	539.19	107.63	102.83	310.87	309.86
10×10	531.44	540.71	107.33	102.83	311.18	310.17
2×2	-	540.84	-	102.72	-	310.41

Table 3.4: Maximum, minimum and average terrain elevation as a function of mesh resolution for the SRTM 30 m and HRMap.

measured in terms of the difference between maximum and minimum (Figure 3.8b), in which case SRTM30 data has a difference circa 15 m irrespective of mesh resolution. At the highest resolution, it has a 424.11 m difference between the highest and the lowest elevation, whereas the HRMap shows 437.88 m.

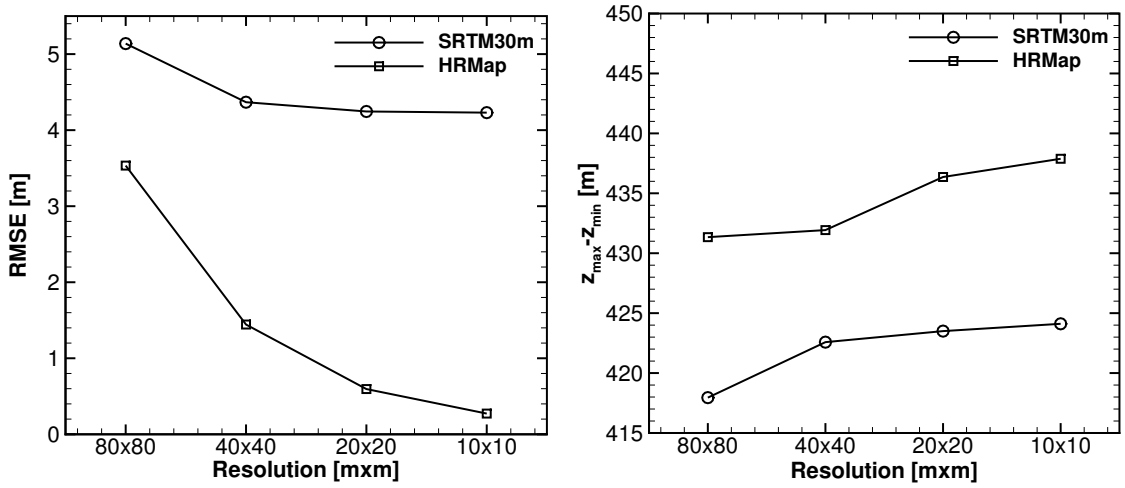

(a) RMSE error

(b) $z_{max} - z_{min}$

Figure 3.8: Impact of mesh resolution on RMSE (a) and the difference between the maximum and minimum terrain elevation (b).

¡ The distribution of error over the AOI is much reduced between the 80 and the 40 m resolution meshes (Figure 3.9). The latter displays a mostly uniform error distribution of around 1 m. If based on the HRMap, the error at the five locations (Figure 3.10b) is less than 1 m for any horizontal resolution finer than 40 m.

That same error was registered at the five reference points mentioned before, using both SRTM30 and HRMap with results plotted in Figure 3.10. When using HRMap, mesh refinement shows visible reduction of error in all 5 points, as when using SRTM30 the error stabilizes or even increases with mesh refinement in some points.

The previously mentioned GPS measurements on site can also detail the elevation error for Tower 20 between the LiDAR source and the topographic survey (table B.1), which reveals a 0.25 m difference in elevation.

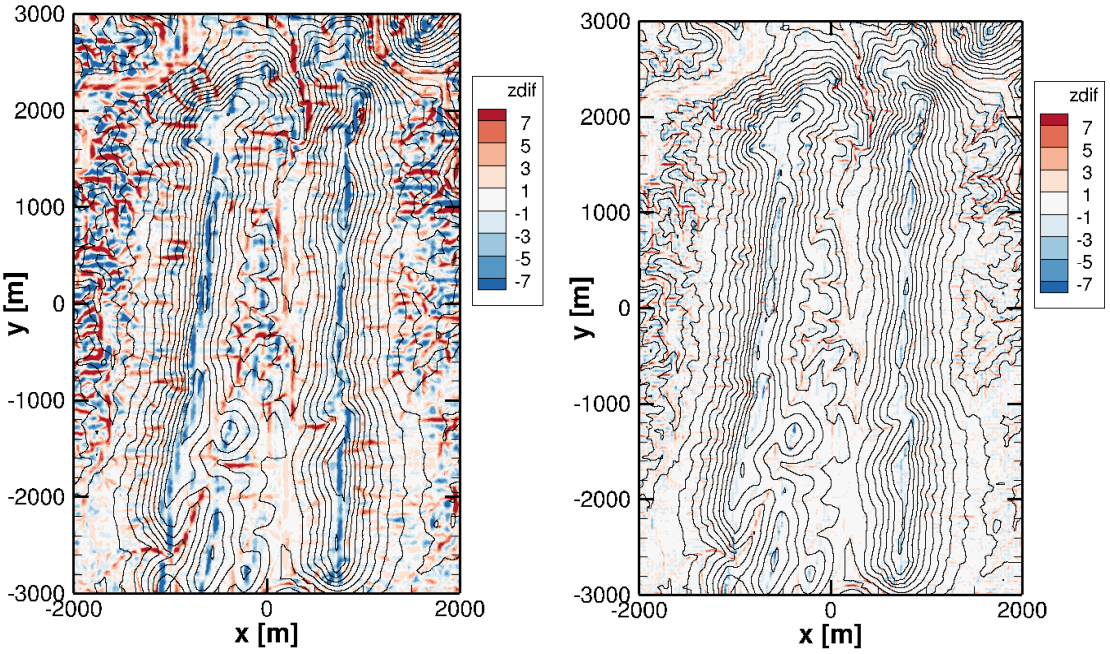

(a) 80×80 m. (b) 40×40 m.

Figure 3.9: Elevation error of resampled meshes mapped over the AOI surface.

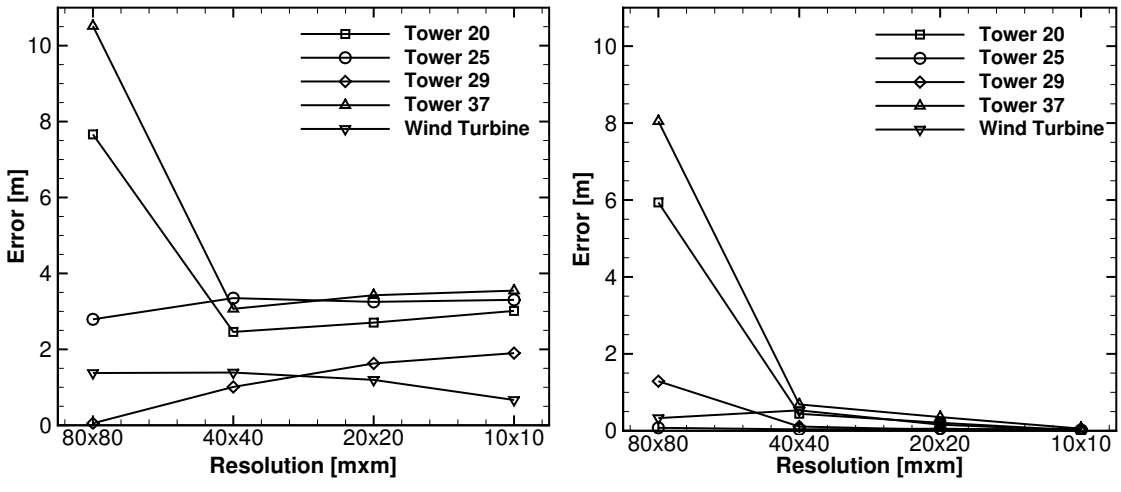

(a) SRTM30m (b) HRMap

Figure 3.10: Elevation error on the 5 key points with different horizontal resolution meshes.

Conclusions on the resolution can be reached:

- SRTM 30 m was not sufficient to accurately represent the terrain.
- SRTM 30 m severely limits accuracy advantages of using higher resolution meshes.
- The HRMap source displays lower elevation errors over all the AOI.
- All remaining studies on the terrain model should be based on the HRMap data.
- Elevation error at the five critical locations, when using the HRMap, can be reduced to less than 1 m at 40×40 m and 0.5 m at 20×20 m horizontal resolution.

3.1.2.2 Terrain slope

Because the terrain slope is also an indicator of the mesh quality, it was calculated along the x and y direction (perpendicular and parallel to the ridges) and shown in Figures 3.11 and 3.12. Since the ridges are mostly two-dimensional, the y direction slope is residual and more focus was given on the x direction.

The maximum slope (x direction) at the AOI (table 3.5) is about 2× higher (140.70% and 195.90%) on a 20 or 10 m mesh resolution compared with the coarsest resolution (78.04%). The minimum slope decreases from -102.83% to -241.59%, between the 80 or 10 m resolutions.

A histogram of the absolute values of the slope in the x direction (Figure 3.14) shows a slight shift to the right when refining the mesh. As the resolution increases the histogram content below 0.2 decreases and is transferred to the 0.3-1.0 range. Neither mesh is able to fully capture all the content above 0.5 present in the DTM (2×2 m).

	Maximum		Minimum		Average	
Resolution	(%)	(°)	(%)	(°)	(%)	(°)
80×80	78.04	37.97	-102.83	-45.80	0.41	0.23
40×40	95.28	43.62	-131.98	-52.85	0.41	0.23
20×20	140.70	54.60	-174.65	-60.21	0.41	0.23
10×10	195.90	62.96	-241.50	-67.51	0.41	0.23

Table 3.5: Slope (maximum, minimum and average) in the x direction with HRMap for the AOI.

The elevation error and slope along the transect passing through Towers 20, 25 and 29 (Figures 3.13, B.1 and B.2) show that the larger errors occur at locations of higher slope, and that these are the locations where the grid refinement is also the most effective in reducing the elevation error. The original 2×2 m DTM shows a lot of high frequency content that could also be undesirable for a numerical CFD model stability.

The RIX (ruggedness index) is thought to be a coarse measure of the extent of flow separation and has the goal of attempting to quantify the terrain complexity, corresponding to the fractional extent of the surrounding terrain which is steeper than a certain critical slope of 0.3 (Mortensen et al., 1993) and, thereby, the extent to which the terrain

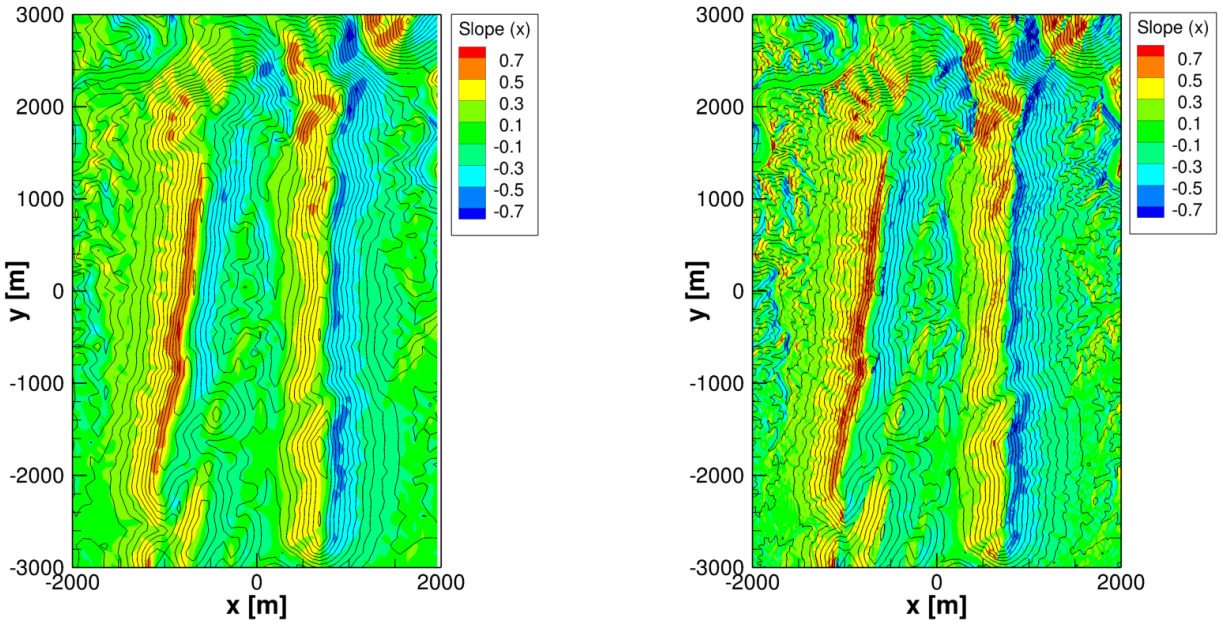

(a) 80×80 m. (b) 10×10 m.

Figure 3.11: Slope in x direction with different resolutions mapped on AOI's surface.

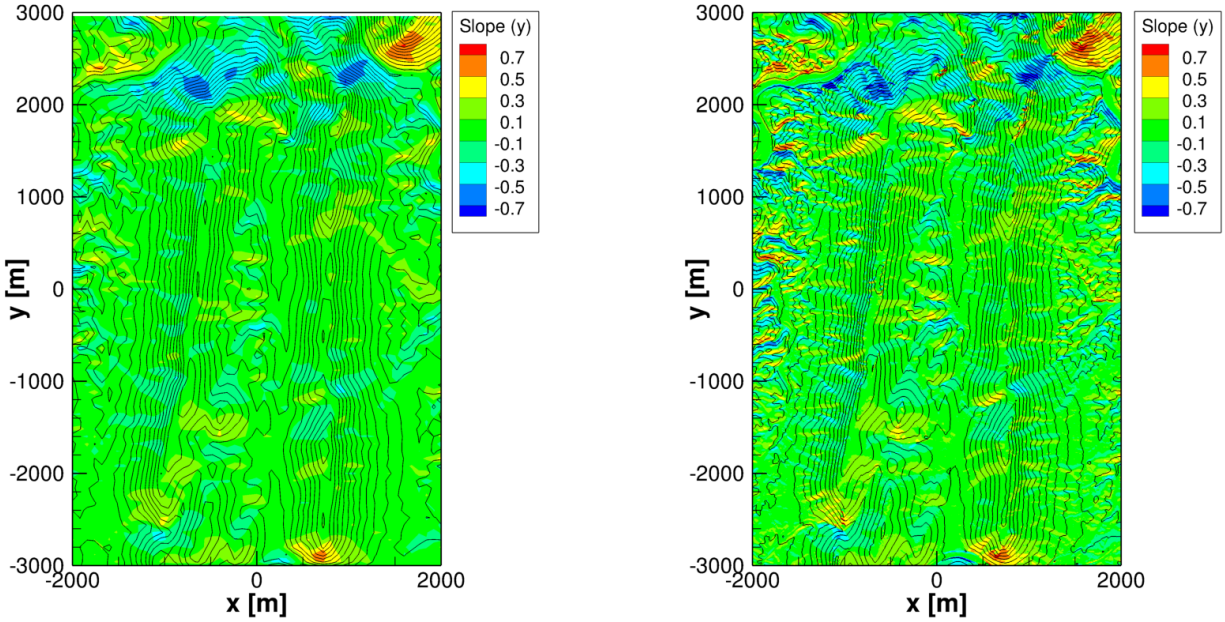

(a) 80×80 (b) 10×10

Figure 3.12: Slope in y direction with different resolutions mapped on AOI's surface.

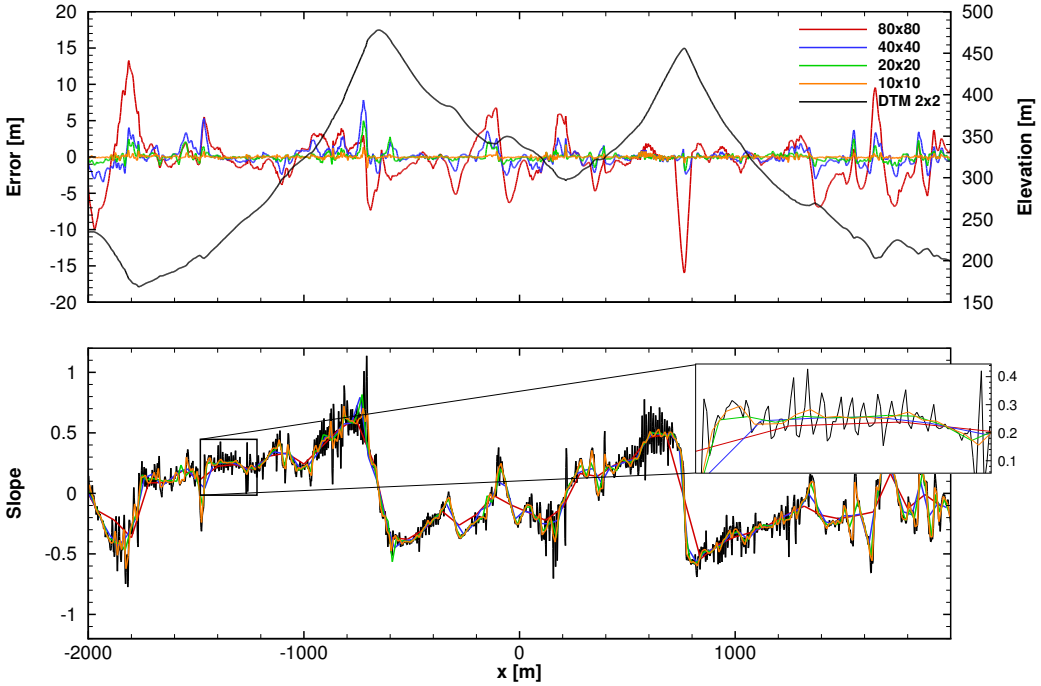

Figure 3.13: Elevation and slope in the x direction profiles on a plane that contains Tower 20.

	Tower 20	Tower 25	Tower 29	Tower 37	Wind Turbine
SRTM30	12.93	12.06	11.97	14.57	13.72
LiDAR	17.21	16.00	16.09	18.84	17.69

Table 3.6: RIX values for the 5 key points in the AOI.

violates the requirements of WAsP. The operational envelope of WAsP corresponds to a RIX value of approximately 0%.

RIX values mapped in the AOI are displayed in Figure 3.15 with the SRTM30 and LiDAR as digital elevation models. LiDAR shows a maximum of 23.7% and an overall higher value of RIX (average 15.22%), while SRTM reaches 19.7% (average 11.06%).

The values for 5 key points (table 3.6) show that the points on the southern ridge have higher values. SRTM under-predicted the values by circa 30%.

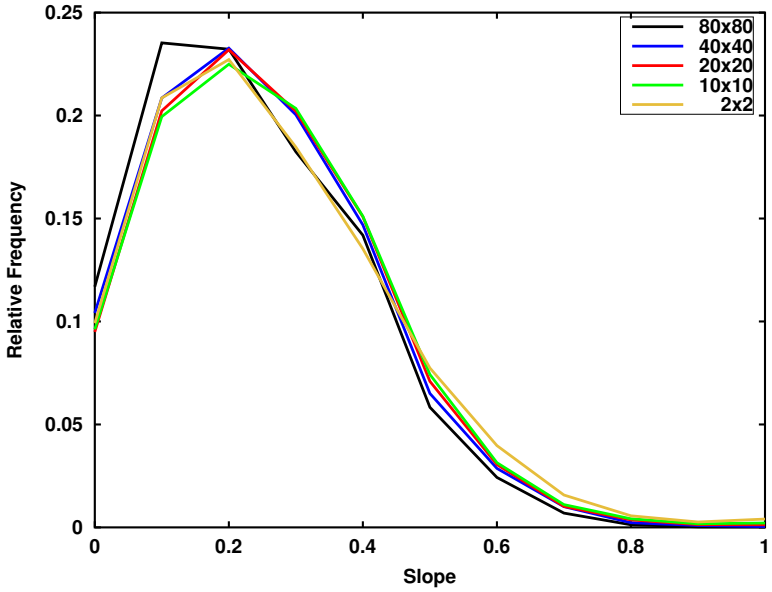

Figure 3.14: Histogram of the absolute values of the slope in the x direction for different mesh resolutions.

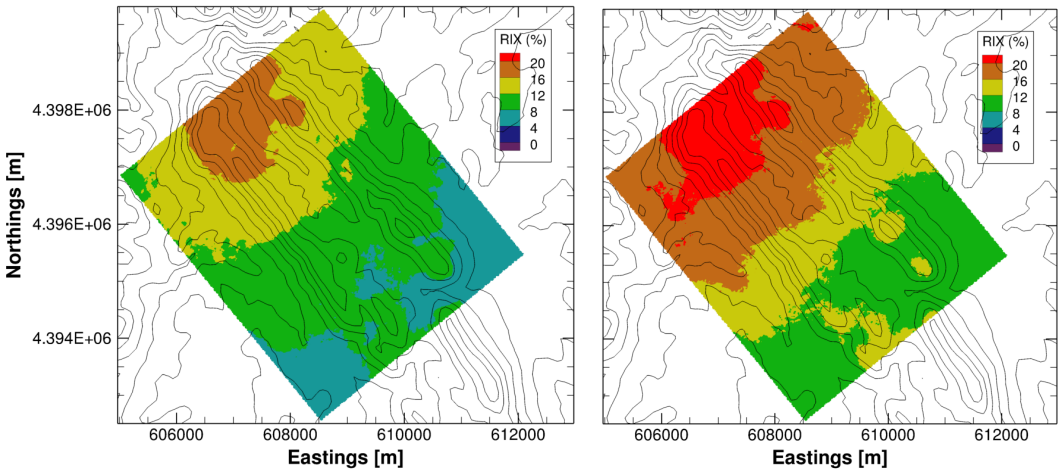

(a) SRTM30 (b) LiDAR

Figure 3.15: RIX values on the surface of the AOI with SRTM and LiDAR DEM.

3.2 Land cover model

The impact of land cover (i.e., vegetation or trees) on the atmospheric boundary layer can be modelled as increased surface friction via roughness length or explicitly via the canopy's aerodynamic drag, with a canopy model (equation 2.10 to 2.12). The latter is bound to the mesh's vertical resolution as the model requires a minimum number of control volumes to adequately represent the canopy drag. Two different sources of roughness information were considered: the LiDAR data (section 1.2.1) and Corine Land Cover, a land use classification derived from satellite data.

3.2.1 LiDAR source

The LiDAR dataset for roughness consisted of a 2 m resolution DSM (section 1.3.2) which, subtracting the DTM, produces a dataset containing measurements of the surface cover. These contain information on the vegetation height and density which are processed into various land cover model products. These include roughness length z_0 and displacement height d (Figure 3.16) estimations, made by Santos et al. (2017) through a numerical model indicated by Shaw and Pereira (1982)). Other products are vegetation height and leaf area index (LAI), displayed in Figure 3.17.

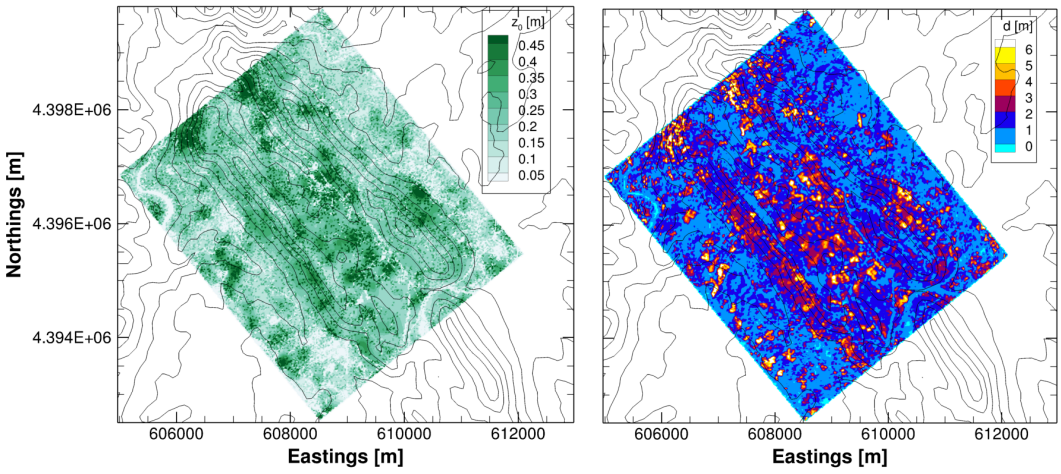

(a) Roughness length z_0

(b) Displacement height d

Figure 3.16: Roughness length z_0 and vegetation height d in the LiDAR scanning area.

There was also information on what can be called substrate roughness z_{0s}, as calculated by a typical "rule of thumb" of $0.1 \times h_{veg}$ (Garratt, 1992) for vegetated surfaces and 0.01 m for unvegetated surfaces. Although z_0 has its basis on a validated model instead of a "rule of thumb" approach, a closer look into the LAI map (3.17b) shows a lot of spikes in the distribution, i.e., a lot more discontinuities that propagate to the z_0 map and can be negative in a numerical point of view, so z_{0s} map was selected to be utilized in further simulations in the LiDAR scanning area and will from this point forward be called z_0.

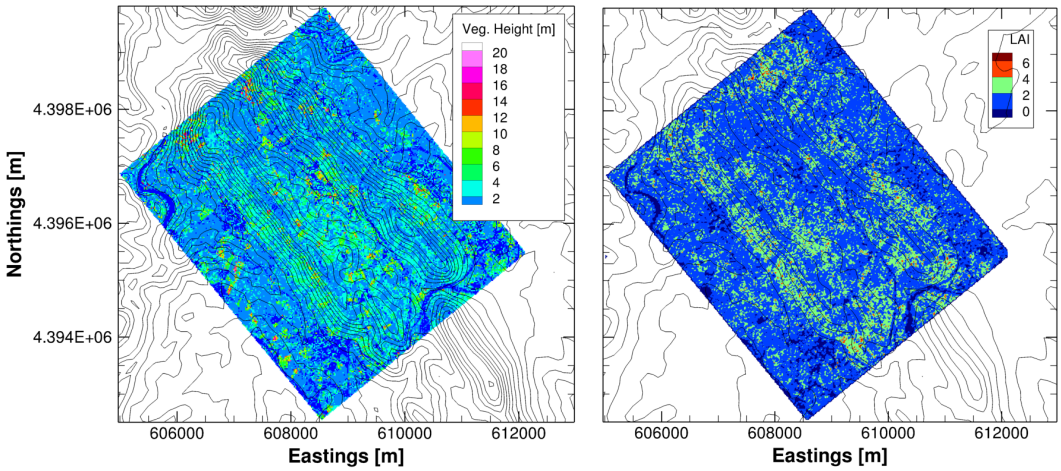

(a) Veg. height (b) LAI

Figure 3.17: Vegetation height and Leaf Area Index (LAI) in the LiDAR scanning area.

3.2.2 Corine Land Cover source

The dataset of 44 descriptive land use classes (Table A.2) available from CLC can also be utilized to provide estimations on z_0. In the present document the 2006 version will be studied to obtain a coherent comparison with other articles utilized as reference. Jancewicz and Szymanowski (2017) indicate that qualitative data (such as CLC) has to be analyzed with caution and possibly corrected, and that LiDAR-based input roughness dataset improved the model's performance and better details the spatial variability of canopy. CLC classes on the AOI are shown in Figure 3.18.

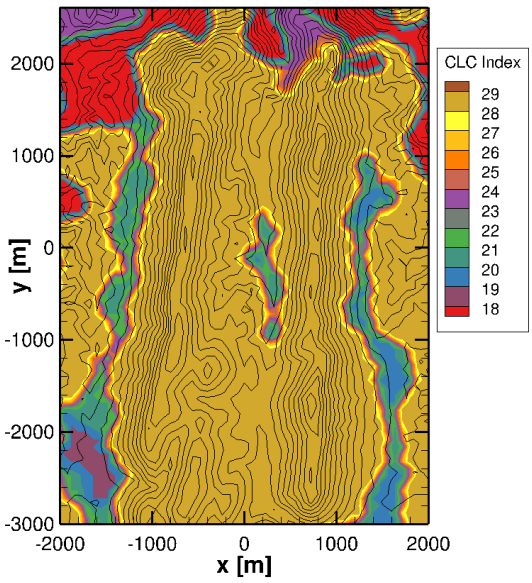

Figure 3.18: Corine Land Cover classes in the AOI.

It should be noted that any conversion from the CLC classes to roughness lengths also indirectly includes forest canopy information on the final roughness values. In this case, assuming the LiDAR as the best source of information, a map based on CLC will be used in the area outside the LiDAR scanning, with no explicitly modelled canopy.

One of the drawbacks of land use data is the equivalence between classes and roughness lengths (Floors et al., 2018; Shaw and Pereira, 1982; Pineda et al., 2004). Different conversion tables are available and lead to very different results, so its description and decision is very important. Section 3.2.2.1 describes a brief comparison on two different conversions considered.

3.2.2.1 Land cover class conversion to roughness length

In the Perdigão area scanned by the LiDAR (Figure 3.1a), Santos et al. (2017) produced a roughness length map using CLC2006 based on the convention table of Silva et al. (2007)), which will be called CLC/LNEG. In this work, another option was the conversion with default values as used by WRF (Weather Research and Forecasting model (Skamarock et al., 2008)) according the respective LANDUSE.tbl file (Pineda et al., 2004), from here on called CLC/WRF.

The main differences between CLC/LNEG and CLC/WRF map for the AOI can be consulted in Figure 3.19. It is noticeable that class 29 is predominant in the AOI (Figure 3.18), corresponding to the 324 CLC class "Transitional woodland/shrubs" (Bossard et al., 2000) or class 109 in USGS code (Pineda et al., 2004). Silva et al. (2007) indicates the difficulty to correctly assess and assign CLC 324 roughness length, which varies significantly from site to site and is one of the most representative land cover present in Portugal (around 16% of the continental area's land cover, according to recent results from CLC2012 by (Caetano and Marcelino, 2000)).

The results for the AOI using the different sources are summarized in table 3.7 and shows that the average roughness length value is, although underestimated, closer to the LiDAR scanning (0.22) when using CLC/WRF (0.12) than by using CLC/LNEG (0.51). Ultimately, CLC/WRF has the advantage of being coherent with mesoscale simulations that will naturally accompany the experiment and micro-scale simulations on the Perdigão site. Therefore, the map utilized in further simulations to complement the LiDAR scanning data is the CLC/WRF and will only be called CLC from this point forward.

	$\overline{z_0}$	$z_{0_{max}}$	$z_{0_{min}}$
LiDAR scan.	0.22	0.53	0.01
CLC/LNEG	0.51	0.75	0.1
CLC/WRF	0.12	0.5	0.06

Table 3.7: Roughness length (maximum, minimum and average) considering different sources.

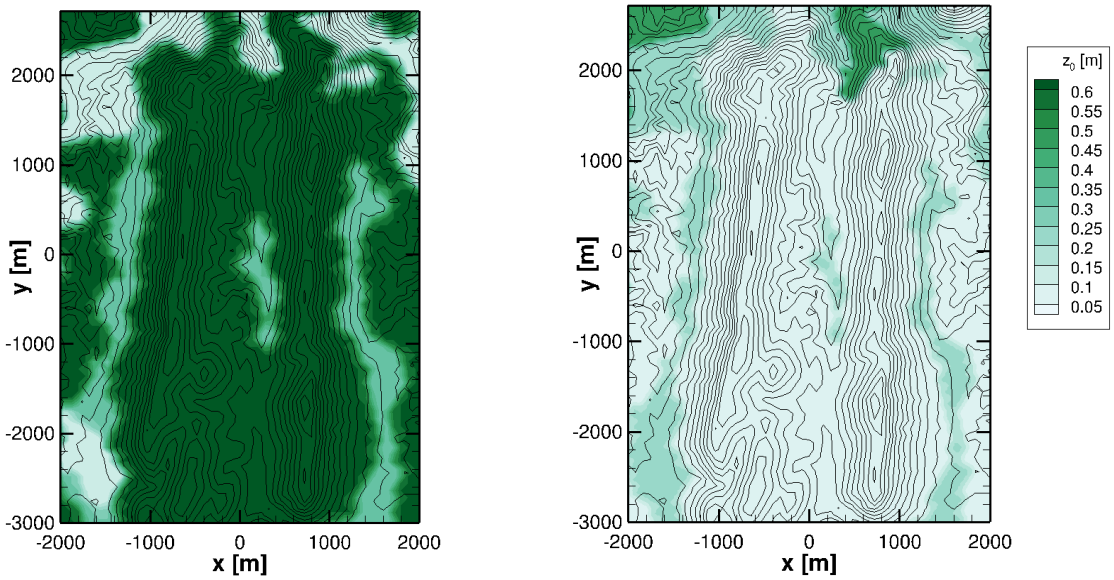

(a) CLC/LNEG (b) CLC/WRF

Figure 3.19: Different Corine Land Cover class conversion to roughness length values.

3.2.3 Explicitly modelled canopy

From the vegetation height map (Figure 3.17a) the cut-off height on roughness representation has to be chosen, i.e., the height above which the forested regions are treated by the canopy model (equations detailed in Chapter 2). Any discussion on how to determine that height is vague, and with little information available on that topic.

The representation of surface cover via canopy model is largely dependent on the vertical resolution of the mesh and the number of control volumes. Vertical resolutions of 2 m used in this document (sections 4.4 and 4.5) do not have the capability of representing low vegetation, so a vegetation height of 5 m is thought to be a compromise cut-off height on roughness representation.

Assuming the typical rule of thumb that vegetation can be represented in terms of roughness as 10% of its height (Garratt, 1992), 5 m height leads to a z_0=0.5 m, which is below the height of the first control volume (considering 2 m vertical resolution). This roughness length value was the maximum represented via increased roughness length.

This vegetation height value of 5 m was also supported by the fact that the displacement heights (Figure 3.16b) estimated through the previously mentioned numerical model are above 2 m for most of the domain, thus exceeding the numerical capability of its representation.

The definition of the canopy model based on the vegetation that exceed 5 m of height and the different zones to consider on the computational model are described in the following section.

3.2.4 Canopy zones

To fully define the canopy model, four zones (Figure 3.20) were characterized based on different height ranges converted into their mean value to represent each zone after a detailed observation on the LiDAR scanning map that contained the vegetation height in the area.

A map containing information on Leaf Area Index (LAI, Figure 3.17b) showed values of circa 2 in general, but low values (under 0.5) in areas of high vegetation height values, showing low correlation between vegetation height and LAI values, and that the high LAI values are probably associated with dense shrubbery and grass. A uniform LAI value of 2 was considered across the domain, leading to different Leaf Area Density (LAD, the total one-sided leaf area per unit volume) values for each zone.

A summary of the canopy information for each zone considered is detailed in Table 3.8. A canopy drag coefficient value of 0.2 was used, as recommended by Santos et al. (2017). Figure 3.20 shows that the canopy introduced to the model is mostly part of zone 1 and 2, with only some sparse small regions being characterized as zone 3 and 4 as result of the small amount of very tall canopy in the region.

	Zone 1	Zone 2	Zone 3	Zone 4
h_{int} [m]	[5;7.5]	]7.5;12.5]	]12.5;17.5]	]17.5;22.5]
h_{can} [m]	6.25	10	15	20
LAD [m^2/m^3]	0.320	0.200	0.133	0.100

Table 3.8: Height and LAD considered for the canopy.

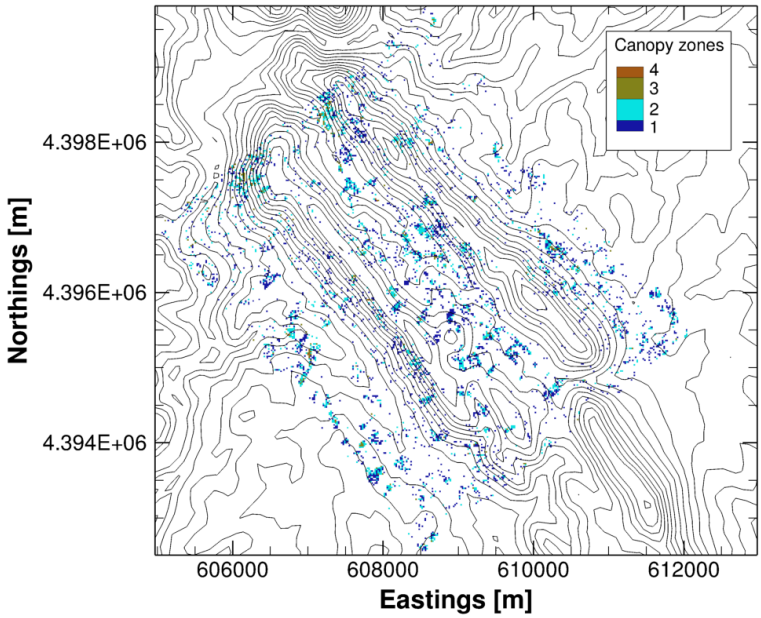

Figure 3.20: Canopy zones.

3.2.5 Summary of roughness representation

A final roughness map can be produced by complementing the roughness lengths obtained by the LiDAR scanning in the AOI with the map CLC/WRF, to provide a larger domain for simulation. This new roughness map had the z_{0s} estimation as a basis, using those values where vegetation height was below 5 m. The value for areas that were inside canopy zones were reduced to 0.01 m, as indicated by Shaw and Pereira (1982) to avoid modelling canopy in duplicate (increased roughness length and momentum sink by explicit canopy model).

The final roughness map with an extended domain (Figure 3.21a) shows that the SW side of the domain has higher values than the NE side, which gives an indication of possible different roughness influence to SW and NE winds. A closer look at the center of the domain shows the mixing region (Figure 3.21b) between the LiDAR data on the AOI and the CLC/WRF data for the remaining domain, and that there is a good blend between both sources.

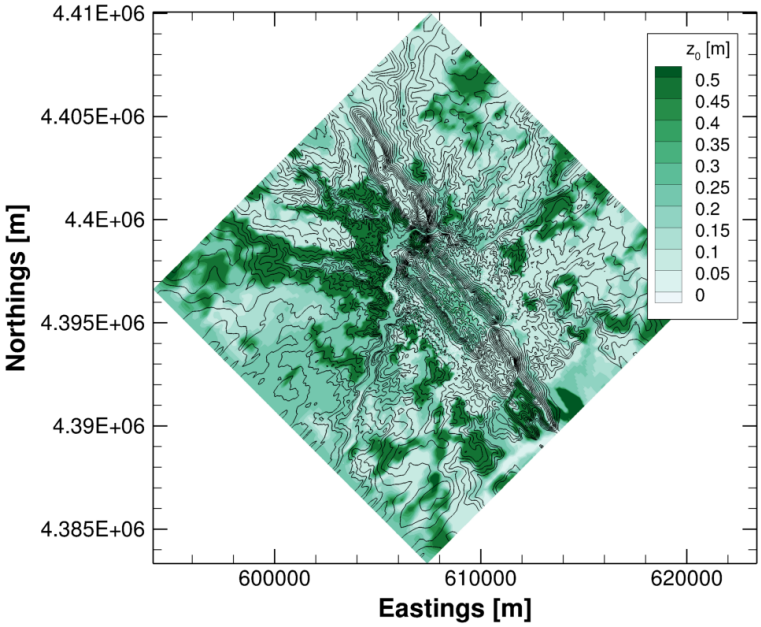

(a) Roughness map with larger domain

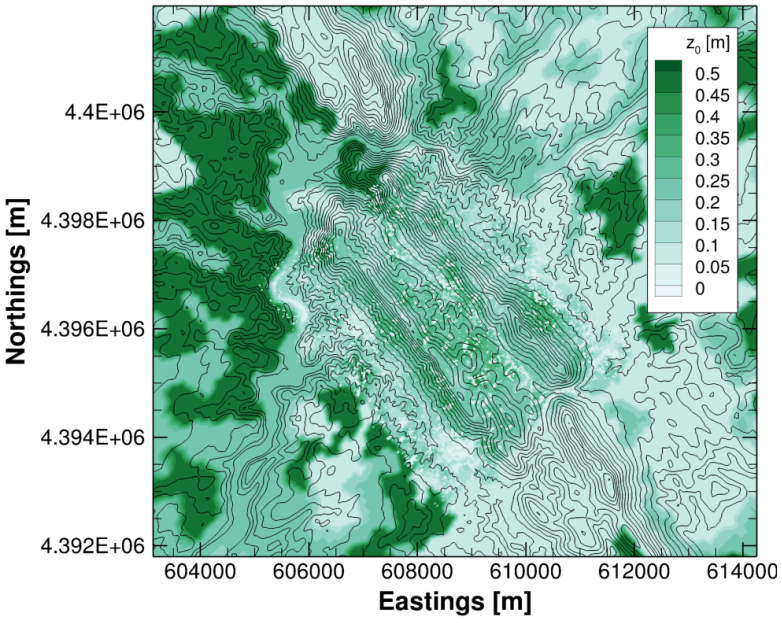

(b) Mixing region between both roughness length maps

Figure 3.21: Roughness map with a large domain and a zoom on the mixing region between both roughness maps (LiDAR on the AOI + CLC).

3.3 Conclusions

This subsection summarizes the conclusions about the terrain and surface cover analysis and representation, the comparison between different sources and the effect of mesh horizontal resolution. The main conclusions were the following:

Digital terrain models

- The SRTM30 was not sufficient to accurately represent the terrain and severely limits the use of higher resolution meshes.
- The spectral analysis for the HRMap shows a significant increase in high frequency content, as horizontal resolution increases. Only meshes based on the HRMap have the ability to reproduce the high-frequency range.
- the spectral analysis for SRTM30 m shows larger decay at high frequencies, as it extrapolates beyond the resolution of its source.
- the HRMap is the source with lower elevation errors all over the domain, showing a RMSE above 5 m for 80×80 m, that drops as low as 0.5 m with 10×10 m. The RMSE for SRTM 30 m does not go under 4 m.
- a 40×40 m horizontal resolution based on the HRMap is enough to achieve an error below 1 m in the five key locations, and below 0.5 m for 20×20 m.
- slope in the x direction proved to be sensitive to mesh resolution, with a maximum slope about 2 × higher (140.70 and 195.90) on a 20 or 10 m mesh resolution compared with an 80 m mesh resolution (78.04).
- profiles that cross each 100 m tower show that 80×80 m mesh resolution does not accurately represent elevation and slope, particularly near the extreme elevation values.
- the ruggedness index (RIX) shows an average value of 11.06% for SRTM 30 m and 15.22% for LiDAR. SRTM 30 m under-predicts the RIX for the five key points by circa 30%.

Surface cover model

- CLC class 324 roughness length is predominant in the double ridge area and is known to be of difficult conversion to roughness length, varying from site to site;
- the average roughness length value is, although underestimated, closer to the LiDAR scanning (0.22) when using CLC/WRF (0.12) than by using CLC/LNEG (0.51);
- CLC/WRF was used to complement the LiDAR roughness data set to produce a roughness map with a larger domain;

- vegetation and canopy were modelled by an increased roughness length up to a 5 m vegetation height and by a canopy model, for vegetation above that height;
- four canopy zones with different height ranges were defined, leading to sparse canopy areas in the whole domain and a small amount of vegetation in zones 3 and 4.

Chapter 4

Flow model: results and discussion

In this chapter, the results on the flow modelling are displayed. Numerical mesh parameters, domain size and land cover representation are part of a parametric study based on wind speed, direction and turbulent kinetic energy.

In section 4.1 a parametric study to define domain boundary positions for the computational model is conducted, while section 4.2 presents general flow patterns in Perdigão as a first insight. The method of comparison with experimental data from the Perdigão campaign is described in section 4.3. Results for digital terrain model comparison and land cover sources, and the impact on physical variables are discussed in section 4.4 and 4.5. Some details on turbulence intensity, vertical inclination and shear factor for the wind turbine location are analyzed (section 4.6) and the chapter ends (section 4.7) with the main conclusions.

4.1 Simulation setup

4.1.1 Case list

A summary of the simulations run, using different combinations of numerical mesh, DTM and land cover data are displayed in Table 4.1 along with a reference name for each, a total of 19 cases.

Meshes with horizontal resolutions of 80×80, 40×40 and 20×20 m were generated for both SW and NE wind directions (this last one just for SW winds), combining different DTM (SRTM30 or HRMap, section 3.1) and, based exclusively on the HRMap DTM, land cover data (CLC/WRF or CLC/WRF+LiDAR, section 3.2).

		DTM		Land cover		Numerical Mesh		
	Name	SRTM30	HRMap	CLC	CLC+LiDAR	80×80	40×40	20×20
SW	SRTM30.SW.80	x				x		
	SRTM30.SW.40	x					x	
	SRTM30.SW.20	x						x
	HRMap.SW.80		x			x		
	HRMap.SW.40		x				x	
	HRMap.SW.20		x					x
	CLC.SW.80		x	x		x		
	CLC.SW.40		x	x			x	
	RougCan.SW.80		x		x	x		
	RougCan.SW.40		x		x		x	
	RougCan.SW.20		x		x			x
NE	SRTM30.NE.80	x				x		
	SRTM30.NE.40	x					x	
	HRMap.NE.80		x			x		
	HRMap.NE.40		x				x	
	CLC.NE.80		x	x		x		
	CLC.NE.40		x	x			x	
	RougCan.NE.80		x		x	x		
	RougCan.NE.40		x		x		x	

Table 4.1: Simulation cases.

4.1.2 Computational domain

The size of the computational domain and location of its boundaries were varied individually, analyzing the influence of each on the results at the area of interest (namely in the five key points, section 3.1.2) and convergence of the fluid flow algorithm.

For each boundary, multiple simulations were performed for different distances (Figure 4.1 for the entry boundary of SW winds) to the domain center (coordinates 608250E 4396621N). This exercise was repeated for both predominant wind directions in the region (SW and NE). The DTM used was the SRTM 90 m with a 80×80 m horizontal resolution on the constant resolution area, expanding towards boundaries (see Section 2.3 for domain mesh structure). Smaller domains, i.e. smaller distances from center to boundaries imply less mesh nodes and a lower computational effort and therefore should have priority. It is also important that the boundary lies on smooth terrain to avoid complex flows near it, for numerical stability purposes. The computational domain in Gomes (2012) was used as a reference to initiate this study.

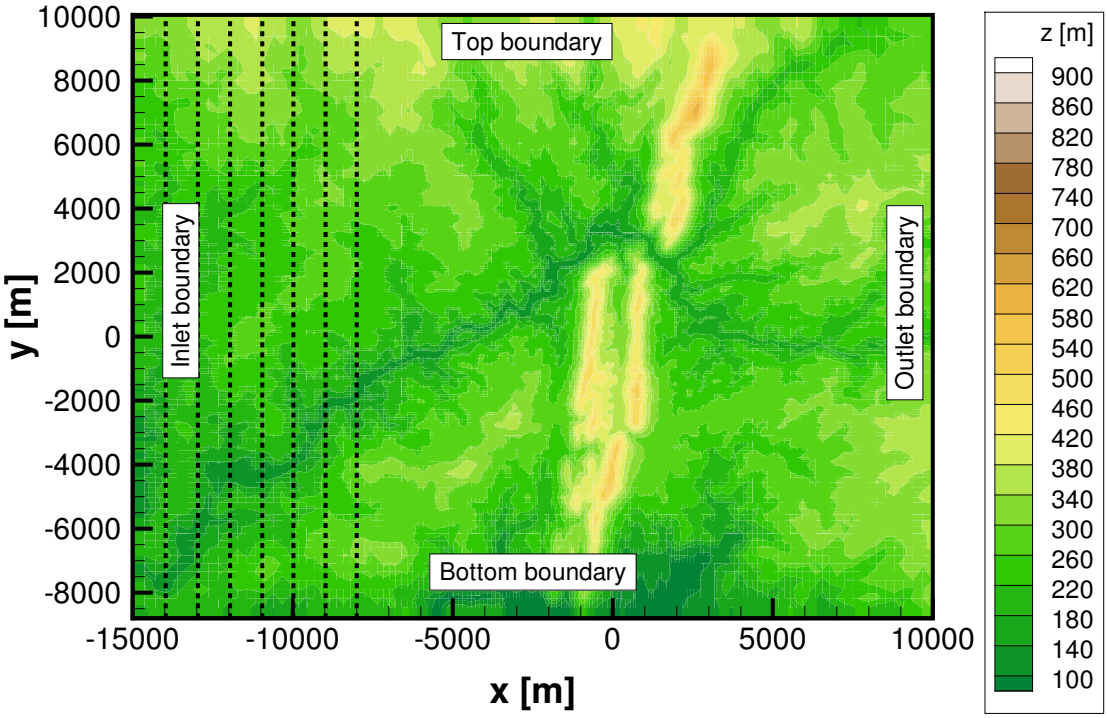

Figure 4.1: Computational domain study, different inlet boundary positions for SW winds. Boundary positions (inlet/outlet and top/bottom) reversed for NE winds).

Results for the four boundaries considering SW winds are represented in Figure 4.2 for different boundary positions (for example, 8 to 15 km distance between the centre and the inlet boundary), in Tower 20. The behaviour was similar to the remaining key points (all documented in appendix C) for the four boundaries in each of the five points.

The wind speed and turbulent kinetic energy were the main variables analyzed. Only the inlet boundary has noticeable impact on wind conditions at Tower 20. Wind

speeds are stable up to boundary distances of 12 km, after which they show some increase. Despite the bottom boundary having no influence on the AOI, a closer look to the results near the boundary shows that local complex flows can be the source of some numerical convergence difficulties in this analysis, specially in this bottom boundary. The reason behind it can be related to the local geological formation of complex topography, known as Portas de Ródão. These numerical convergence problems were due to either the simulation not achieving the residuals criteria (although stabilizing) or numerical divergence.

After finishing this analysis for all of the boundaries in both wind directions considered, the final domain (Figure 4.3) to use in further simulations in this work is the one represented in Table 4.2. Since the domain center indicated is the same for both wind directions, the considered solution was to invert the boundary position to each direction, this way the total domain size remains the same for SW and NE winds.

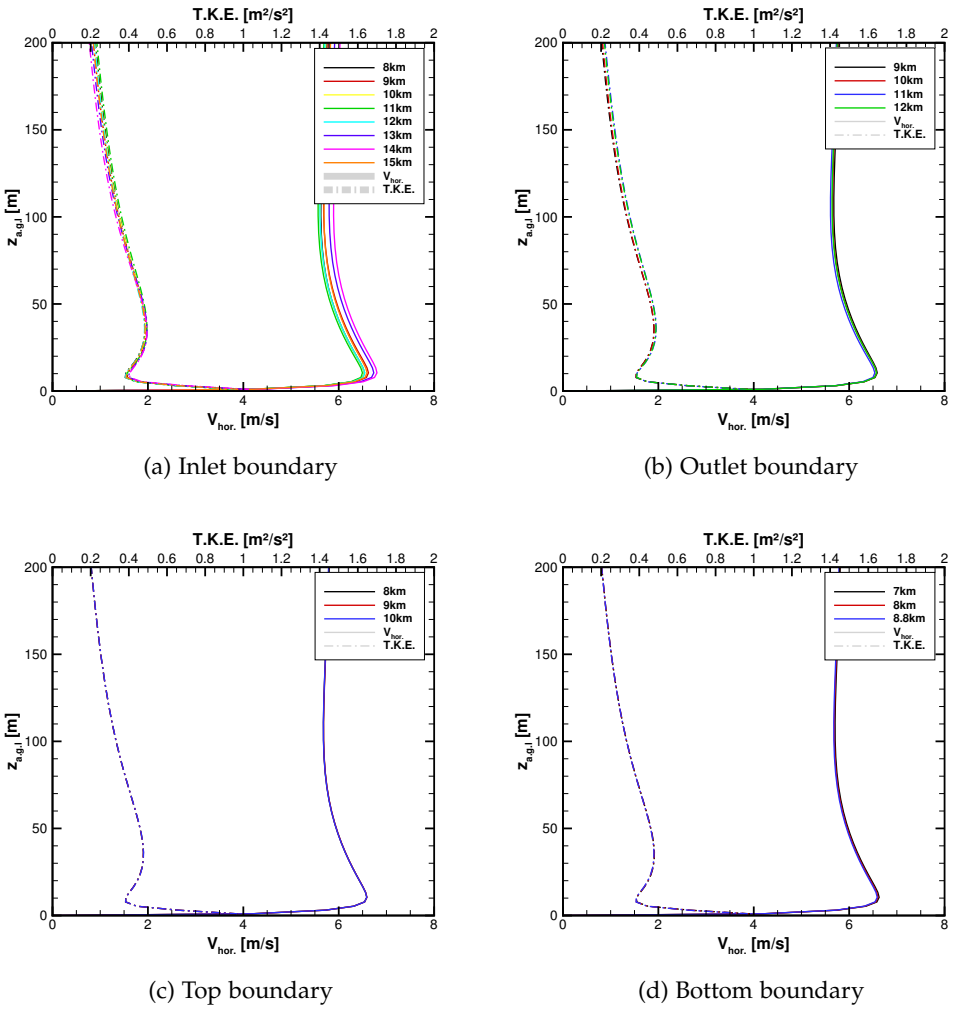

(a) Inlet boundary

(b) Outlet boundary

(c) Top boundary

(d) Bottom boundary

Figure 4.2: Simulation results for different boundaries for SW winds, Tower 20.

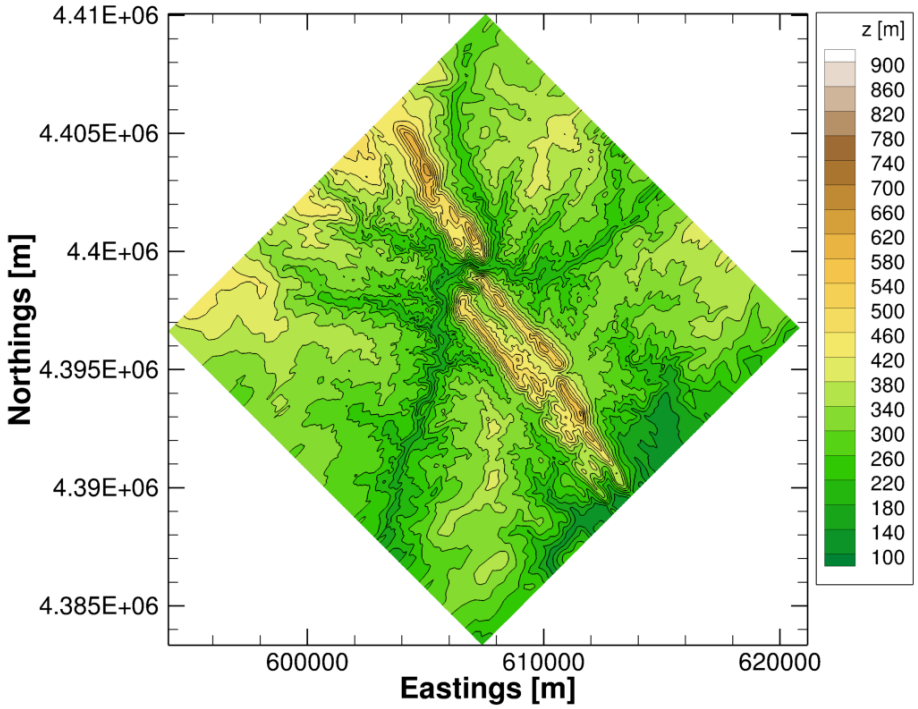

Figure 4.3: Representation of the computational domain for further simulations.

	SW winds	NE winds
Inlet [m]	-10000	-9000
Outlet [m]	9000	10000
Bottom [m]	-8800	-10000
Top [m]	10000	8800

Table 4.2: Computational domain to use on further simulations.

4.2 Flow over Perdigão: general flow pattern

Before analyzing the results at the reference locations (section 4.4 and 4.5) the general flow pattern over Perdigão is shown for SW and NE winds (section 4.2.1 and 4.2.2), a first insight on the type of structures that develop in the region with the visual aid of streamlines coloured by the wind speed.

Velocity profiles across different sections (Figure 4.4) on the double ridge were also made across Tower 32, 20, 37 and 39 (ordered by Southeast-Northwest direction). Towers 32 and 39 (20 m height towers) were chosen because they correspond to the most south and northern instrumentation on the southern ridge, so that the flow is analyzed with more detail on a larger area. The different sections are distanced 550-600 m from each other (detailed in Table 4.3, circa 1.7 km total).

Reference points were chosen to describe flow patterns with more detail (Table 4.3 in the northern ridge (n), southern ridge (s) and valley (v). Points n_1 and n_2 were chosen because they are located in gaps where the northern ridge ends in both sides and n_2, n_3 and n_4 because they correspond to elevation peaks in the northern ridge. Points s_1, s_2,

	Eastings [m]	Northings [m]	Elevation [m]
Tower 32	608159	4395639	472
Tower 20	607818	4396091	473
Tower 37	607508	4396515	482
Tower 39	607151	4396967	488
s_1	606677	4397454	439
s_2	607277	4396783	482
s_3	608466	4395306	493
s_4	608816	4394734	474
v_1	607514	4397318	299
v_2	608375	4396411	343
v_3	609481	4395336	377
n_1	607003	4399352	179
n_2	610569	4394807	352
n_3	608096	4396783	482
n_4	609033	4396902	456
n_5	609959	4395945	532

Transect	Distance [m]
32-20	579
20-37	559
37-39	564

Table 4.3: Coordinates of reference points for general flow pattern figures and the distance between the transects in Figure 4.4.

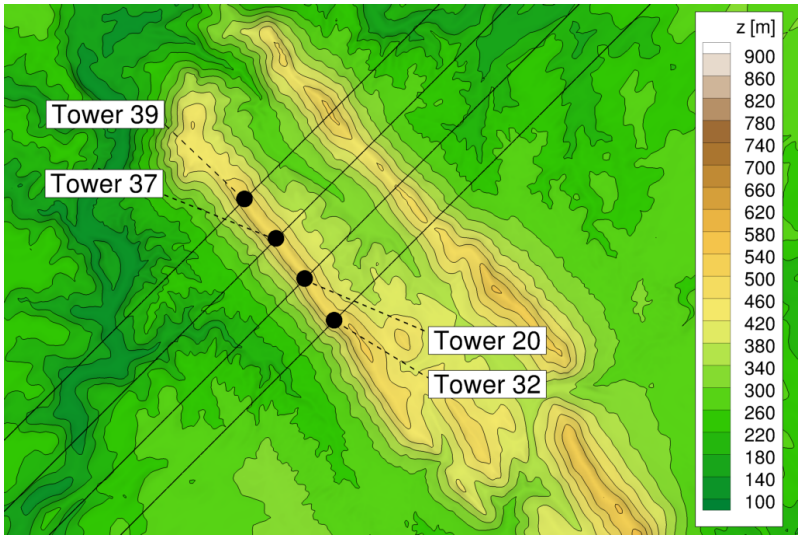

Figure 4.4: Transects that cross Tower 32, 20, 37 and 39.

s_3 and s_4 cover the southern ridge and its elevation peaks. In the valley, v_2 is located somewhere in its middle, while v_1 and v_3 comprise the more northern and southern valley region, respectively.

4.2.1 Southwesterly winds

For SW winds (Figure 4.5) the flow in the central area of the southern ridge (between s_2 and s_3) goes mainly over the valley, almost neglecting its presence, leaving a lower pressure area in the valley (relative to the ends of the ridges). This lower part of the valley is filled from both sides of the southern ridge (Figure 4.5a, between points s_1 and s_2, and s_3 and s_4, probably due to their difference in elevation, circa 40 and 20 m, respectively, with gaps between them) and forms big recirculation zones (columnar-like vortices) with the flow direction being parallel to the ridges. These two streams meet in the middle of the valley area (Figure 4.5b, point v_2), showing some symmetry to the flow structure. The flow then exits the valley area over the northern ridge, mainly through the centre (Figure 4.5b, point n_4).

The areas immediately outside the ends of the double ridge have gaps where the flow accelerates through (Figure 4.5c, points n_1 and n_2) and forms jet-like streams. In these areas the flow forms many complex vortex structures, such as spirals, on the downstream side of the site that have impact on the northern ridge's wake.

Wind flow profiles on vertical cross-section passing through Tower 32, 20, 37 and 39 are presented in Figure 4.6 and 4.7. Velocity components u and w (stream-wise and vertical) are displayed in the form of vectors, while v (cross-stream) is in the form of contour (positive direction of v means Southeast-Northwest, or v_3-v_1 orientation). A dashed line corresponding to the isoline $u = 0$ traces the wind profile inversion along the transect.

The v velocity component reinforces what was visible in Figure 4.5. Tower 32 (Figure D.3c, south extreme of the southern ridge) shows mostly positive v values on the valley

(flow going on the v_3-v_1 direction), while Tower 39 (Figure D.6c, north extreme of the southern ridge) shows negative v values close to the valley's surface (flow going on the v_3-v_1 direction), meaning that mid-valley the mean flow inverts its direction from going down to going up the valley.

The v velocity component also reveals inversion of direction with height. This behaviour is found in the deeper parts of the valley and near the ends of the ridges (Figure D.3c and D.6c).

Results that consider the surface cover and canopy zones (Figure 4.7) do not affect the general trends, although v values are lower in general.

The detached flow areas (below the isoline $u = 0$) show different behaviours along the ridge. As expected, it occurs right after reaching the peak of the southern ridge. While for most of the sections reattachment occurs mid-valley when approximating the northern ridge, when adding variable roughness and explicitly canopy modelling, the transect that crosses Tower 37 (Figure 4.7c) shows that the flow remains detached even after crossing the northern ridge.

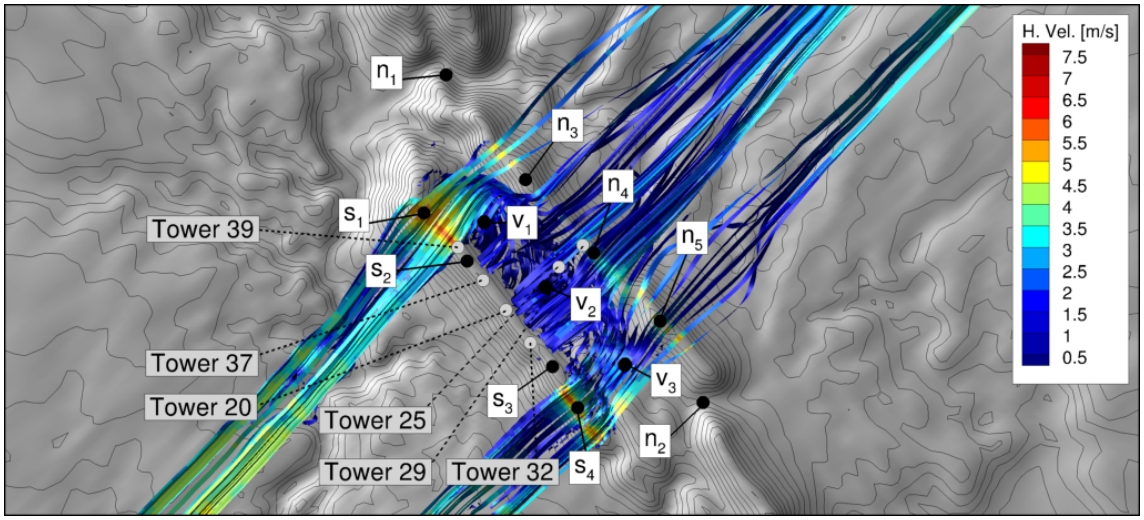

(a)

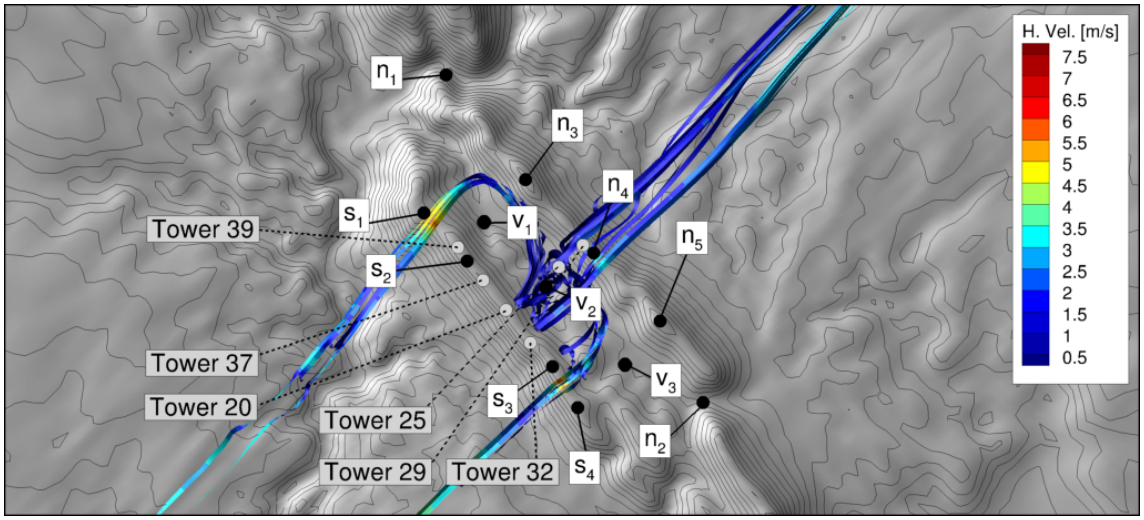

(b)

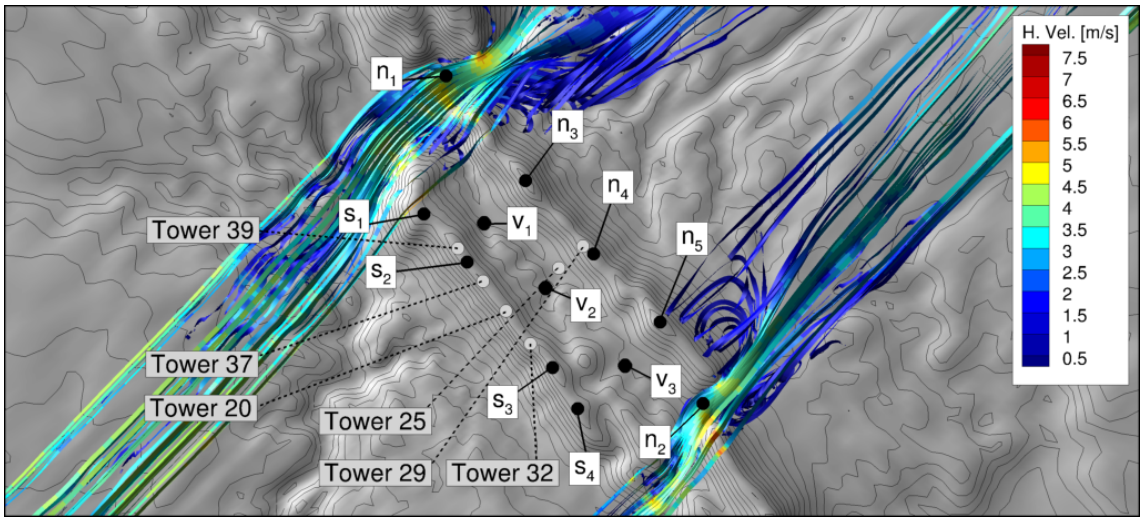

(c)

Figure 4.5: Flow patterns for SW winds.

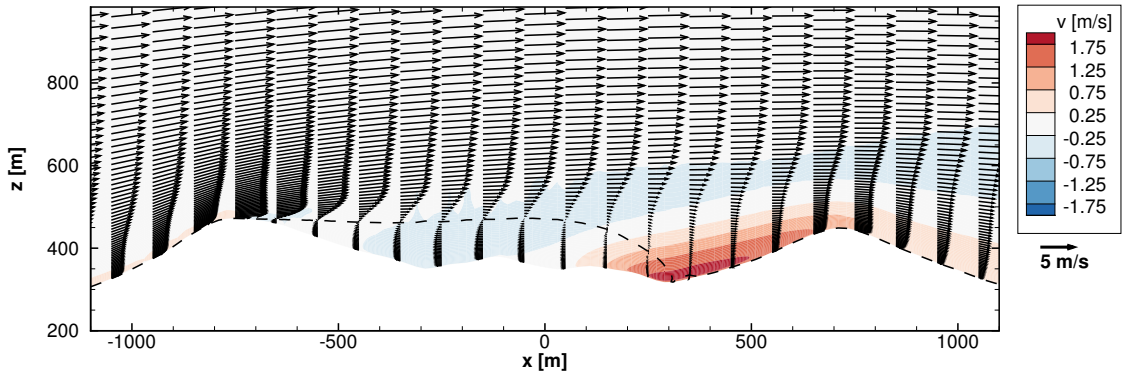

(a) Tower 32

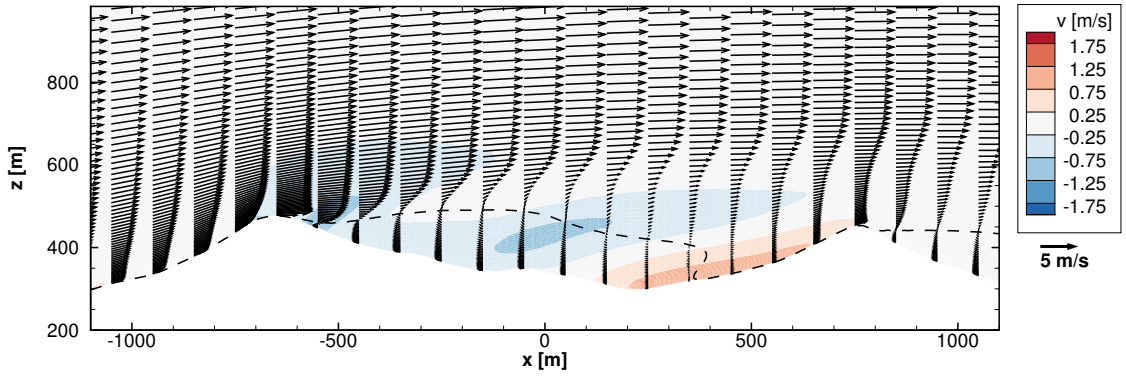

(b) Tower 20

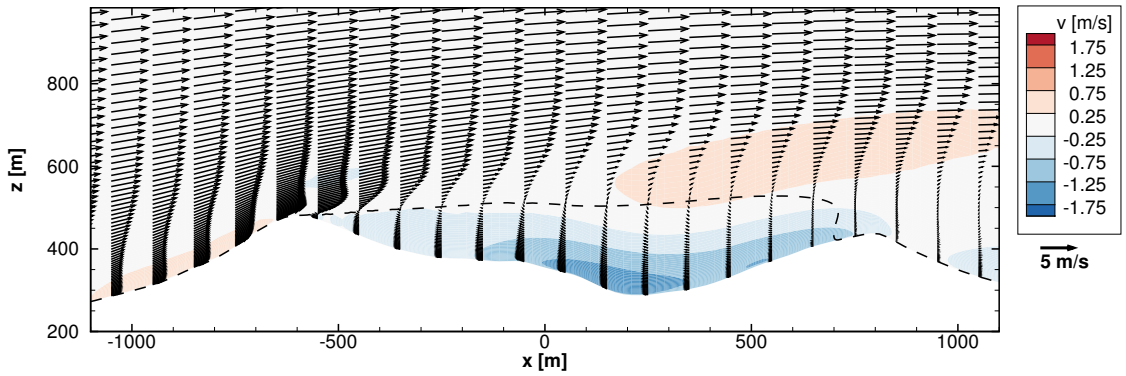

(c) Tower 37

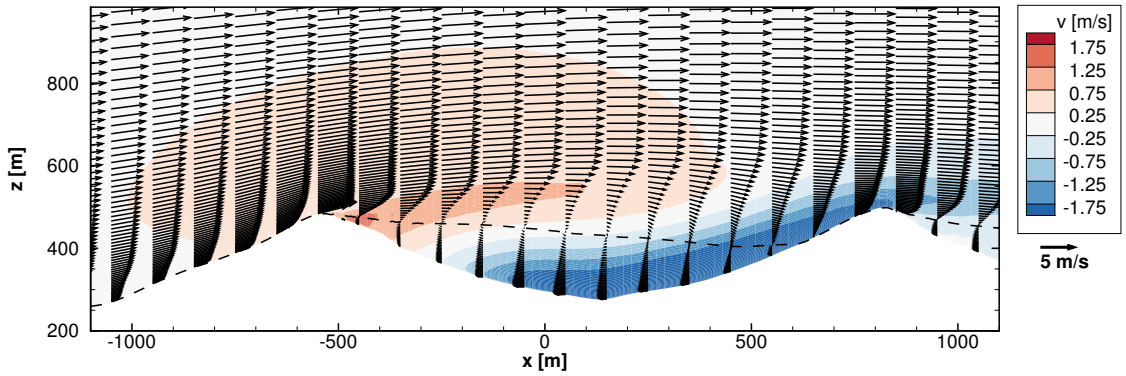

(d) Tower 39

Figure 4.6: Wind velocity profile along the double ridge using results from HRMAP.SW.20.

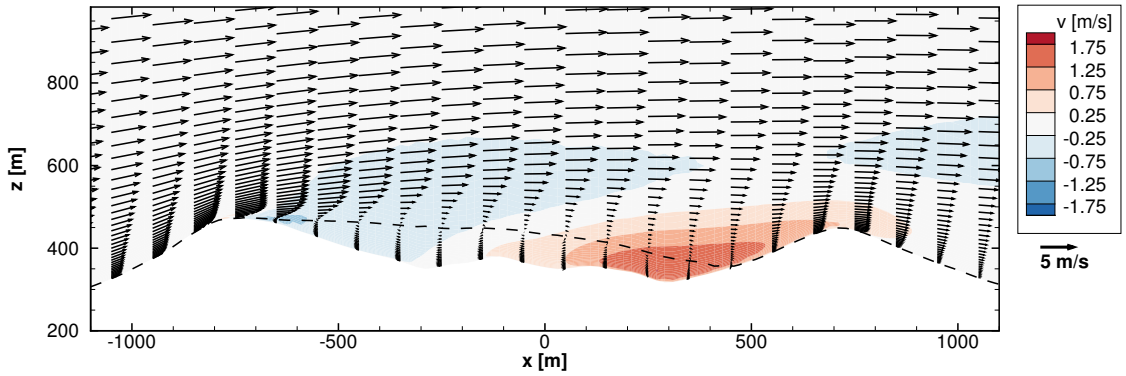

(a) Tower 32

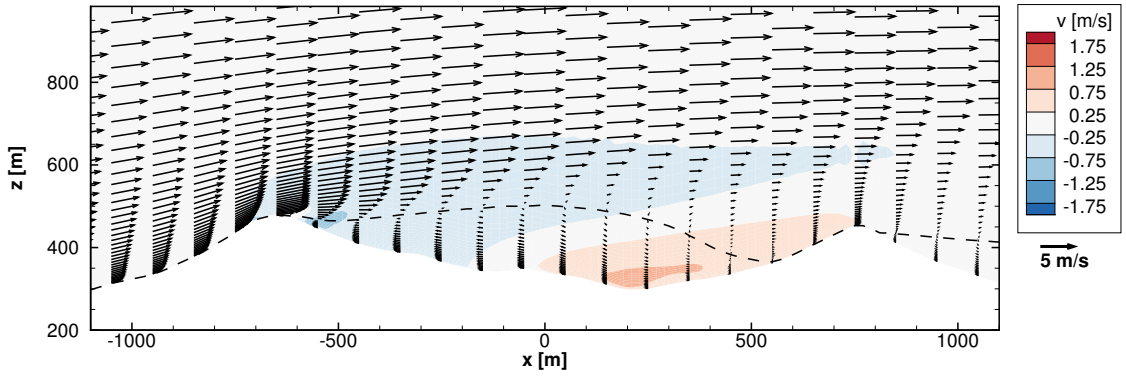

(b) Tower 20

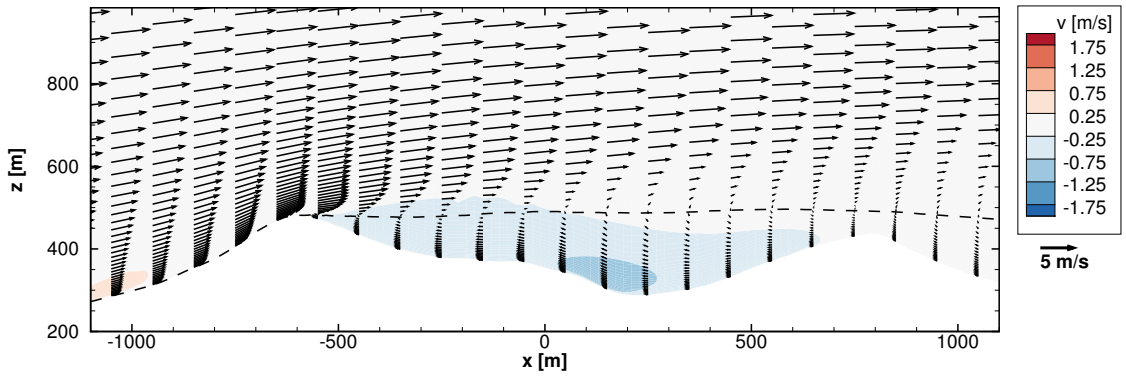

(c) Tower 37

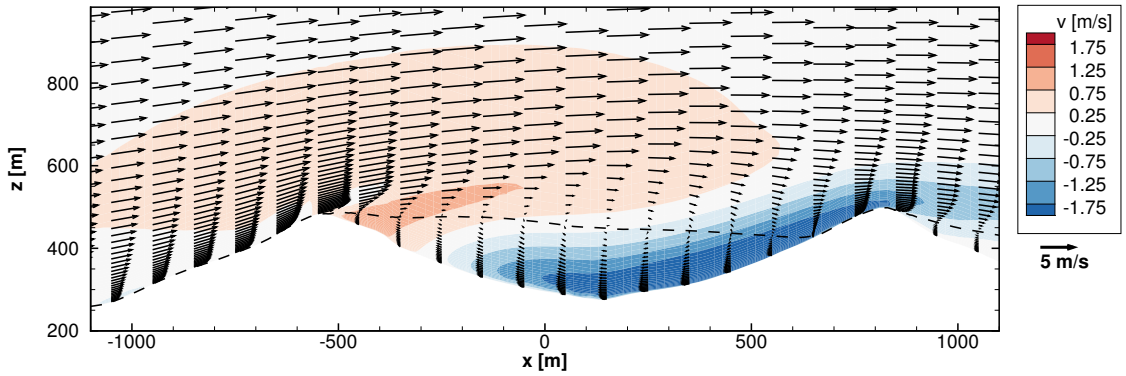

(d) Tower 39

Figure 4.7: Wind velocity profile along the double ridge using results from ROUGCAN.SW.20.

4.2.2 Northeasterly winds

Figure 4.8 reveals some flow patterns involving the double ridge for predominant NE wind direction. As equally observed for SW winds, part of the flow goes above the double ridge (Figure 4.8c), over the complex valley area. The flow that fills the low pressure valley area (relative to the ends of the ridges) comes mostly from the gap on the south (Figure 4.8b, point n_2).

Figure 4.8b shows that the recirculation zones that form in the valley then go above the southern ridge, mainly through the gap between points s_1 and s_2 (meaning that the flow goes down the valley). A part of the flow that comes from the south gap (n_2) also escapes between s_3 and s_4 instead of going down the valley. The two gaps on the double ridge's ends (Points n_1 and n_2) accelerate the flow and form jet-like streams (more noticeable on the North side), also contributing to the southern ridge's wake.

The v velocity component shows different behaviour than for SW winds. Values near the valley's surface (at least between Tower 32 and 39, most of the valley's length) are either positive (flow going on the v_3-v_1 direction direction) or near zero when approaching the north of the valley (near v_1), which confirms the conclusion that for NE winds most of the flow that fills the valley comes from the Southwest gap (point n_2) and continues down the valley (Figure 4.8b).

As equally observed in SW winds, v values also change from positive to negative with height (Figure 4.9a), although in less extent as positive v values are predominant in the valley for NE winds.

As expected, flow detachment occurs right after reaching the peak of the northern ridge (Figure 4.9). In the section that crosses Tower 39 (Figure 4.9d) the whole valley between the two ridge's peaks shows detached flow. It is noticeable that the recirculation zone in the valley (confined by the dashed line) grows from Tower 32 to Tower 39 (Southeast-Northwest direction), as the northern ridge height grows relative to the south's.

The addition of surface cover largely eliminates negative v velocity areas inside the valley (Figure 4.10).

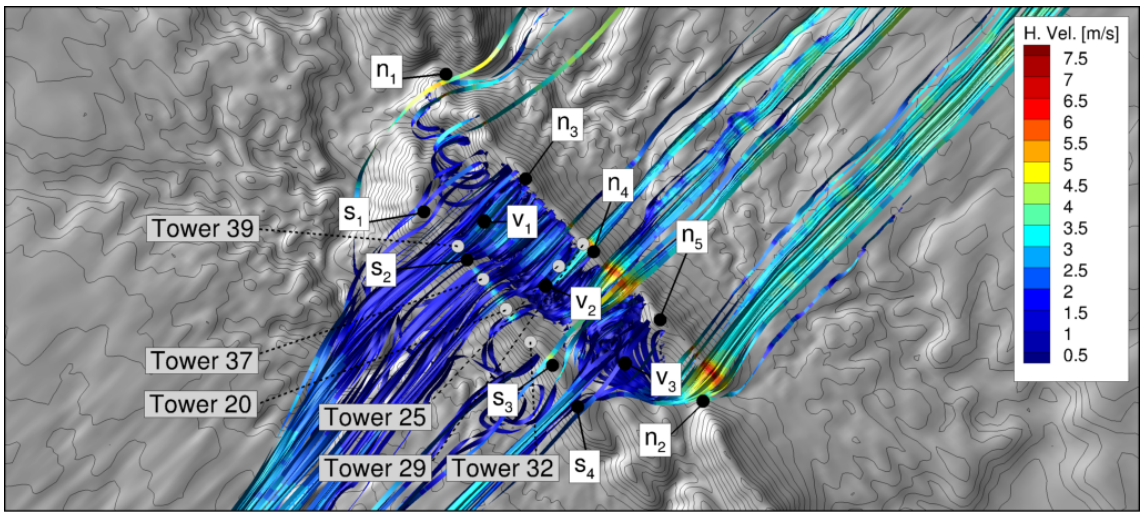

(a)

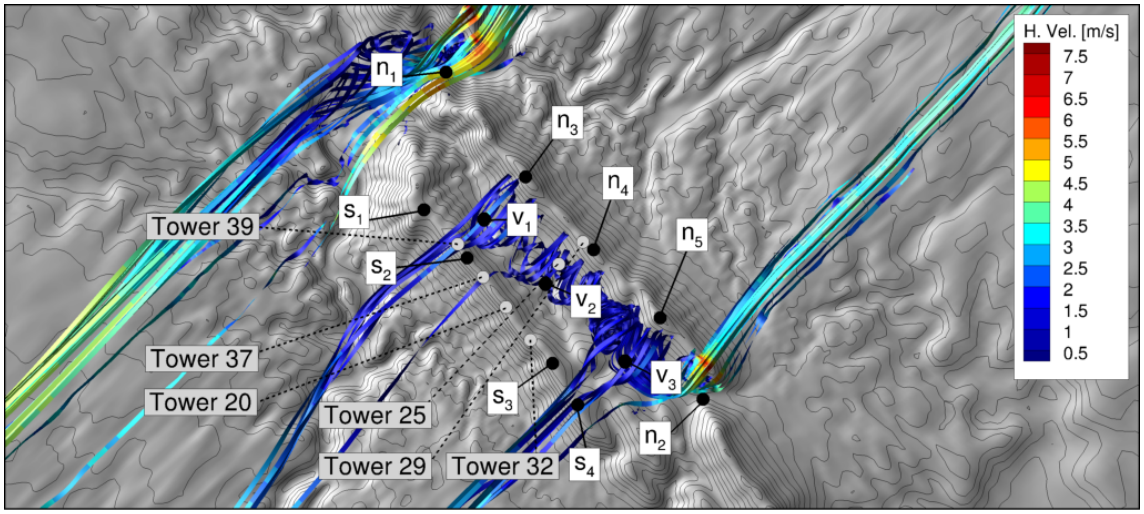

(b)

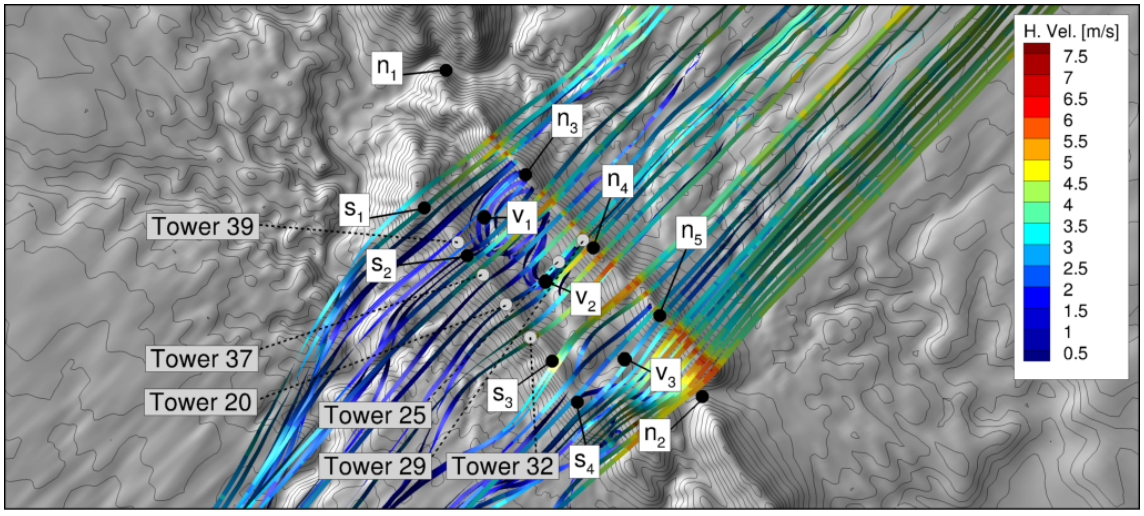

(c)

Figure 4.8: Flow patterns for NE winds.

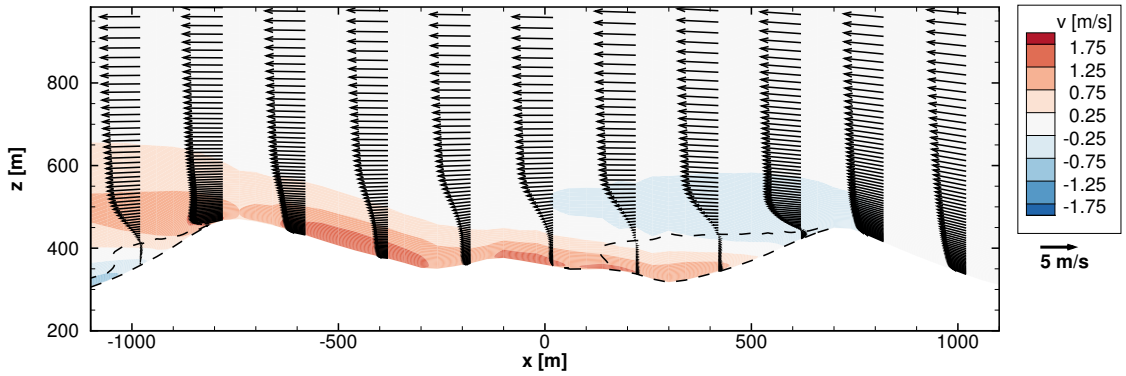

(a) Tower 32

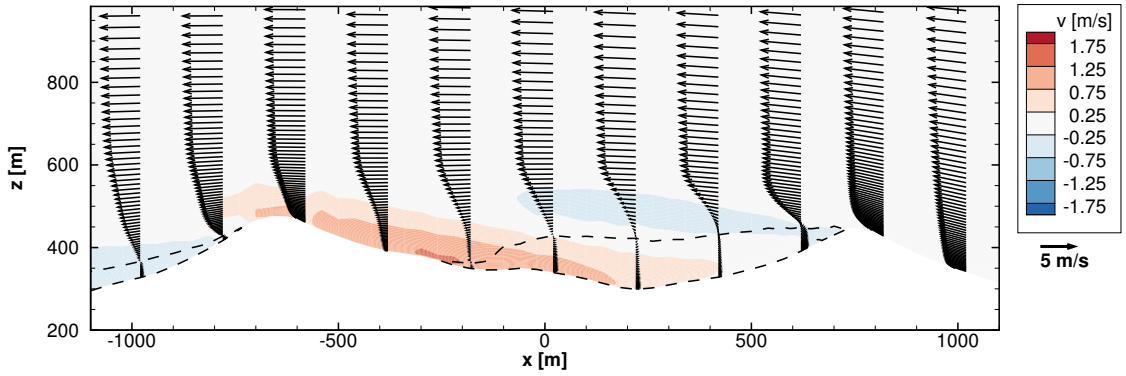

(b) Tower 20

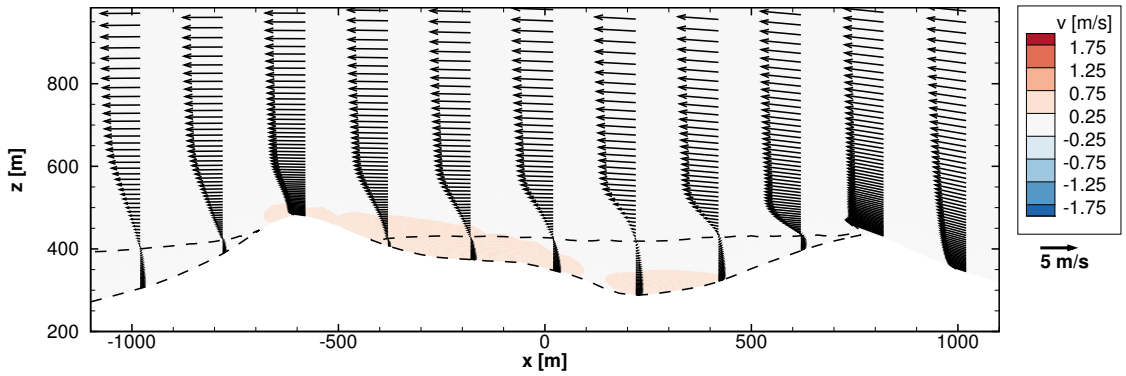

(c) Tower 37

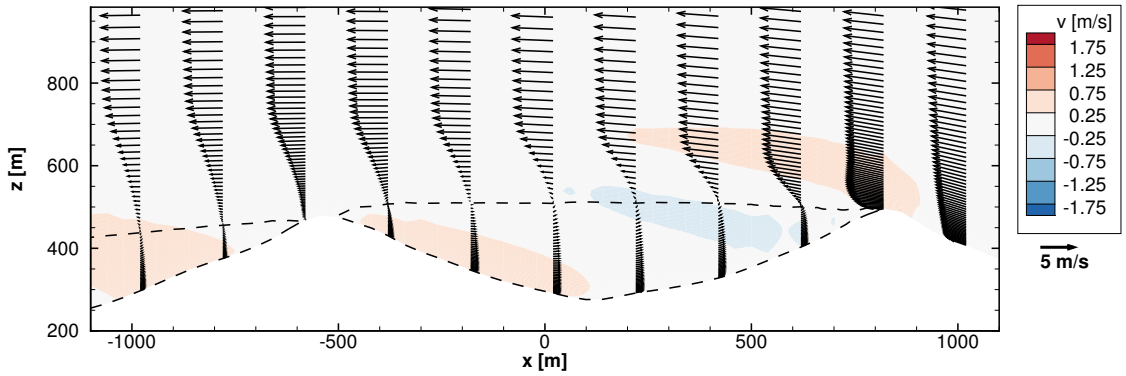

(d) Tower 39

Figure 4.9: Wind velocity profile along the double ridge using results from HRMAP.NE.40.

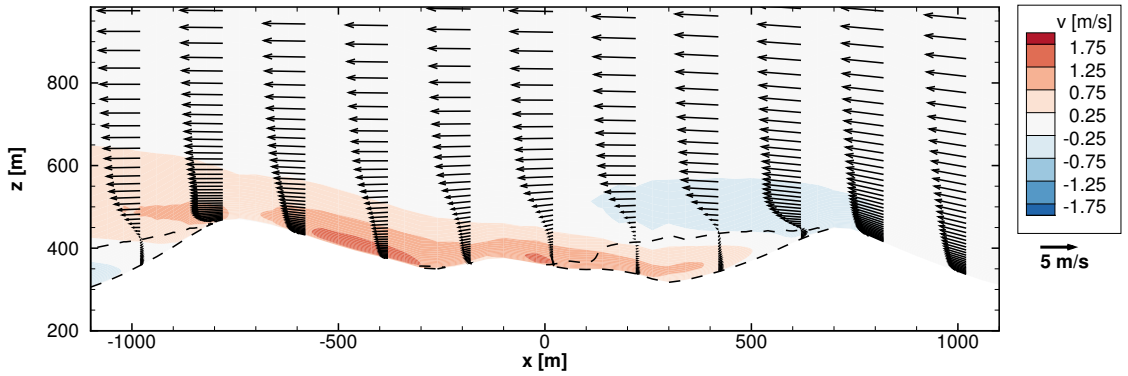

(a) Tower 32

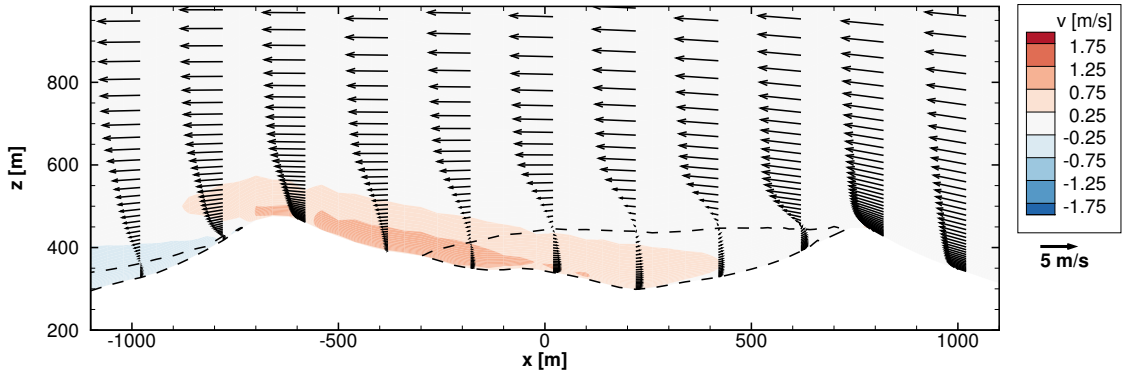

(b) Tower 20

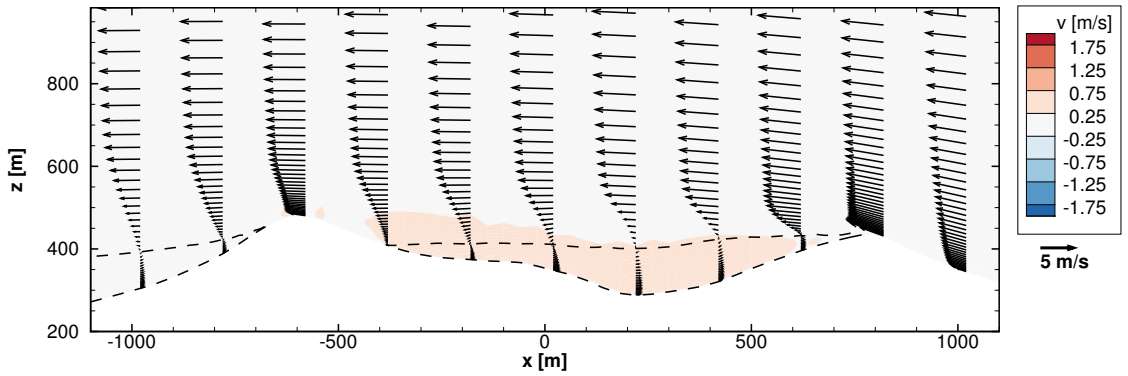

(c) Tower 37

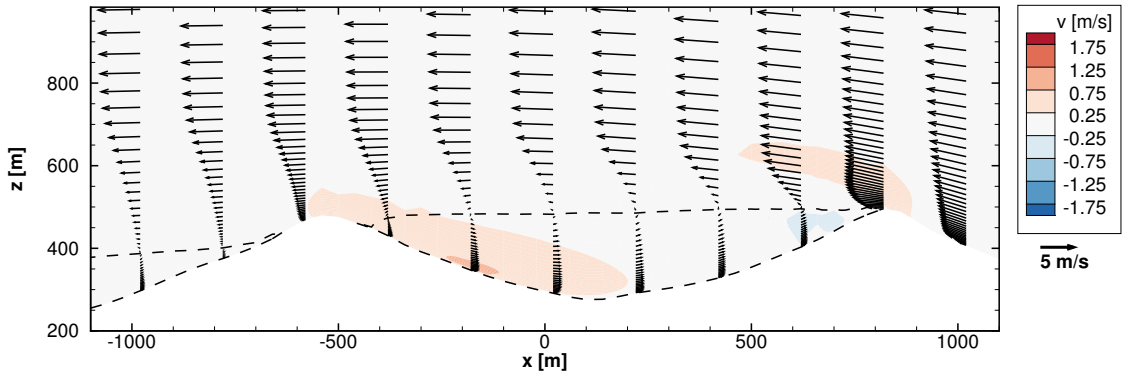

(d) Tower 39

Figure 4.10: Wind velocity profile along the double ridge using results from ROUGCAN.NE.40.

4.3 Comparison with measurements

The sequential increase in complexity of the flow model ultimately had the goal of comparison to experimental results obtained from the Perdigão campaign.

As an initial approach, filters were applied to the experimental data based on horizontal velocity, wind direction and shear factor at 100 m above ground level at Tower 20, used as a reference. The filtered time periods were noted and the synchronized data for Towers 25, 29 and 37 and their measurements at different heights were registered and plotted with the simulation results.

Vilaça (2018) deals on the post-processing of the Perdigão experimental data and indicates that the comparison with the computational results requires the identification and extraction of stationary periods within the experimental data. This is "based on the fact that the flow must be stationary during a period of time long enough for a fluid element to travel through the whole length and to every fluid element, passing through the same location, to experience identical conditions", dependent on domain size and wind speed.

For a characteristic length equal to the domain size used (circa 19 km), considering an average wind speed of 6 m/s, Vilaça (2018) indicates that six consecutive 10-minute periods (filtered by visual inspection and a set of criteria based on a more statistical approach) are required to fulfill the stationarity condition. Wind direction would then be filtered to be SW (225 $\pm$ 15 °) or NE (45 $\pm$ 15 °).

In the present document, only results for SW winds will be compared with experimental data in wind speed and direction profiles in the following sections (4.4 and 4.5).

Southwesterly winds

The criteria was defined by observing the simulation results for Tower 20, for SW winds, in 100 m a.g.l. This lead to a criteria of 6 $\pm$ 0.5 m/s wind speed, wind direction of 225 $\pm$ 15 ° and moderate shear of 0 $\pm$ 0.1.

A period of May 4^{th} (wind direction, horizontal velocity and temperature throughout the day observed in Figure 4.11) met the criteria and was chosen with an interval of 1h of consecutive data, from 21h40 to 22h30, with a wind speed of 5.8 m/s, wind direction of 234.3° and -0.03 shear. In Vilaça (2018), part of the instrumentation indicates that in the Perdigão campaign, May 4^{th} oscillates between a stable and unstable atmosphere close to same time period previously mentioned. The synchronized data from the remaining towers was averaged for that time interval and plotted with the computational results in sections 4.4 and 4.5.

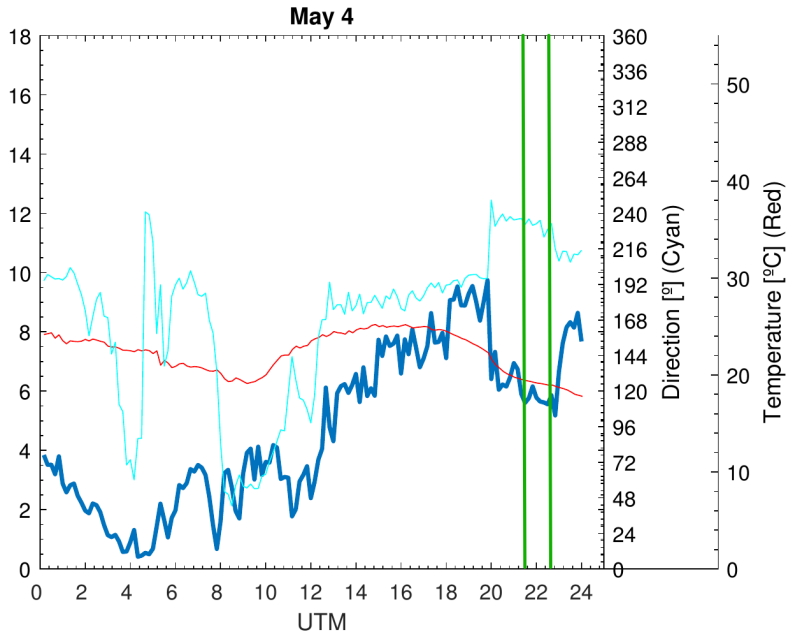

Figure 4.11: Experimental wind speed, temperature and wind direction on May 4th for Tower 20 (100 m a.g.l.). Selected stationary period marked in green.

4.4 Numerical mesh (DTM)

This section aims to quantify the impact of using different DTM and numerical meshes on wind speed, direction and turbulent kinetic energy. The computational results in this section were obtained using SRTM 30 m or HRMap with different numerical meshes (Table 4.4).

The details include a domain (Figure 4.3) of circa 19×19 km, 3 km high, a constant horizontal resolution at AOI expanding towards boundaries, homogeneous roughness $z_0 = 0.03$ m (open grass land), friction velocity of $u^* = 0.23$, no surface cover modelling and a neutral atmosphere. A closer look to the structured terrain-following mesh is presented in Figure 4.12.

Table 4.4 shows the different case names, the numerical parameters and the duration (in hours) of each simulation, showing that the selection on the computational mesh has to be a compromise between the results accuracy and the computation effort. For 20×20 m horizontal resolution, the vertical number of nodes had to be increased in order to achieve convergence.

Southwesterly winds

The computational results are displayed in the form of horizontal velocity, wind direction and turbulent kinetic energy profiles in the five key points.

Tower 20 (Figure 4.14) at 50 m a.g.l. shows that differences between DTMs at the same resolution in horizontal velocity are all under 0.25 ms^{-1}, while differences greater than 0.5 ms^{-1} can be reached between mesh refinements, particularly 80×80 m

	$\Delta_{x/y}$ [m]			Δ_z [m]			
Name	Min	Max	$n_i \times n_j$	Min	Max	n_k	t_{CPU} [h]
SRTM30.SW.80	80	458.9	120×145	2	223.6	60	0.96
SRTM30.SW.40	40	378.3	200×270	2	226.2	60	7.24
SRTM30.SW.20	20	396.2	320×470	2	118.2	100	*
HRMap.SW.80	80	458.9	120×145	2	223.6	60	0.96
HRMap.SW.40	40	378.3	200×270	2	226.2	60	7.39
HRMap.SW.20	20	396.2	320×470	2	118.2	100	*
SRTM30.NE.80	80	458.9	120×145	2	223.6	60	0.74
SRTM30.NE.40	40	378.3	200×270	2	226.2	60	*
HRMap.NE.80	80	458.9	120×155	2	223.6	60	0.59
HRMap.NE.40	40	378.3	200×270	2	226.2	60	*

*Duration not registered or incomplete because pre-defined convergence criteria were not met; runs were user interrupted when numerical convergence was deemed satisfactory.

Table 4.4: Mesh parameters details used on the simulation.

to 40×40 m. This would lead to the conclusion that mesh resolution has a greater impact than the change of DTM. At 80×80 m horizontal velocity profiles show negative shear, absent from experimental results.

Tower 37 (Figure 4.13) shows higher differences (at the same height) in horizontal velocity when using different DTMs with finer meshes. For example, while the coarser 80×80 m shows almost null differences between SRTM 30 m and HRMap, 20×20 m shows circa 1 ms^{-1} or more difference. The turbulent kinetic energy profiles also present similar sensitivity to resolution, responding differently to mesh refinement for the two DTMs.

In both towers, using the improved DTM and finer meshes cause lowered wind speeds and degraded match to experimental data, particularly at Tower 37. The wind turbine, as it is located in the southern ridge between Tower 20 and 37, shows similar results (Figure D.1), so the previous conclusion also stands for this location.

As Tower 37 and 20 are located on the southern ridge before the complexity of the valley flow, wind direction was thought to not vary much from the inflow. The wind direction profile in both towers supports the previous statement showing negligible variations in the first 200 m, deviating a maximum of 12° for Tower 20 and 8° for Tower 37 and matching the experimental data. Impact of DTM and mesh resolution for both towers only shows on the first 150 m above ground level.

Tower 25 (Figure 4.15) shows much greater impact from changes in DTM and mesh resolution. As it is located in the valley, where the flow shows to be more complex (Figure 4.5a), Tower 25 shows very low horizontal velocities (generally under 1 ms^{-1} and typical of recirculation zones). All profiles agree on these values (corroborated by experimental data), diverging only above 100 m.

These low horizontal velocities are also associated with big variations of wind direction that stabilize on the SW sector (circa 225°) only above 200 m above ground level. The direction prediction is noticeably stabilized by the swap to HRMap, consistently

matching the trend established by the experimental data.

Tower 29 (Figure 4.16) located in the northern ridge, past the valley) shows big variations of turbulent kinetic energy (different cases differ a maximum of 1 $m^2\ s^{-2}$). Its wind profile (in opposite to the southern ridge towers) shows higher values when using HRMap as DTM, while when using SRTM 30 m negative shears appear and differences only became negligible above circa 170 m above ground level.

When comparing the experimental data from May 4^{th}, computational results still lack effects of modelling land cover representation, stratification and other phenomena so it should not be considered a fully accurate representation of the flow. Nevertheless, computational results generally under-predicted horizontal velocity but qualitatively showed a satisfactory approximation to wind direction profiles for the four towers (also showing big variations with height at Tower 25) and horizontal velocity (for the southern ridge towers).

In general, wind flow direction was the least sensible variable, almost indifferent to the DTM or mesh resolution (with the exception of Tower 25).

The impact of the DTM used was greater for higher mesh resolutions. However, in locations affected by the valley's flow complexity (Tower 25 and Tower 29), the response to mesh refinements for different DTM was different, diverging with SRTM whereas HRMap remains more stable.

Figures D.3 to D.6 showed that mesh refinement from 80×80 m to 40×40 m generally led to an increase of the extent of the recirculation zone, and to the separation point occurring earlier along transects that cross double ridge. 20×20 m resolution was not consistent with this trend (the higher number of vertical nodes could affect the direct comparison between resolutions).

Northeasterly winds

Similar profiles but for Northwesterly winds were taken for all 5 key points, in function of DTM and mesh resolution.

Tower 29 (Figure 4.20, located in the northern ridge and thus on the upstream side of the valley) was the least affected by the change in DTM with converged results beyond 50 m above ground level. It showed only small differences, caused by refining the mesh from 80×80 m to 40×40 m.

For the southern ridge locations, in this case more affected by the valley's flow complexity, Towers 37 and 20 (Figure 4.17 and 4.18) showed that the DTM change has a noticeable impact on horizontal velocity (differences as high as 2 ms^{-1} or 40% reduction when using HRMap instead of SRTM 30 m at 50 m a.g.l.) and turbulent kinetic energy (differences of 0.5 m^2s^{-2} or 70% increase when using HRMap at 50 m a.g.l.). The wind turbine (Figure D.2) has results very similar to Tower 20 and thus conclusions for that location are the same.

Flow behaviour regarding Tower 25 (Figure 4.19) is very similar to SW winds, with very low horizontal velocities in the first 100 m (generally under 1 ms^{-1}) and big variations of wind direction that stabilize on the NE sector (circa 45^o) only above 200 m above

ground level. Again the DTM is the dominant factor for change in profile shape.

Flow direction was (as equally concluded for SW winds) the least sensible variable to the change in DTM and mesh resolution (with the exception of Tower 25).

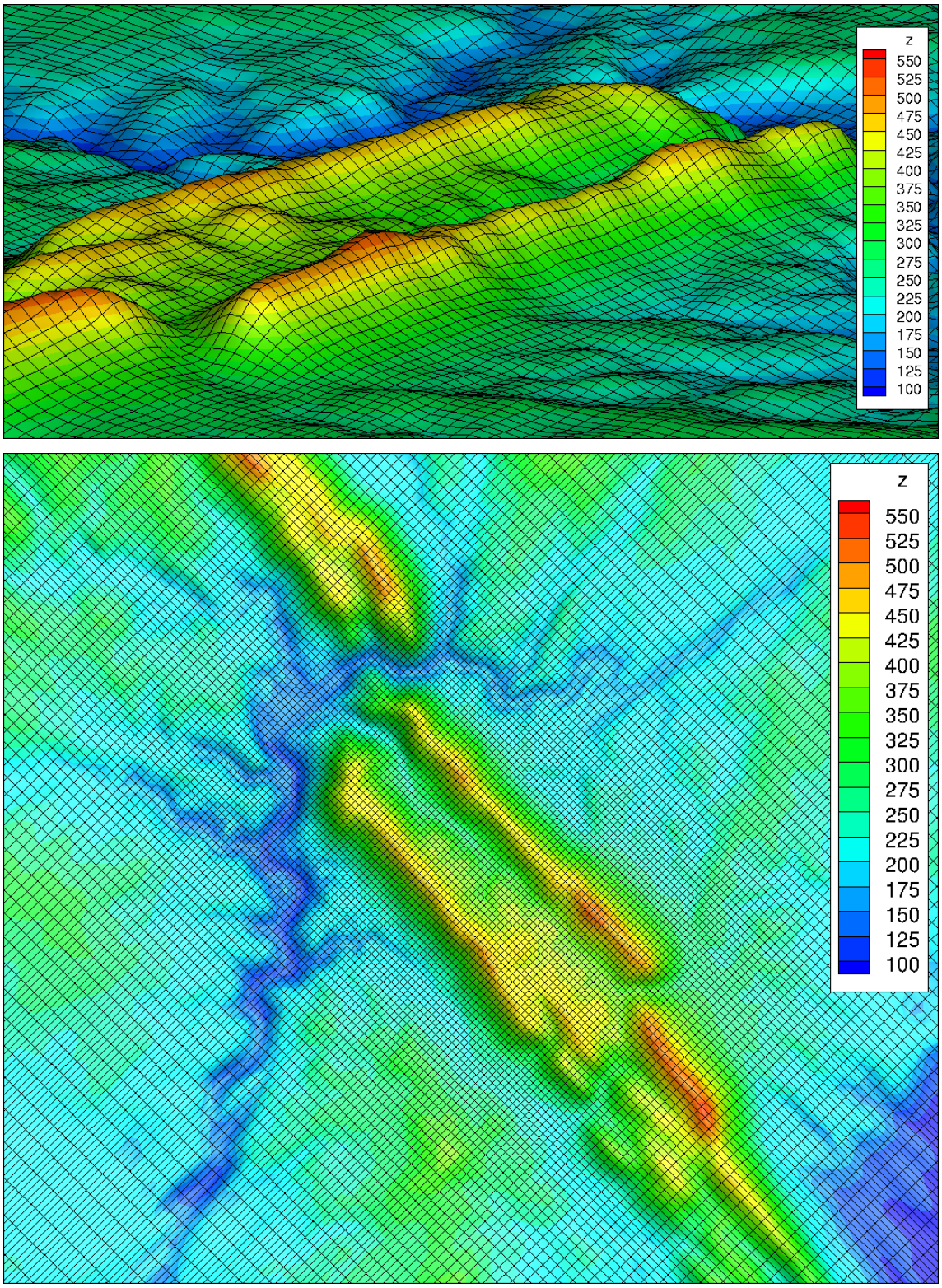

Figure 4.12: A closer look to the structured terrain-following 80×80 m horizontal resolution mesh (z coordinate scaled by a factor of 2).

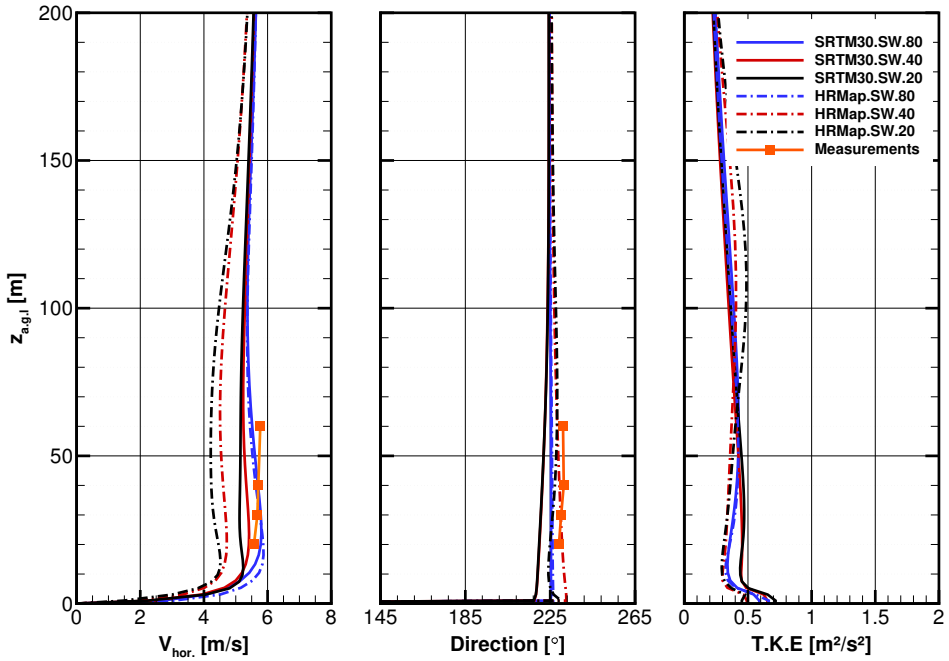

Figure 4.13: Wind speed, direction and turbulent kinetic energy profile simulation results in Tower 37 for SW winds.

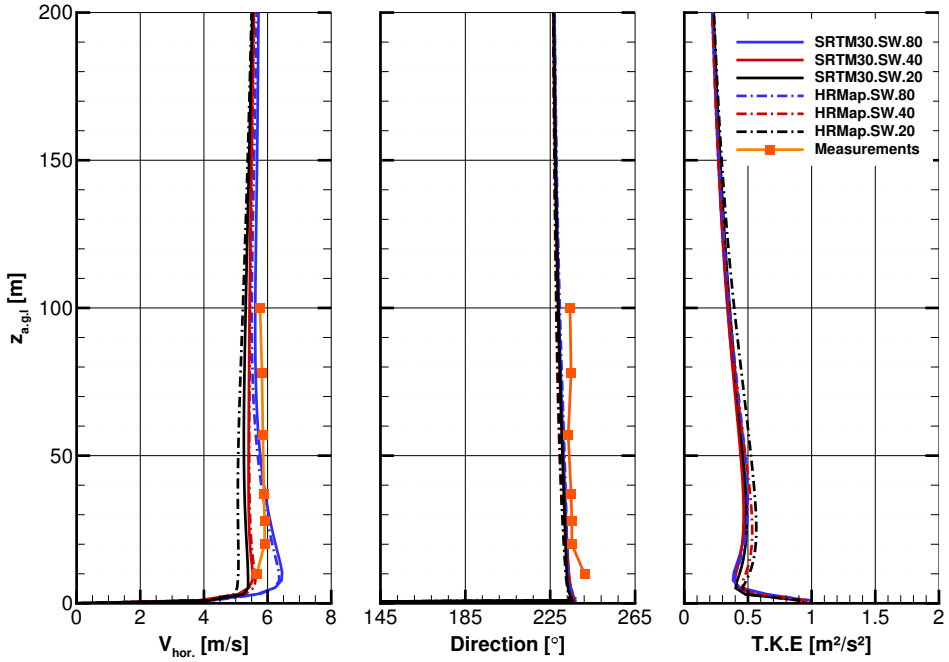

Figure 4.14: Wind speed, direction and turbulent kinetic energy profile simulation results in Tower 20 for SW winds.

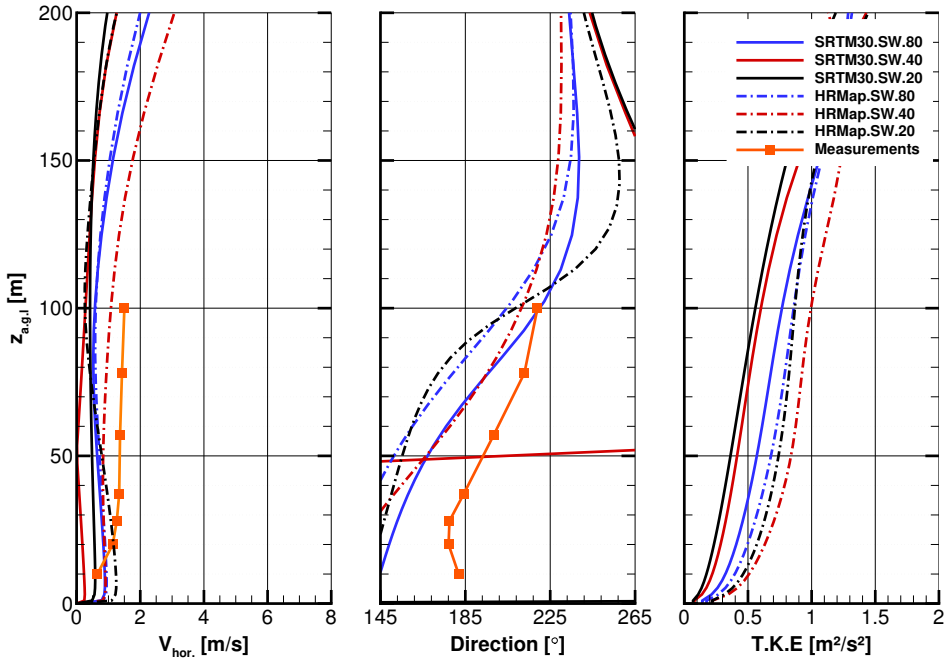

Figure 4.15: Wind speed, direction and turbulent kinetic energy profile simulation results in Tower 25 for SW winds.

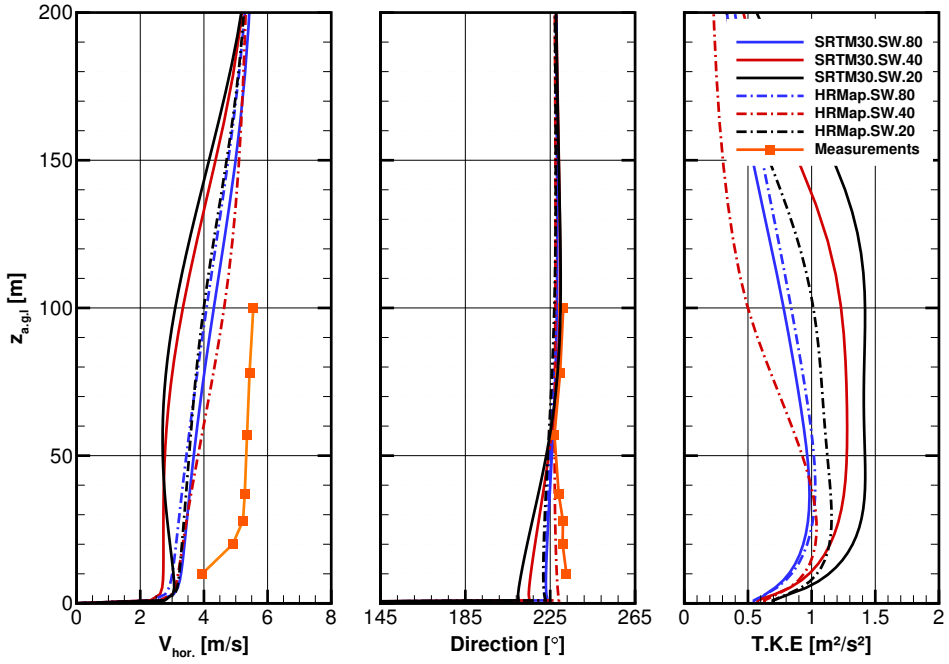

Figure 4.16: Wind speed, direction and turbulent kinetic energy profile simulation results in Tower 29 for SW winds.

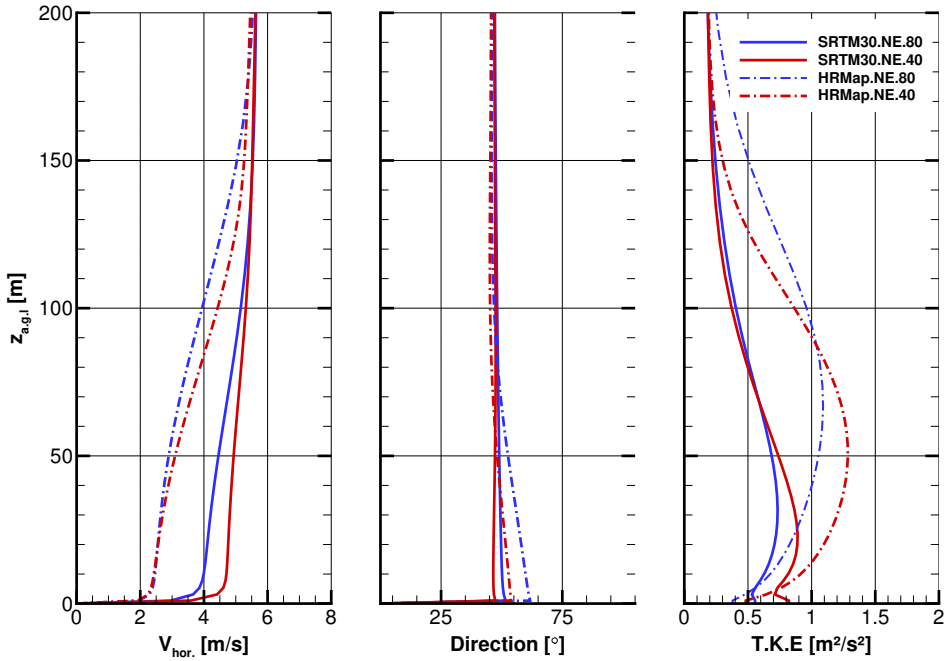

Figure 4.17: Wind speed, direction and turbulent kinetic energy profile simulation results in Tower 37 for NE winds.

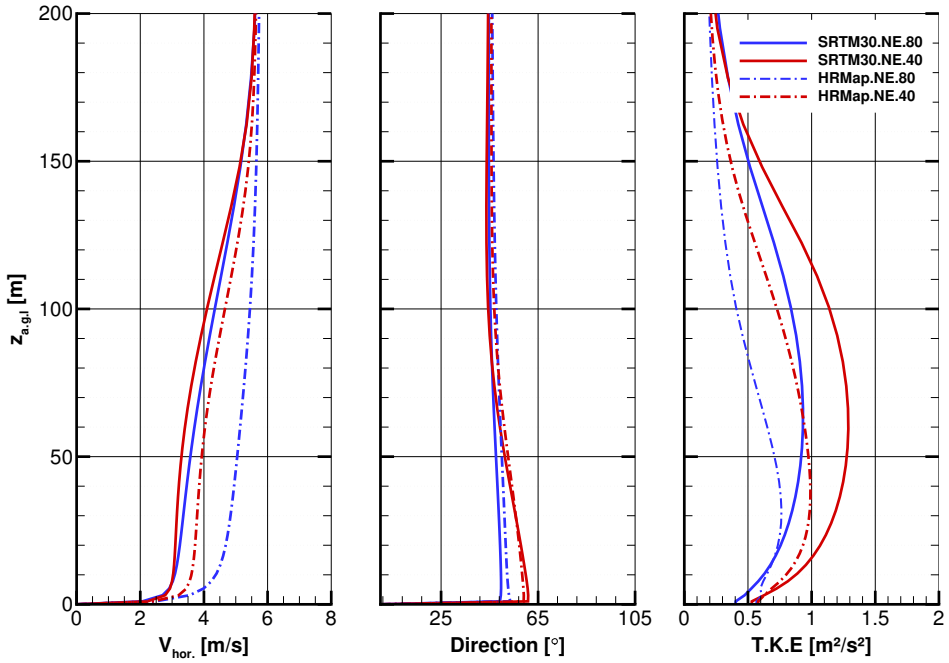

Figure 4.18: Wind speed, direction and turbulent kinetic energy profile simulation results in Tower 20 for NE winds.

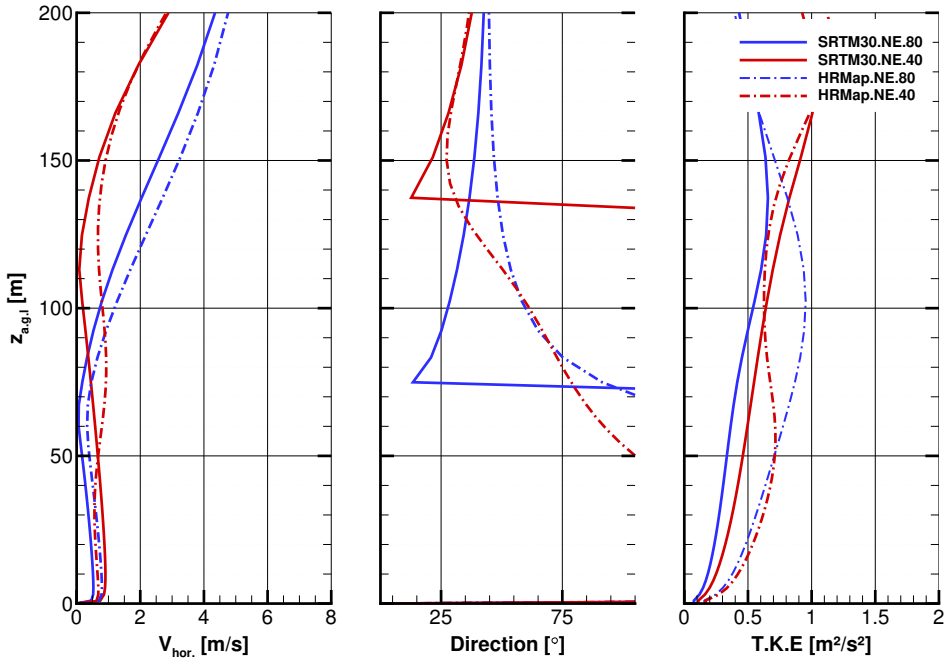

Figure 4.19: Wind speed, direction and turbulent kinetic energy profile simulation results in Tower 25 for NE winds.

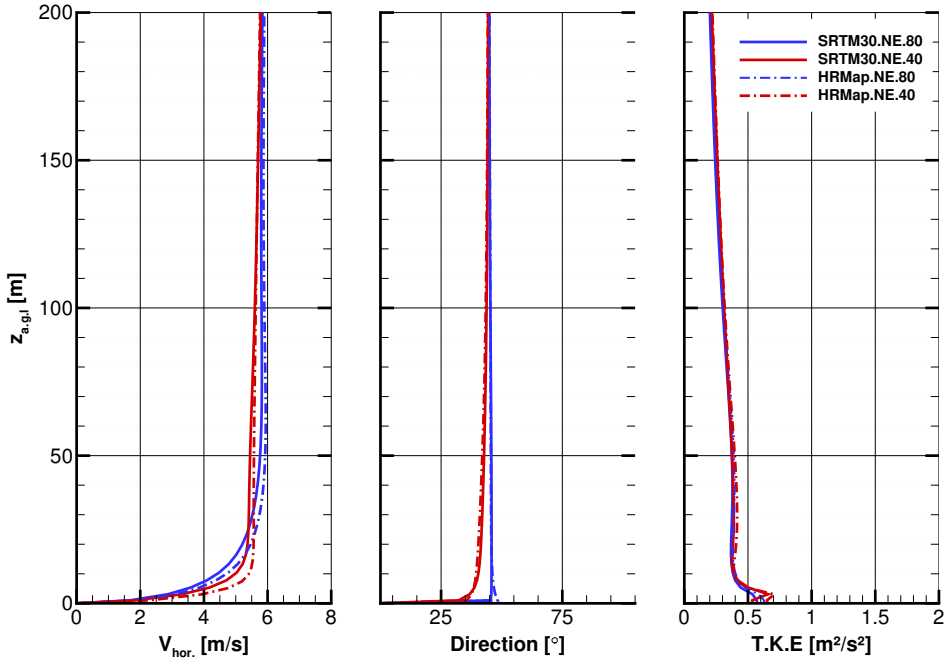

Figure 4.20: Wind speed, direction and turbulent kinetic energy profile simulation results in Tower 29 for NE winds.

4.5 Land cover

This section aims to quantify the impact of modelling the surface cover, by considering a variable roughness and introducing a canopy model in the computational model and also to compare the different representations of that roughness, as described in Chapter 3. Table 4.5 shows the different cases, the numerical parameters and the duration of each simulation.

To obtain a coherent comparison with the previous results from section 4.4, the value of the friction velocity u^* was calibrated (in both wind directions) to obtain approximately the same horizontal velocity on Tower 20 at 100 m a.g.l, chosen to be the reference point in the domain. The value was increased from 0.23 to 0.3 for SW winds and from 0.23 to 0.32 for NE winds to achieve the needed results.

Southwesterly winds

For SW winds, horizontal velocity, turbulent kinetic energy and wind direction profiles in the first 200 m a.g.l. are discussed with surface cover models.

For towers located in the southern ridge, such as Tower 37 (Figure 4.21) or 20 (Figure 4.22), the presence of the surface cover model (and with higher values, as HRMap.SW.80 and similar cases with different resolutions considered constant roughness of 0.03 m) shows an increase in turbulent kinetic energy and a decrease of horizontal velocity. Changes in horizontal velocity are most noticeable between different mesh resolutions. For turbulent kinetic energy, profiles are mostly grouped by the presence or absence of the surface cover model with small differences between mesh resolutions. The wind turbine location (Figure E.1) shares the same conclusions as the southern ridge towers.

The low wind speeds inside the valley (Tower 25, Figure 4.23) are not significantly affected by the change in surface cover, irrespective of horizontal resolution. Due to the flow speeds, the variations in direction in the first 200 m, although considerable, should not be over-valued.

Wind speed at Tower 29 decreased considerably (over 1 m s^{-1}) with the addition

	$\Delta_{x/y}$ [m]			Δ_z [m]			
Name	Min	Max	$n_i \times n_j$	Min	Max	n_k	t_{CPU} [h]
CLC.SW.80	80	458.9	120×155	2	223.6	60	5.11
CLC.SW.40	40	378.3	200×270	2	226.2	60	11.89
RougCan.SW.80	80	458.9	120×155	2	223.6	60	0.81
RougCan.SW.40	40	378.3	200×270	2	226.2	60	5.62
RougCan.SW.20	20	396.2	320×470	2	118.2	55	25.04
CLC.NE.80	80	458.9	120×155	2	223.6	60	2.73
CLC.NE.40	40	378.3	200×270	2	226.2	60	17.32
RougCan.NE.80	80	458.9	120×155	2	223.6	60	0.94
RougCan.NE.40	40	378.3	200×270	2	226.2	60	6.68

Table 4.5: Mesh parameters details used on the simulation with roughness.

of the surface cover model, with resolutions of 40×40 m and 20×20 m and turbulent kinetic energy also steadily increases with resolution. A similar behaviour is not seen without the surface cover data. Turbulent kinetic energy more than doubles its value at 100 m a.g.l. (Figure 4.24) with a 40×40 m resolution when considering the surface cover model.

The pattern discussed in section 4.4 of decreasing horizontal velocities with mesh refinement still stands. Wind direction was, once again, the least sensible variable with the exception of Tower 25 in the valley where sudden changes in direction were expected (and as experimental data supports).

The comparison between the different surface cover models considered (CLC and RougCan cases, Table 4.5) is documented in Appendix E, from Figure E.3 to E.7. Using only Corine Land Cover as source for the land cover model led to higher horizontal velocities in all five key-points. Decreasing horizontal velocities with mesh refinement shows similar behaviour between land cover models. Tower 29 (Figure E.6) shows to be the most affected by the different representations, showing differences in horizontal velocity of almost $1 ms^{-1}$ for 80×80 m resolution.

Northeasterly winds

Results for NE winds show the same general trend as SW winds, as the presence of the surface cover model shows a decrease of horizontal velocity and increase of turbulent kinetic energy for the towers upstream (in this case, Tower 29).

The impact of the mesh resolution proved to be always dominant throughout the four towers, and not the presence or absence of the surface cover model. Even for the towers affected by the flow in the valley (Tower 20, 25 and 37) differences in horizontal velocity when considering the surface cover model do not go over 0.5 $m\ s^{-1}$.

The comparison between the different surface cover models considered for NE winds (Appendix E, from Figure E.8 to E.12) show that using only Corine Land Cover in the land cover model proved to have little effect in all five key-points when compared to the other representation, and mesh resolution was the dominant factor.

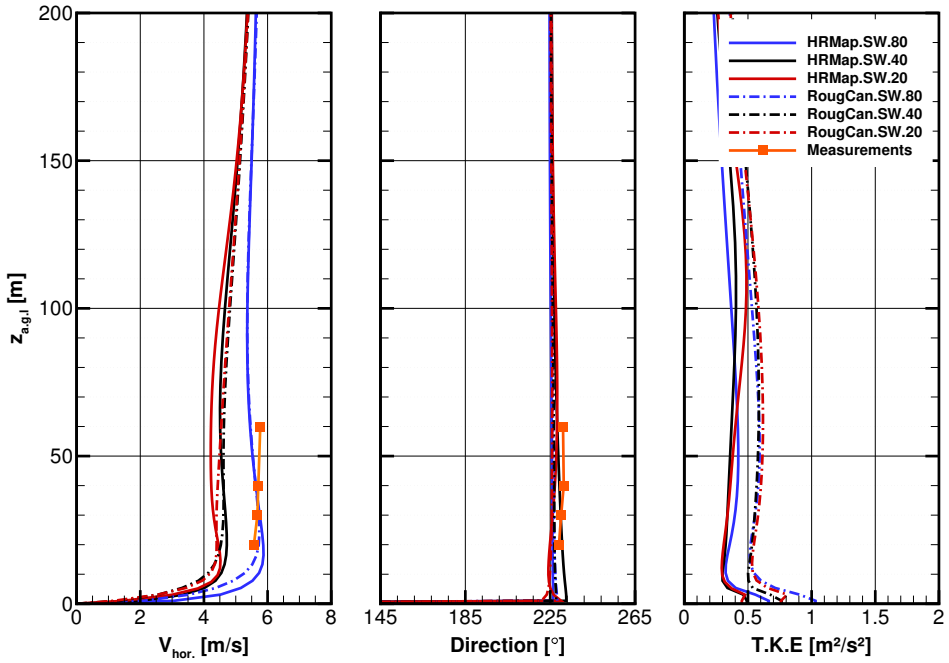

Figure 4.21: Numerical results for the surface cover model for SW winds, Tower 37.

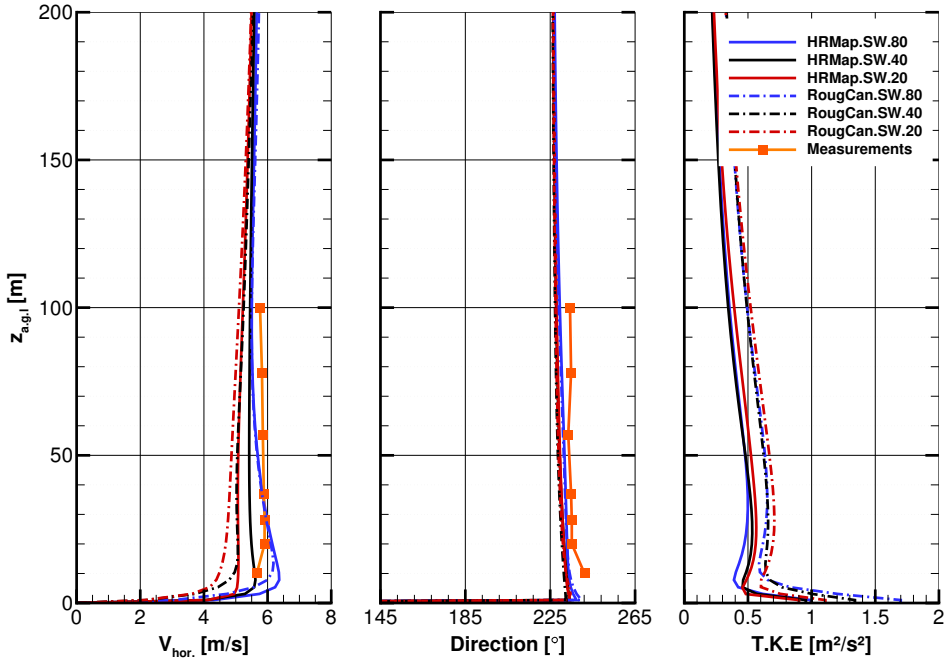

Figure 4.22: Numerical results for the surface cover model for SW winds, Tower 20.

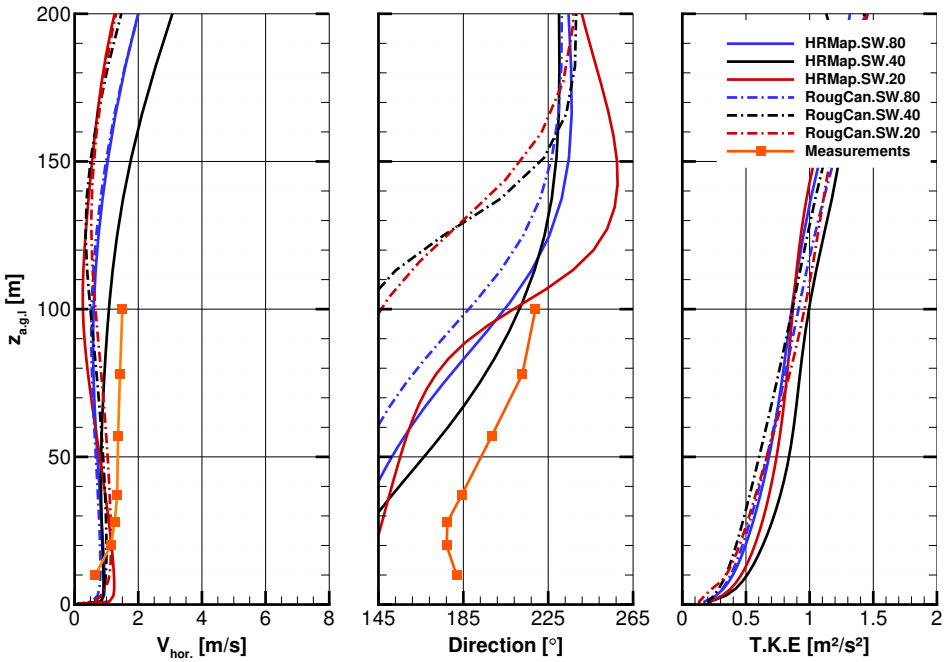

Figure 4.23: Numerical results for the surface cover model for SW winds, Tower 25.

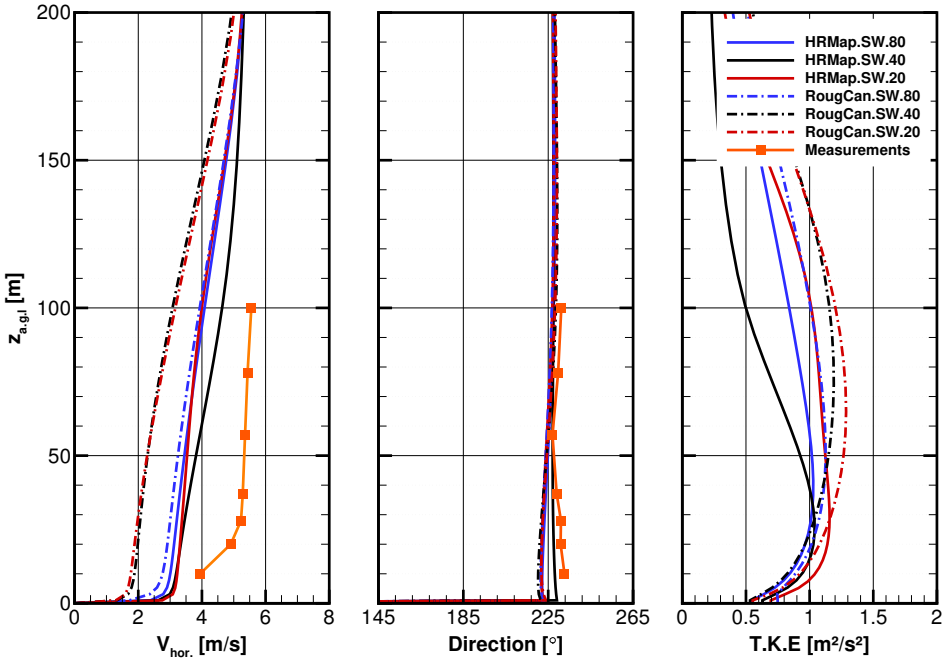

Figure 4.24: Numerical results for the surface cover model for SW winds, Tower 29.

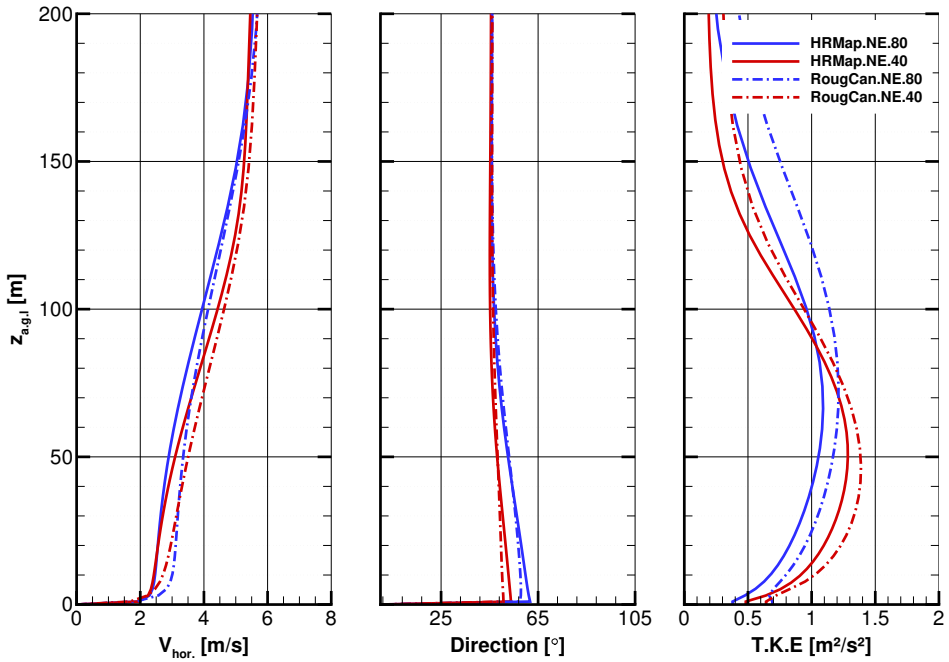

Figure 4.25: Numerical results for the surface cover model for NE winds, Tower 37.

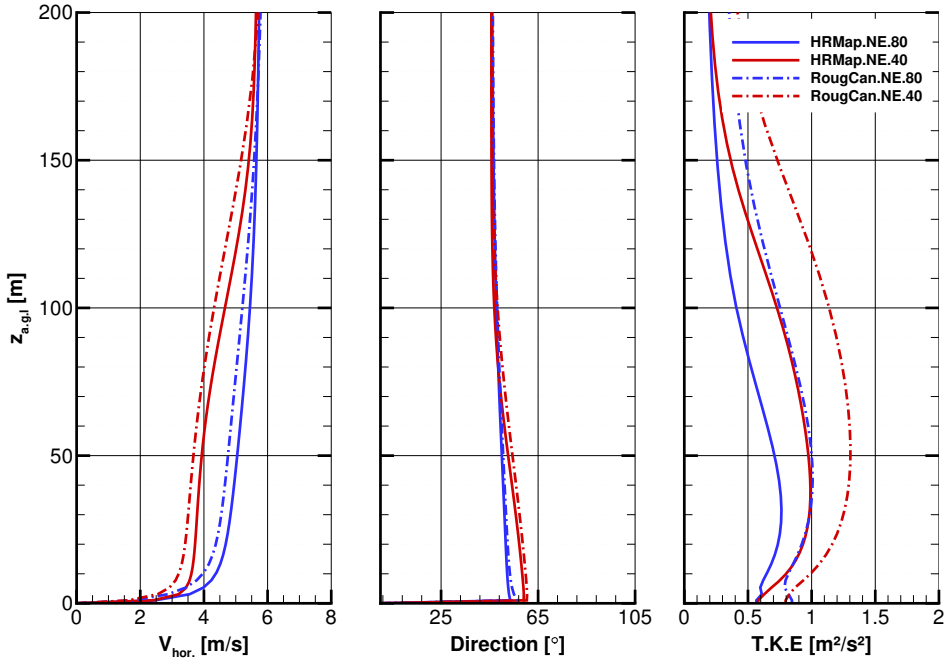

Figure 4.26: Numerical results for the surface cover model for NE winds, Tower 20.

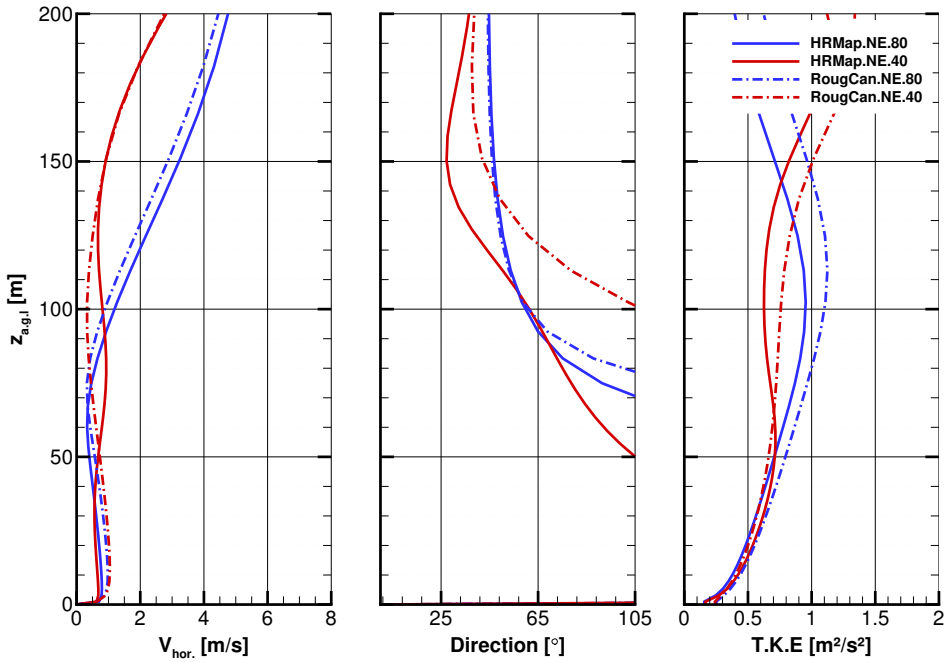

Figure 4.27: Numerical results for the surface cover model for NE winds, Tower 25.

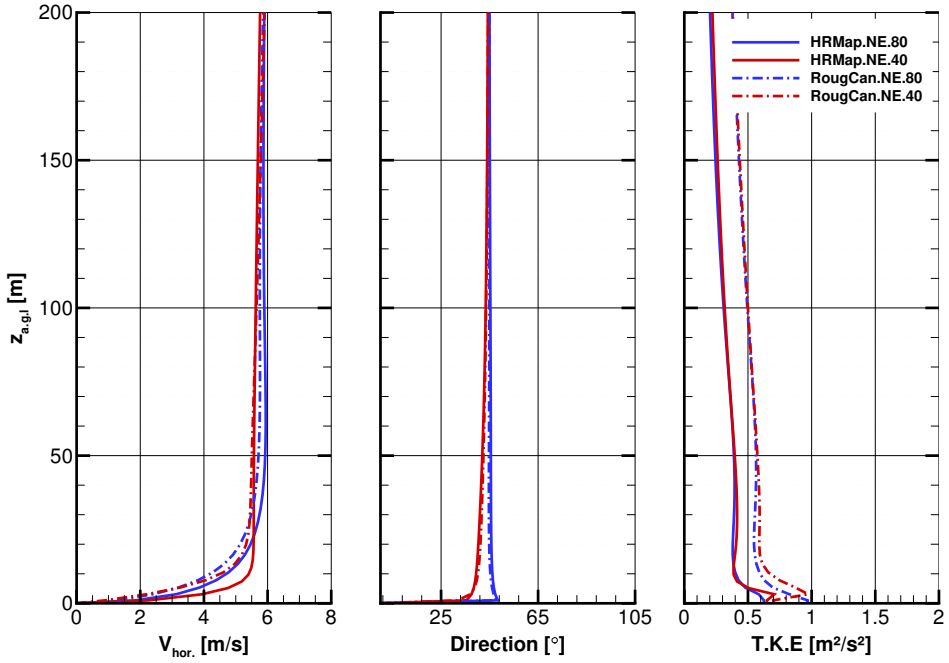

Figure 4.28: Numerical results for the surface cover model for NE winds, Tower 29.

4.6 Wind turbine

As mentioned in Chapter 1.2, the Perdigão site has the characteristic of having a single wind turbine (Enercon 2MW; 82 m diameter) on the southern ridge with 80 m hub height. Using different simulation results (with and without the surface cover model) some preliminary results can be obtained specifically for the wind turbine location. For wind turbines there are some main variables that can affect its operation, such as the shear factor between the top and bottom of the rotor swept area, wind flow inclination and turbulence intensity. These are indicators that are linked to the wind turbine class chosen to put on site. The results for SW and NE winds are displayed in Figures 4.29 and 4.30.

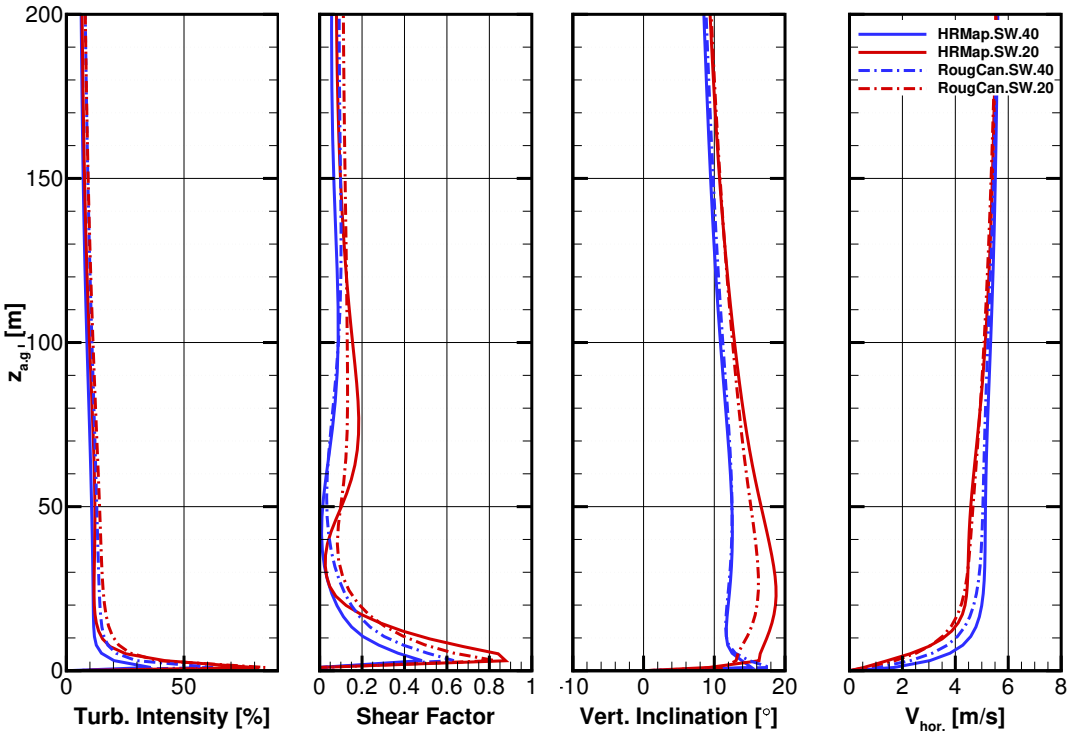

Figure 4.29: Numerical results for the wind turbine, SW winds.

For the turbulence intensity, SW winds show relatively homogeneous values (around 10%) inside the rotor span (40 to 120 m), while for NE winds they are approximately double that value (around 20%). There is not much dependency on the mesh resolution and surface cover representation.

Local shear factor seems to be more affected by the change of mesh resolution. At the wind turbine hub height, for SW winds the value ranges range from 0.06 to 0.18, while for NE winds the values are much higher (0.28 to 0.44). Considering shear factor only between the top and bottom of the rotor swept area, SW winds shows a 0.06 value while NE winds reveal 0.44, well above a reference value of 0.2 generally considered to be acceptable in the wind energy industry.

Vertical inclination of the flow has high values (between 11 and 14° at hub height)

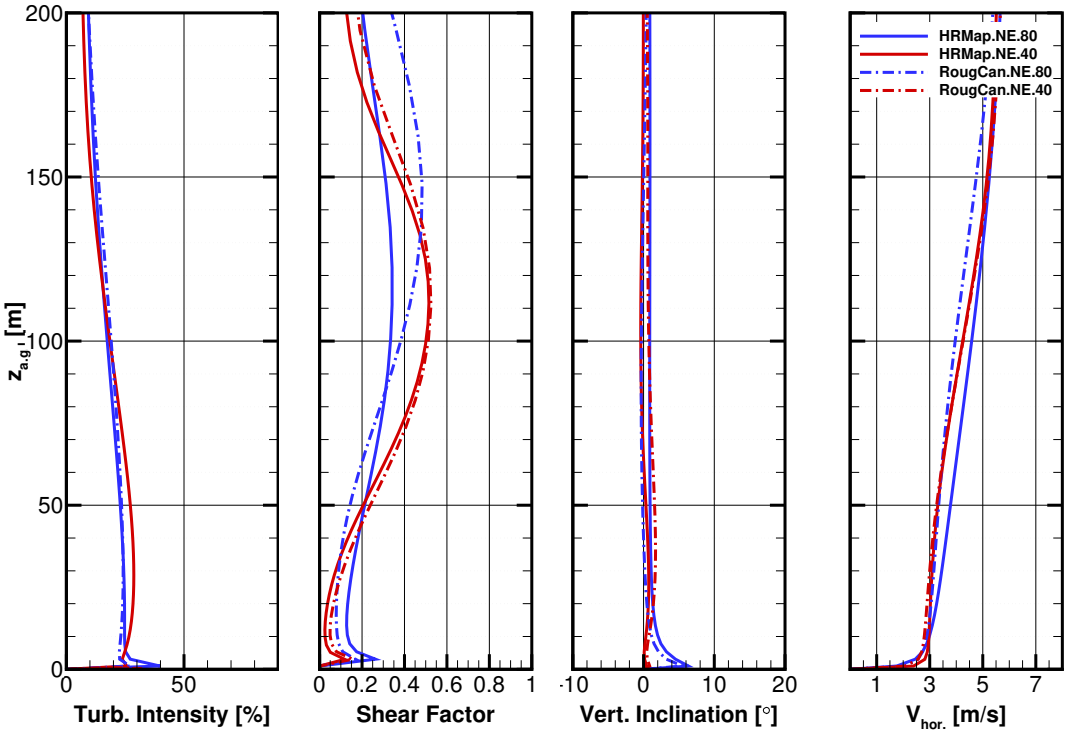

Figure 4.30: Numerical results for the wind turbine, NE winds.

for SW winds (typical reference limit value for vertical inclination is 8°) and its profile is very affected by the horizontal mesh resolution. For NE winds the values are close to zero and show low sensitivity between the considered cases. Figures D.5c and 4.9c for Tower 37, close to the wind turbine, support the fact for SW winds there is a clear sign of vertical inclination of the flow at hub height (probably due to the steep slope when approaching the peak of the southern ridge), while for NE winds vertical inclination is not visible in the southern ridge.

Horizontal velocity reaches around 5.5 ms^{-1} at hub height for SW winds, while for NE winds values only reach around 4 ms^{-1}. The fact that the wind turbine is positioned in the southern ridge has the consequence of making the predominant wind direction a critical factor when assessing the previous variables in this location, as the complexity of the flow in the valley significantly affects the quantity and quality of wind resource at hub height.

4.7 Conclusions

This subsection summarizes the main conclusions about the computational parameters such as the domain and mesh resolution, and its influence on the simulation results and specific physical variables, globally and in specific key points. The main conclusions were:

Domain boundaries

- The domain boundary positioning has a small but noticeable impact on the results, although it is important to note that it is much lower than all other parameters. The study for positioning the boundaries focused on SW winds and the inlet boundary's influence proved to dominate when compared to the remaining boundaries.
- The top and bottom boundary positions were important to calibrate, since they were associated with potential numerical convergence problems, due to the introduction of complex flow structures.
- The horizontal velocity seemed to be more affected than the turbulent kinetic energy, with a maximum range of around 0.5 m/s between different distances from the domain center.

Flow patterns

Southwesterly winds

- The flow in the central area of the southern ridge goes mainly over the valley, leaving a lower pressure area in the valley (relative to the ends of the ridges) filled from both sides of the southern ridge and going predominantly parallel to the ridges. These two streams meet in the middle and the flow exits mainly over the centre of the northern ridge.
- The cross-stream velocity component shows that mid-valley the mean flow inverts its direction from going down to going up the valley.
- Detachment occurs at the ridge's peak and shows different behaviours along different transects. Reattachment occurs mainly mid-valley when approximating the northern ridge. For Tower 37, with the presence of the surface cover model, reattachment does not occur even when passing the northern ridge.

Northeasterly winds

- Part of the flow goes above the double ridge, over the valley. The flow that fills the low pressure valley area (relative to the ends of the ridges) comes mostly from the gap on the south, corroborated by the cross-stream velocity component, dominantly positive.
- A part of the flow that comes from the south gap also escapes instead of going down the valley. The two gaps on the double ridge's ends accelerate the flow and form jet-like streams.
- Flow detachment occurs right after reaching the peak of the northern ridge, and reattachment occurs mainly when reaching the southern ridge. The whole valley between the two ridge's peaks shows detached flow for Tower 39.

DTM and mesh resolution influence on simulation results

Southwesterly winds

- Tower 20 at 50 m a.g.l. shows that differences between DTMs at the same resolution in horizontal velocity are all under 0.25 $m\ s^{-1}$, while differences greater than 0.5 $m\ s^{-1}$ can be reached between mesh refinements, particularly 80×80 m to 40×40 m. At 80×80 m horizontal velocity profiles show negative shear, absent from experimental results.

- Tower 37 shows higher differences (at the same height) in horizontal velocity when using different DTMs with finer meshes. For example, while the coarser 80×80 m shows almost null differences between SRTM 30 m and HRMap, 20×20 m shows circa 1 $m\ s^{-1}$ or more difference. The turbulent kinetic energy profiles also present similar sensitivity to resolution, responding differently to mesh refinement for the two DTMs.

- In both towers, using the improved DTM and finer meshes cause lowered wind speeds and degraded match to experimental data, particularly at Tower 37.

- As Tower 37 and 20 are located on the southern ridge before the complexity of the valley flow, wind direction was thought to not vary much from the inflow. The wind direction profile in both towers supports the previous statement showing negligible variations in the first 200 m, deviating a maximum of 12° for Tower 20 and 8° for Tower 37 and matching the experimental data. Impact of DTM and mesh resolution for both towers only shows on the first 150 m above ground level.

- Tower 25 shows much greater impact from changes in DTM and mesh resolution, with very low horizontal velocities (generally under 1 $m\ s^{-1}$ and typical of recirculation zones). All profiles agree on these values (corroborated by experimental data), diverging only above 100 m. These low horizontal velocities are also associated with big variations of wind direction that stabilize on the SW sector (circa 225°) only above 200 m above ground level.

- Tower 29 located in the northern ridge, past the valley) shows big variations of turbulent kinetic energy (different cases differ a maximum of 1 $m^2\ s^{-2}$). Its wind profile (in opposite to the southern ridge towers) shows higher values when using HRMap as DTM, while when using SRTM 30 m negative shears appear and differences only became negligible above circa 170 m above ground level.

- In general, wind flow direction was the least sensible variable, almost indifferent to the DTM or mesh resolution (with the exception of Tower 25).

- The impact of the DTM used was greater for higher mesh resolutions. However, in locations affected by the valley's flow complexity (Tower 25 and Tower 29), the response to mesh refinements for different DTM was different, diverging with SRTM whereas HRMap remains more stable.

- Mesh refinement from 80×80 m to 40×40 m generally led to an increase of the extent of the recirculation zone, and to the separation point occurring earlier along

transects that cross double ridge. 20×20 m resolution was not consistent with this trend (the higher number of vertical nodes could affect the direct comparison between resolutions).

Northeasterly winds

- Tower 29, located in the northern ridge and thus on the upstream side of the valley) was the least affected by the change in DTM with converged results beyond 50 m above ground level. It showed only small differences, caused by refining the mesh from 80×80 m to 40×40 m.
- For the southern ridge locations, in this case more affected by the valley's flow complexity, Towers 37 and 20 showed that the DTM change has a noticeable impact on horizontal velocity (differences as high as 2 m s^{-1} or 40% reduction when using HRMap instead of SRTM 30 m at 50 m a.g.l.) and turbulent kinetic energy (differences of 0.5 m^2 s^{-2} or 70% increase when using HRMap at 50 m a.g.l.).
- Flow behaviour regarding Tower 25 is very similar to SW winds, with very low horizontal velocities in the first 100 m (generally under 1 m s^{-1}) and big variations of wind direction that stabilize on the NE sector (circa 45^o) only above 200 m above ground level. Again the DTM is the dominant factor for change in profile shape.
- Flow direction was (as equally concluded for SW winds) the least sensible variable to the change in DTM and mesh resolution (with the exception of Tower 25).

Surface cover model influence on simulation results

Southwesterly winds

- For towers located in the southern ridge, such as Tower 37 or 20, the presence of the surface cover model (and with higher values, as HRMap.SW.80 and similar cases with different resolutions considered constant roughness of 0.03 m) shows an increase in turbulent kinetic energy and a decrease of horizontal velocity. Changes in horizontal velocity are most noticeable between different mesh resolutions. For turbulent kinetic energy, profiles are mostly grouped by the presence or absence of the surface cover model with small differences between mesh resolutions.
- The low wind speeds inside the valley (Tower 25) are not significantly affected by the change in surface cover, irrespective of the horizontal resolution. Due to the flow speeds, the variations in direction in the first 200 m, although considerable, should not be over-valued.
- Wind speed at Tower 29 decreased considerably (over 1 m s^{-1}) with the addition of the surface cover model, with resolutions of 40×40 m and 20×20 m and turbulent kinetic energy also steadily increases with resolution. A similar behaviour is not seen without the surface cover data. Turbulent kinetic energy more than doubles its value at 100 m a.g.l. with a 40×40 m resolution when considering the surface cover model.

- The pattern discussed when comparing only DTM and mesh resolutions, of decreasing horizontal velocities with mesh refinement, still stands. Wind direction was, once again, the least sensible variable with the exception of Tower 25 in the valley where sudden changes in direction were expected (and as experimental data supports).

- Using only Corine Land Cover as source for the land cover model led to higher horizontal velocities in all five key-points. Decreasing horizontal velocities with mesh refinement shows similar behaviour between land cover models. Tower 29 shows to be the most affected by the different representations, showing differences in horizontal velocity of almost 1 $m\ s^{-1}$ for 80×80 m resolution.

Northeasterly winds

- Results for NE winds show the same general trend as SW winds, as the presence of the surface cover model shows a decrease of horizontal velocity and increase of turbulent kinetic energy for the towers upstream (in this case, Tower 29).

- The impact of the mesh resolution proved to be always dominant throughout the four towers, and not the presence or absence of the surface cover model. Even for the towers affected by the flow in the valley (Tower 20, 25 and 37) differences in horizontal velocity when considering the surface cover model do not go over 0.5 $m\ s^{-1}$.

- The comparison between the different surface cover models show that using only Corine Land Cover in the land cover model proved to have little effect in all five key-points when compared to the other representation, and mesh resolution was the dominant factor.

Wind Turbine

- Turbulence intensity for SW winds shows homogeneous values inside the rotor span, while for NE winds they are approximately double that value.

- Between the top and bottom of the rotor swept area, shear factor for SW winds shows a 0.06 value while NE winds reveal 0.44, well above a reference value of 0.2.

- Vertical inclination of the flow (typical reference limit value of 8^o) has values between 11° and 14° at hub height for SW winds, while for NE winds values are close to zero.

- Horizontal velocity reaches around 5.5 $m\ s^{-1}$ at hub height for SW winds, while for NE winds values only reach around 4 $m\ s^{-1}$.

- The fact that the wind turbine is positioned in the southern ridge has the consequence of making the predominant wind direction a critical factor when assessing the previous variables in this location, as the complexity of the flow in the valley significantly affects the quantity and quality of wind resource at hub height.

Computational effort and convergence problems

- Computational time increases with resolution, so a compromise between computational effort and accuracy is necessary.
- Difficulties in numerical convergence increased for higher resolution meshes.
- The use of a variable roughness surprisingly led to easier convergence and less time-consuming simulations, possibly associated to lower near-surface wind speeds.
- In terms of predominant wind directions studied, SW winds proved to be of easier convergence.

Chapter 5

Conclusions and future work

5.1 Conclusions

5.1.1 Terrain and land cover model

The high-resolution digital terrain model (DTM) produced for the Perdigão site (HRMap) based on LiDAR technology was compared with a version of the Shuttle Radar Topography Mission (SRTM), a public domain DTM, with different mesh resolutions (80×80, 40×40, 20×20 m and 10×10 m). A basic statistical analysis was performed to assess the impact of the DTM source and the resolution in the terrain description. Land cover information was also obtained from the LiDAR data and through Corine Land Cover (CLC), to produce a surface cover model. The main conclusions were the following:

1. The SRTM did not accurately represent the terrain and did not bring any advantages when using higher resolution meshes, as it is limited to the 30 m resolution of its source. The HRMap should be used in future works.
2. The spectral analysis shows that only meshes based on the HRMap have the ability to reproduce the high-frequency range ($7 \times 10^{-2}\ rad/m < k < 1\ rad/m$), while SRTM30 m shows faster decay at high frequencies, as it extrapolates beyond the resolution of its source.
3. The HRMap is a source with lower elevation errors all around the domain, showing an average root mean square error (RMSE) around 5 m for 80×80 m, decreasing to 0.5 m with 10×10 m. The RMSE for SRTM 30 m does not go under 4 m. A 40×40 m horizontal resolution based on the HRMap is enough to achieve an error below 1 m in five key locations and below 0.5 m using 20×20 m.
4. The slope in the x direction showed maximum slopes about 2× higher (140.70%) on a 20×20 m mesh resolution compared with an 80×80 m mesh resolution (78.04%). Terrain profiles passing through each 100 m tower show that 80×80 m mesh resolution does not accurately represent elevation and slope, mainly near the extreme elevation values (highs and lows). The ruggedness index (RIX) has an average value of 11.06% for SRTM 30 m and 15.22% for LiDAR. SRTM 30 m under-predicts RIX for the five key points in circa 30%.

5. Vegetation and canopy were modelled by an increased roughness length up to 5 m vegetation height and by a canopy model for vegetation above that height. Four canopy zones with different heights were defined, leading to sparse canopy areas.

5.1.2 Flow model

Numerical meshes were generated with 80×80, 40×40 and 20×20 m based on the SRTM 30 m and HRMap. The impact of the domain boundary positions, DTM, mesh resolution and surface cover model was evaluated in the horizontal velocity, direction and turbulent kinetic energy of the flow, globally and in five key points (Tower 20, Tower 25, Tower 29, Tower 37 and wind turbine). This analysis was done to both SW and NE winds. General flow patterns were described. The main conclusions were the following:

1. The domain boundary positioning has a small but noticeable impact on the results. The inlet boundary's influence proved to dominate when compared to the remaining boundaries. Horizontal velocity was more affected than the turbulent kinetic energy.

2. Computational time increased with resolution, so a compromise between computational effort and accuracy is necessary.

Southwesterly winds:

1. General flow patterns show the flow in the central area of the southern ridge goes mainly over the valley, leaving a lower pressure area in the valley (relative to the ends of the ridges) filled from both sides of the southern ridge and going predominantly parallel to the ridges. These two streams meet in the middle and the flow exits mainly over the centre of the northern ridge. The cross-stream velocity component shows that mid-valley the mean flow inverts its direction from going down to going up the valley.

2. The impact of DTM and mesh resolution for the southern ridge towers is only apparent on the first 150 m above ground level. As they are located before the complexity of the valley flow, wind direction did not vary much from the inflow. Using the HRMap and finer meshes caused lowered wind speeds in the first 150 m and degraded match to experimental data, particularly at Tower 37. This could be explained by the fact that mesh refinement showed a more detailed representation of the terrain. Thus, more height variations are resolved and drag is increased.

3. Tower 25, located in the valley, shows great impact from DTM and resolution change (mainly in the wind direction), with low horizontal velocities (under $1 ms^{-1}$, typical of recirculation zones) corroborated by experimental data. These low velocities are associated with large variations of wind direction with height that only stabilized above 200 m above ground level. Wind velocity profiles in Tower 29 shows higher values when using HRMap as DTM (in opposite to the southern ridge towers), while negative shears appear when using SRTM 30 m.

4. The impact of the DTM was greater for higher mesh resolutions in all four towers. In locations affected by the valley's flow complexity (Tower 25 and Tower 29), the response to mesh refinements for different DTM was different, diverging with SRTM whereas HRMap remains more stable.

5. The addition of the surface cover model led to an increase of the surface friction and, consequently, to a general decrease of horizontal velocity and increase of turbulent kinetic energy for towers located in the southern ridge (Tower 20 and 37), which experienced noticeable changes in horizontal velocity due to mesh refinement, while turbulent kinetic energy profiles were mostly grouped by the presence or absence of the surface cover model. Wind speed at Tower 29 decreased over 1 ms^{-1} with the addition of the surface cover model (for resolutions of 40×40 m and 20×20 m). Turbulent kinetic energy steadily increased with resolution.

6. When assessing the impact of the presence or absence of the surface cover model, the impact of resolution dominates at the southern ridge, but not in the remaining locations, where the surface cover model influences the most.

7. Wind direction was the least sensible variable, with and without the presence of a surface cover model, showing only considerable variations for Tower 25, where the flow was expected to significantly change its direction with height.

8. Mesh refinement from 80×80 m to 40×40 m generally led to an increase of the extent of the recirculation zone, and to the separation point occurring earlier along transects that cross the double ridge. This could be explained by the fact that, when refining the mesh, slopes showed to be steeper when approaching the summit of the southern ridge. 20×20 m resolution was not consistent with this trend (the higher number of vertical nodes could affect the direct comparison between resolutions).

Northeasterly winds:

1. General flow patterns show that part of the flow goes above the double ridge, over the valley. The flow that fills the low pressure valley area (relative to the ends of the ridges) comes mostly from the gap on the south, corroborated by the cross-stream velocity component, dominantly positive. A part of the flow that comes from the south gap also escapes instead of going down the valley. The two gaps on the double ridge's ends accelerate the flow and form jet-like streams.

2. Southern ridge towers showed to be more affected by the change in DTM, instead of mesh resolution. Tower 37 showed differences as high as 2 m s^{-1} (circa 40% reduction) in horizontal velocity and 0.5 m^2 s^{-2} (circa 70% increase) in turbulent kinetic energy when using HRMap instead of SRTM 30 m.

3. When assessing the impact of the surface cover model, the mesh resolution was always the dominant parameter for this wind direction, in all five key points.

4. Wind direction was the least sensible variable, with and without the presence of a surface cover model, showing only considerable variations for Tower 25, just as concluded for SW winds.

Wind turbine:

1. The location of the wind turbine, in the southern ridge, has the consequence of making the predominant wind direction a critical factor when assessing the quantity and quality of wind resource at hub height, as the flow in the valley shows to be complex and to affect parameters linked to the wind turbine's operating conditions.

2. Turbulence intensity for SW winds shows relatively homogeneous values (around 10%) inside the rotor span, while for NE winds they are approximately twice that value. Between the top and bottom of the rotor swept area, shear factor for SW winds shows a 0.06 value while NE winds reveal 0.44, well above a reference value of 0.2. Vertical inclination of the flow (typical reference limit value of 8°) has values between 11° and 14° at hub height for SW winds, while for NE winds values are close to zero. Horizontal velocity reaches around 5.5 m s^{-1} at hub height for SW winds, while for NE winds values only reach around 4 m s^{-1}.

5.2 Future work

- A thorough study on registering experimental stationary periods of time with a set of different criteria would allow to extract more information from the comparison of numerical results with the experimental data from the Perdigão campaign.

- Experimental data for pressure and turbulent kinetic energy would be relevant to reach a higher level of understanding of the flow in Perdigão.

- The addition of stratification effects to the computational flow model should be implemented, to show its impact on numerical results and bring the model closer to the real site conditions.

- Different land cover models should be implemented and compared, trying different sets of heights and number of canopy zones. The possibility of varying LAD with height could also be an important addition to the model.

Bibliography

S. D. Al Harbi. *Suitability of DEMs derived from SAR interferometry and ASTER stereoscopy for hydrological applications using GIS. A case study of Al-Jafer basin, Jordan*. PhD thesis, University of Leicester, 2009.

C. G. Bachman. Laser radar systems and techniques. 1979.

Andreas Bechmann, Jacob Berg, Michael Courtney, Hans Ejsing Jørgensen, Jakob Mann, and Niels N. Sørensen. The bolund experiment: Overview and background. 2009. ISSN 01062840.

F. Bingöl. Complex terrain and wind lidars. *Risø National Laboratory for Sustainable Energy*, 03 2010.

M. Bossard, J. Feranec, and J. Otahel. Corine land cover technical guide – addendum 2000. Technical report, European Environment Agency, 2000.

M. Caetano and F. Marcelino. Corine land cover de portugal continental 1990-2000-2006-2012. relatório técnico. Technical report, Direção-Geral do Território (DGT), 2000.

F. A. Castro, J. M. L. M. Palma, and A. Silva Lopes. Simulation of the askervein flow. part 1: Reynolds averaged navier–stokes equations (k turbulence model). *Boundary-Layer Meteorology*, 107(3):501–530, Jun 2003. doi: 10.1023/A:1022818327584.

FA. Castro. *Metodos Numéricos para a Simulação de Escoamentos Atmosféricos sobre Topografia Complexa*. PhD thesis, Universidade do Porto, 1997.

J.C. Lopes da Costa, F.A. Castro, J.M.L.M. Palma, and P. Stuart. Computer simulation of atmospheric flows over real forests for wind energy resource evaluation. *Journal of Wind Engineering and Industrial Aerodynamics*, 94(8):603 – 620, 2006. ISSN 0167-6105. doi: https://doi.org/10.1016/j.jweia.2006.02.002.

Y. Deng, J. P. Wilson, and B. O. Bauer. Dem resolution dependencies of terrain attributes across a landscape. *Int. J. Geogr. Inf. Sci.*, 21(2):187–213, January 2007. ISSN 1365-8816. doi: 10.1080/13658810600894364.

Jessica DeWitt, Timothy Warner, and Jamison Conley. Comparison of dems derived from usgs dlg, srtm, a statewide photogrammetry program, aster gdem and lidar: implications for change detection. 52:179–197, 03 2015.

Marc Diebold, Jiannong Fang, Andreas Bechmann, and Marc Parlange. Flow over hills: A large-eddy simulation of the bolund case. 2013.

T. G. Farr, P. A. Rosen, E. Caro, R. Crippen, R. Duren, S. Hensley, M. Kobrick, M. Paller, E. Rodriguez, L. Roth, D. Seal, S. Shaffer, J. Shimada, J. Umland, M. Werner, M. Oskin, D. Burbank, and D. Alsdorf. The shuttle radar topography mission. *Reviews of Geophysics*, 2007.

R. Floors, P. Enevoldsen, N. Davis, J. Arnqvist, and E. Dellwik. From lidar scans to roughness maps for wind resource modelling in forested areas. *Wind Energy Science*, 3(1):353–370, 2018. doi: 10.5194/wes-3-353-2018.

Igor V. Florinsky and Galina A. Kuryakova. Determination of grid size for digital terrain modelling in landscape investigations—exemplified by soil moisture distribution at a micro-scale. *International Journal of Geographical Information Science*, 14(8):815–832, 2000. doi: 10.1080/136588100750022804.

J.R. Garratt. *The Atmospheric Boundary Layer*. Cambridge Atmospheric and Space Science Series. Cambridge University Press, 1992. ISBN 9780521380522.

GisGeography DEM. 5 free global dem data sources – digital elevation models. https://gisgeography.com/free-global-dem-data-sources. Accessed: 2018-06-05.

GisGeography Land Cover. 9 free global land cover / land use data sets. https://gisgeography.com/free-global-land-cover-land-use-data/. Accessed: 2018-06-05.

V. Gomes. The wind flow over serra do perdigão - computational preliminary studies. Technical report, CEsA: Research Centre for Wind Energy and Atmospheric Flows, 2012.

K. Jancewicz and M. Szymanowski. The relevance of surface roughness data qualities in diagnostic modeling of wind velocity in complex terrain: A case study from the Śnieznik massif (sw poland). *Pure and Applied Geophysics*, 2017.

J.C. Kaimal and J.J. Finnigan. *Atmospheric Boundary Layer Flows: Their Structure and Measurement*. Oxford University Press, 1994. ISBN 9780195362770.

Julia Lange, Jakob Mann, Jacob Berg, Dan Parvu, Ryan Kilpatrick, Adrian Costache, Jubayer Chowdhury, Kamran Siddiqui, and Horia Hangan. For wind turbines in complex terrain, the devil is in the detail. *Environmental Research Letters*, 12(9), 2017.

Rubini Mahalingam and Michael J. Olsen. Evaluation of the influence of source and spatial resolution of dems on derivative products used in landslide mapping. *Geomatics, Natural Hazards and Risk*, 7(6):1835–1855, 2016. doi: 10.1080/19475705.2015.1115431.

J. Mann, N. Angelou, J. Arnqvist, D. Callies, E. Cantero, R. Chávez Arroyo, M. Courtney, J. Cuxart, E. Dellwik, J. Gottschall, S. Ivanell, P. Kühn, G. Lea, J. C. Matos, J. M. L. M. Palma, L. Pauscher, A. Peña, J. Sanz Rodrigo, S. Söderberg, N. Vasiljevic, and C. Veiga Rodrigues. Complex terrain experiments in the new european wind atlas. *Philosophical Transactions of the Royal Society of London A: Mathematical, Physical and Engineering Sciences*, 375(2091), 2017. ISSN 1364-503X. doi: 10.1098/rsta.2016.0101. URL http://rsta.royalsocietypublishing.org/content/375/2091/20160101.

Niels Mortensen, L Landberg, I L. Troen, and Erik Petersen. Atlas analysis and application program (wasp). 2, 01 1993.

NCAR/EOL. Perdigão field catalog - ncar/eol. http://catalog.eol.ucar.edu/perdigao. Accessed: 2018-06-10.

V. Nikora and D. Goring. Mars topography: bulk statistics and spectral scaling. *Chaos, Solitons Fractals*, 19(2):427 – 439, 2004. ISSN 0960-0779. doi: https://doi.org/10.1016/S0960-0779(03)00054-7. Fractals in Geophysics.

T.R. Oke. *Boundary Layer Climates*. Routledge, 1987. ISBN 9780415043199.

J.M.L.M. Palma, F.A. Castro, L.F. Ribeiro, A.H. Rodrigues, and A.P. Pinto. Linear and nonlinear models in wind resource assessment and wind turbine micro-siting in complex terrain. *Journal of Wind Engineering and Industrial Aerodynamics*, 96(12):2308 – 2326, 2008. ISSN 0167-6105. doi: https://doi.org/10.1016/j.jweia.2008.03.012.

S. Patankar. *Numerical Heat Transfer and Fluid Flow*. Series in computational methods in mechanics and thermal sciences. Taylor & Francis, 1980. ISBN 9780891165224.

S.V Patankar and D.B Spalding. A calculation procedure for heat, mass and momentum transfer in three-dimensional parabolic flows. *International Journal of Heat and Mass Transfer*, 15(10):1787 – 1806, 1972. ISSN 0017-9310.

N. Pineda, O. Jorba, J. Jorge, and J. M. Baldasano. Using noaa avhrr and spot vgt data to estimate surface parameters: application to a mesoscale meteorological model. *International Journal of Remote Sensing*, 2004.

Rodeo DTU. Online meteorological data - dtu wind energy. http://rodeo.dtu.dk. Accessed: 2018-06-10.

E. Rodriguez and J. M. Martin. Theory and design of interferometric synthetic aperture radars. *IEE Proceedings F - Radar and Signal Processing*, 139(2):147–159, April 1992. ISSN 0956-375X. doi: 10.1049/ip-f-2.1992.0018.

D. Santos, P. Costa, T. Simões, and A. Estanqueiro. Progress evaluation at portugal experimental test site - perdigão (preliminary version). *NEWA - Annual Report*, 2017.

R. Shaw and A. Pereira. Aerodynamic roughness of a plant canopy: a numerical experiment. *Agricultural Meteorology*, 1982.

J. Silva, C. Ribeiro, and R. Guedes. Roughness length classification of corine land cover classes. *MEGAJOULE - Consultants*, 2007.

A. Silva Lopes, J. M. L. M. Palma, and F. A. Castro. Simulation of the askervein flow. part 2: Large-eddy simulations. *Boundary-Layer Meteorology*, 125(1):85–108, Oct 2007. ISSN 1573-1472. doi: 10.1007/s10546-007-9195-4.

W.C. Skamarock, J Klemp, Jimy Dudhia, D.O. Gill, Dale Barker, W Wang, and J.G. Powers. A description of the advanced research wrf version 3. 27:3–27, 01 2008.

R.B. Stull. *An Introduction to Boundary Layer Meteorology*. Atmospheric and Oceanographic Sciences Library. Springer Netherlands, 1988. ISBN 9789027727688.

P. A. Taylor and H. W. Teunissen. The askervein hill project: Overview and background data. *Boundary-Layer Meteorology*, 39(1):15–39, Apr 1987. ISSN 1573-1472. doi: 10.1007/BF00121863.

N. Vasiljević, J. M. L. M. Palma, N. Angelou, J. Carlos Matos, R. Menke, G. Lea, J. Mann, M. Courtney, L. Frölen Ribeiro, and V. M. M. G. C. Gomes. Perdigão 2015: methodology for atmospheric multi-doppler lidar experiments. *Atmospheric Measurement Techniques*, 10(9):3463–3483, 2017. doi: 10.5194/amt-10-3463-2017. URL https://www.atmos-meas-tech.net/10/3463/2017/.

J. Vilaça. Analysis of Atmospheric Conditions, Data Quality, and Stationarity in Perdigão. Master's thesis, University of Porto, 2018.

J. Wieringa. Updating the davenport roughness classification. *Journal of Wind Engineering and Industrial Aerodynamics*, 1992.

WindsP. Windsp. https://perdigao.fe.up.pt. Accessed: 2018-06-10.

Y. Yamaguchi, A. B. Kahle, H. Tsu, T. Kawakami, and M. Pniel. Overview of advanced spaceborne thermal emission and reflection radiometer (aster). *IEEE Transactions on Geoscience and Remote Sensing*, 36(4):1062–1071, Jul 1998. ISSN 0196-2892. doi: 10.1109/36.700991.

Appendices

Appendix A

Roughness representation

Landscape	z_0 [m]	Description
Sea	0.0002	Open sea or lake (irrespective of the wave size), tidal flat, snow-covered flat plain, featurless deser, tarmac and concrete, with a free fetch of several kilometers.
Smooth	0.005	Featureless land surface without any noticeable obstacles and with negligible vegetation; e.g. beaches, pack ice without large ridges, morass, and snow-covered or fallow open country.
Open	0.03	Level country with low vegetation (e.g. grass) and isolated obstacles with separations of at least 50 obstacle heights; e.g. grazing land without windbreaks, heather, moor and tundra, runway area of airports.
Roughly open	0.10	Cultivated area with regular cover of low crops, or moderately open country with occasional obstacles (e.g. low hedges, single rows of trees, isolated farms) at relative horizontal distances of at least 20 obstacle helghts.
Rough	0.25	Recently-developed "young" landscape with high crops or crops of varying height, and scattered obstacles (e.g. dense shelterbelts, vineyards) at relative distances of about 15 obstacle heights.
Very rough	0.5	"Old" cultivated landscape with many rather large obstacle groups (large farms, clumps of forest) separated by open spaces of about 10 obstacle heights. Also low large vegetation with small interspaces, such as bushland, orchards, young densely-planted forest.
Closed	1.0	Landscape totally and quite regularly covered wlth similar-size large obstacles, wlth open spaces comparable to the obstacle heights; e,g, mature regular forests, homogeneous cities or villages.
Chaotic	≥ 2	Centres of large towns with mixture of low-rise and high-rise buildings. Also irregular large forests with many clearings.

Table A.1: Revised Davenport roughness classification.

Level 1	Level 2	Level 3
1. Artifical surfaces	11 Urban fabric	111 Continuous urban fabric 112 Discontinuous urban fabric
	12 Industrial, commercial and transport units	121 Industrial or commercial units 122 Road and rail networks and associated land 123 Port areas 124 Airports
	13 Mine, dump and costruction sites	131 Mineral extraction sites 132 Dump sites 133 Construction sites
	14 Artificial, non-agricultural vegetated areas	141 Green urban areas 142 Sport and leisure facilities
2. Agricultural areas	21 Arable lands	211 Non-irrigated arable land 212 Permanently irrigated land 213 Rice fields
	22 Permanent crops	221 Vineyards 222 Fruit trees and berry plantations 223 Olive grooves
	23 Pastures	231 Pastures
	24 Heterogeneous agricultural areas	241 Annual crops associated with permanent crops 242 Complex cultivation patterns 243 Land principally occupied by agriculture, with significant areas of natural vegetation 244 Agro-forestry areas
3. Forest and semi-natural areas	31 Forest	311 Broad-leaved forest 312 Coniferous forest 313 Mixed forest
	32 Scrub and/or herbaceous vegetation associations	321 Natural grasslands 322 Moors and heathland 323 Sclerophyllous vegetations 324 Transitional woodland-shrub
	33 Open spaces with little or no vegetation	331 Beaches, dunes, sands 332 Bare rocks 333 Sparsely vegetated areas 334 Burnt areas 335 Glaciers and perpetual snow
4. Wetlands	41 Inland wetlands	411 Inland marshes 412 Peat bogs
	42 Maritime wetlands	421 Salt marshes 422 Salines 423 Intertidal flats
5. Water bodies	51 Inland waters	511 Water courses 512 Water bodies
	52 Marine waters	521 Coastal lagoons 522 Estuaries 523 Sea and ocean

Table A.2: Corine Land Cover classes.

Appendix B

Terrain model

Slope

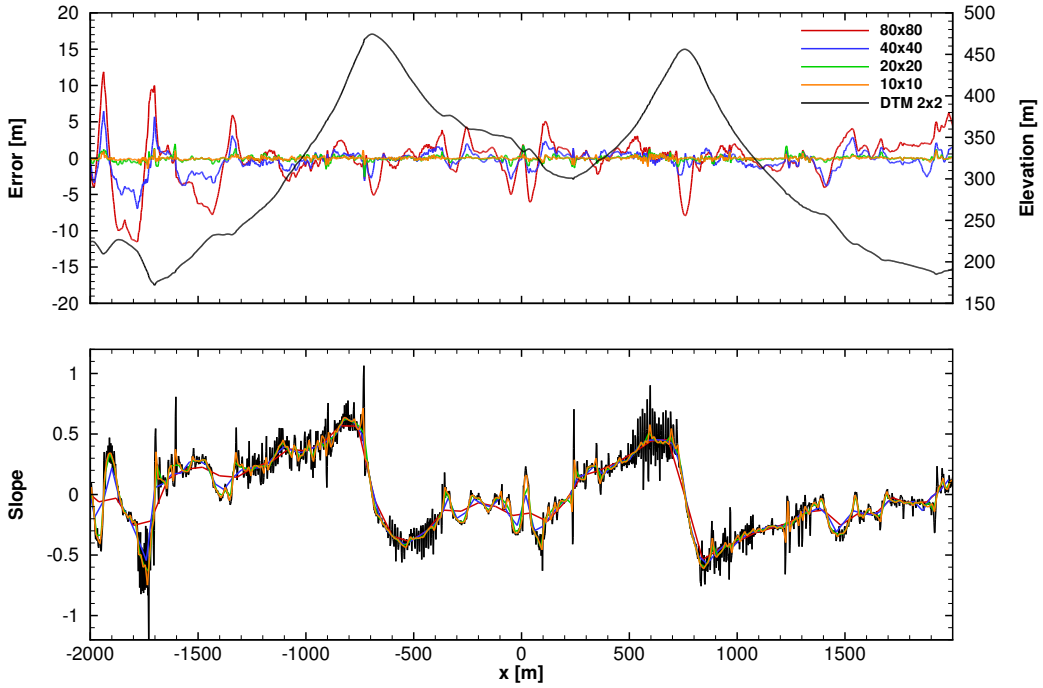

Figure B.1: Elevation and slope in the x direction profiles on a plane that contains Tower 25.

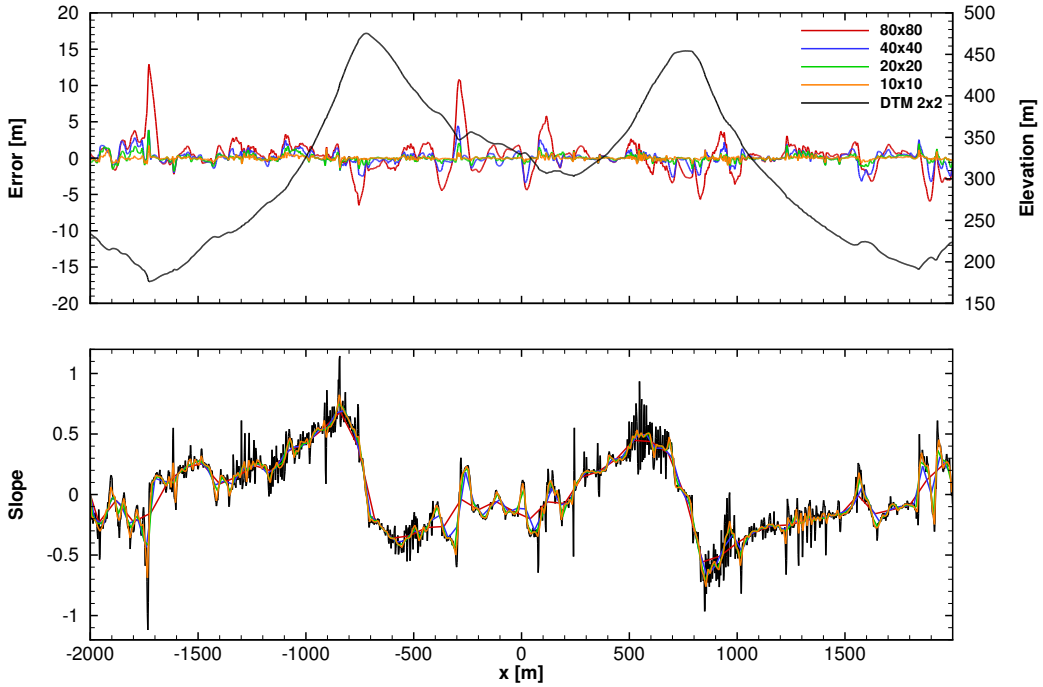

Figure B.2: Elevation and slope in the x direction profiles on a plane that contains Tower 29.

Code	Station	Coordinates[a] [m]		Elevation [m]			Elevation error [m]		
		Eastings	Northings	SRTM30	LiDAR	GPS	SRTM30-GPS	LiDAR-GPS	SRTM30-LiDAR
	TW12	34095.80	5717.10	419.26	421.23	421.54	-2.28	-0.31	-1.97
	TW13	34140.92	5777.09	389.97	384.62	383.90	6.07	0.72	5.35
	TW14	34222.77	5816.64	350.42	349.00	348.91	1.51	0.09	1.42
	TW15	34272.97	5843.29	331.97	330.30	330.50	1.47	-0.20	1.67
	TW20	33394.18	4258.87	469.95	472.99	472.74	-2.79	0.25	-3.05
	ZephIR 447	32379.29	4339.22	234.82	237.91	236.81	-1.99	1.10	-3.09
151	USA01	34409.80	5222.82	441.36	447.94	447.84	-6.48	0.10	-6.58
152	USA2	34008.00	5132.02	310.19	311.92	311.11	-0.92	0.81	-1.73
153	USA3	33419.47	5252.65	332.71	334.78	333.97	-1.26	0.81	-2.07
154	Sodar-RASS	34606.96	6117.91	255.83	260.08	258.45	-2.62	1.63	-4.25
155	MWR	34651.07	6170.54	257.92	260.27	259.83	-1.91	0.43	-2.35
157	Ceilometer	33922.69	5007.21	297.05	294.99	294.30	2.75	0.69	2.06
161	USA04	33907.88	5844.70	459.38	461.69	460.78	-1.40	0.91	-2.31
163	USA06	34491.89	6083.23	264.24	265.58	265.53	-1.29	0.06	-1.34
164	Scintillometer	34495.70	6076.55	263.11	262.43	268.00	-4.89	-5.57	0.69
165	Tethersonde	34462.56	6069.35	264.69	261.44	260.29	4.40	1.15	3.25
						MAX	6.07	1.63	5.35
						MIN	-6.48	-5.57	-6.58
						RMSE	3.24	1.58	3.09
						STDEV	3.26	1.62	3.06

Table B.1: Elevation data from the GPS topographic survey for some of the instrumentation and comparison with LiDAR and SRTM30 DEM.

[a]Coordinate system ETRS89 PT-TM06

Appendix C

Domain boundary positioning

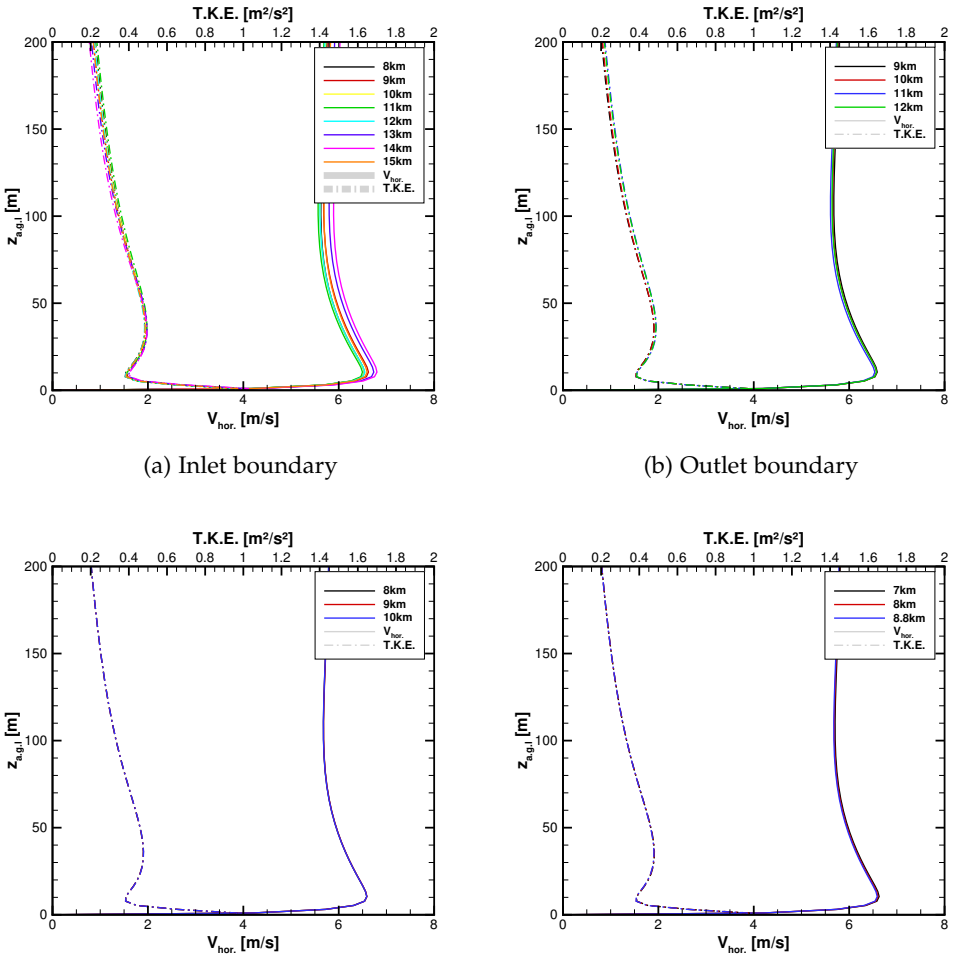

(a) Inlet boundary

(b) Outlet boundary

(c) Top boundary

(d) Bottom boundary

Figure C.1: Simulation results for different boundaries for SW winds, tower 20.

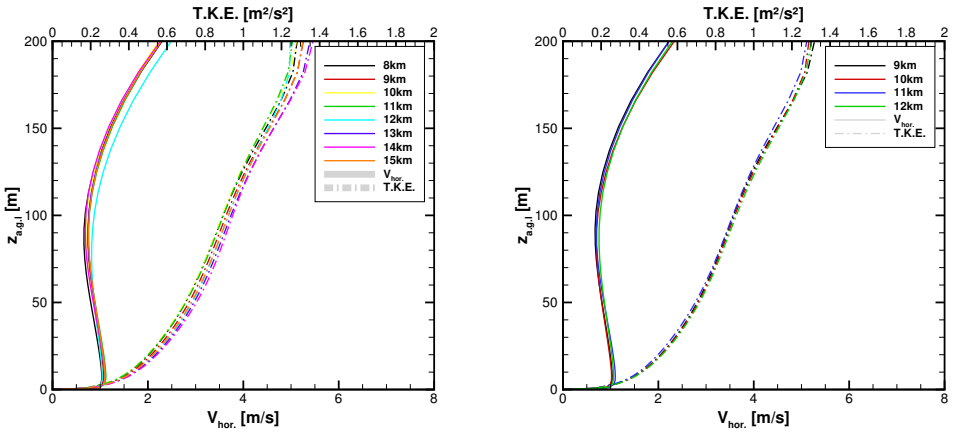

(a) Inlet boundary

(b) Outlet boundary

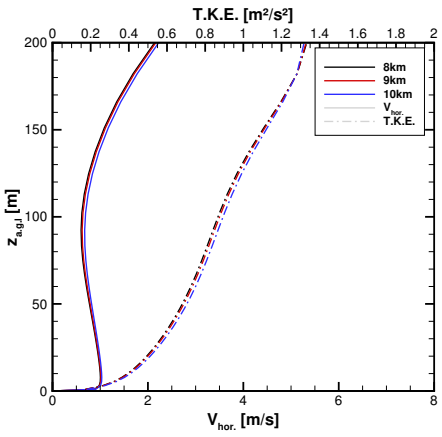

(c) Top boundary

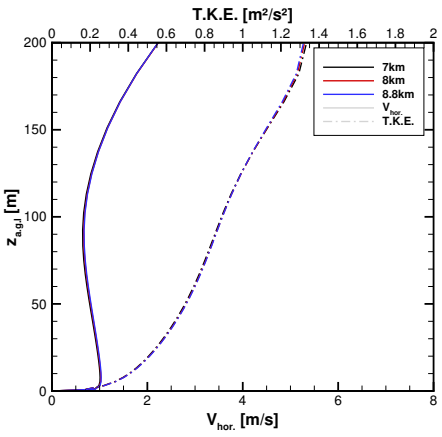

(d) Bottom boundary

Figure C.2: Simulation results for different boundaries for SW winds, tower 25.

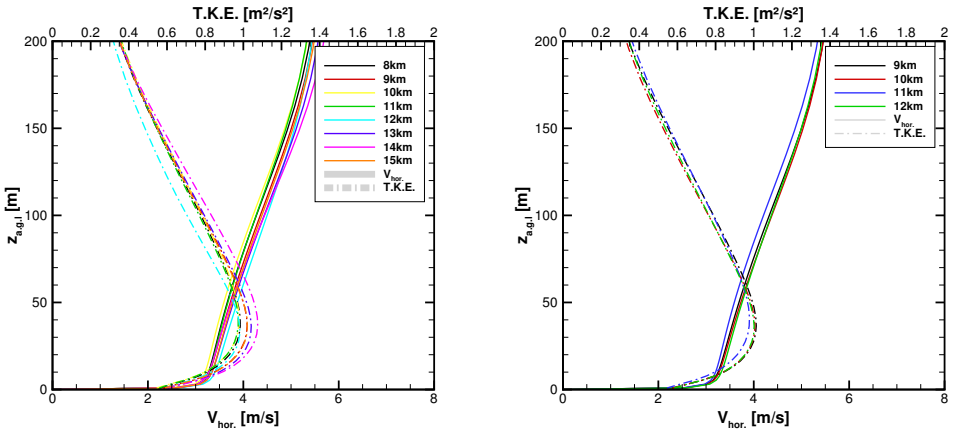

(a) Inlet boundary

(b) Outlet boundary

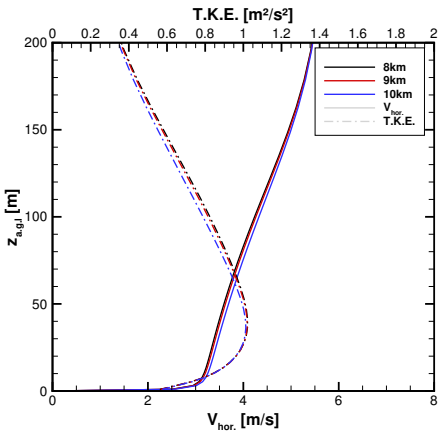

(c) Top boundary

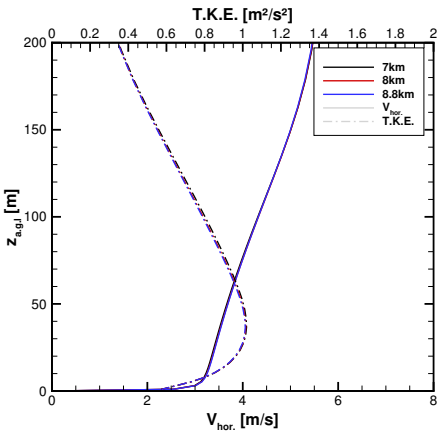

(d) Bottom boundary

Figure C.3: Simulation results for different boundaries for SW winds, tower 29.

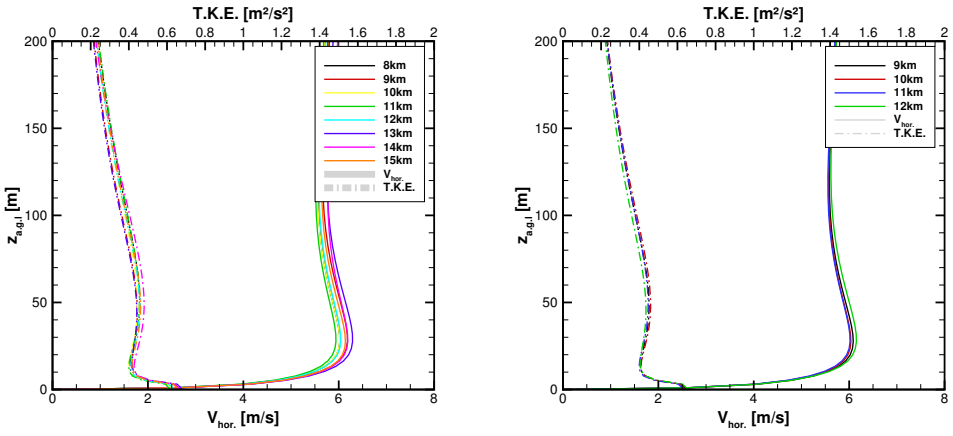

(a) Inlet boundary

(b) Outlet boundary

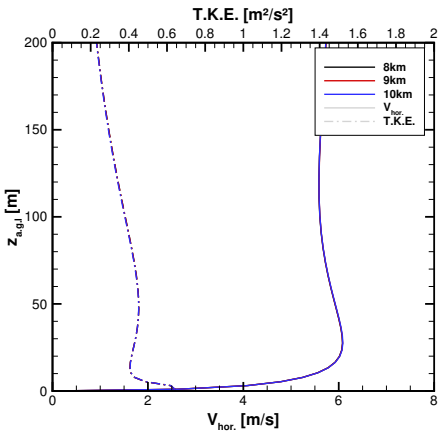

(c) Top boundary

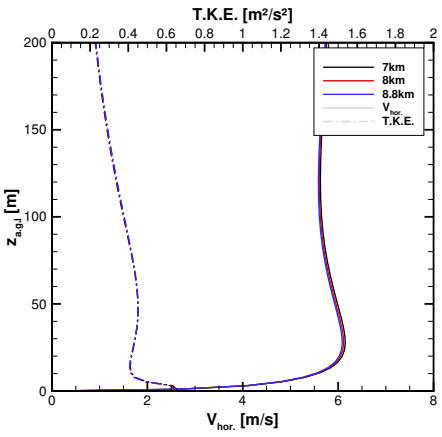

(d) Bottom boundary

Figure C.4: Simulation results for different boundaries for SW winds, tower 37.

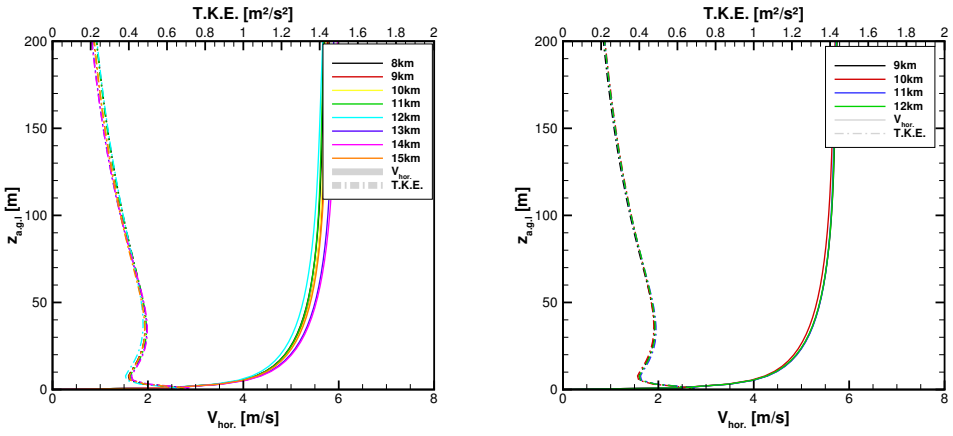

(a) Inlet boundary

(b) Outlet boundary

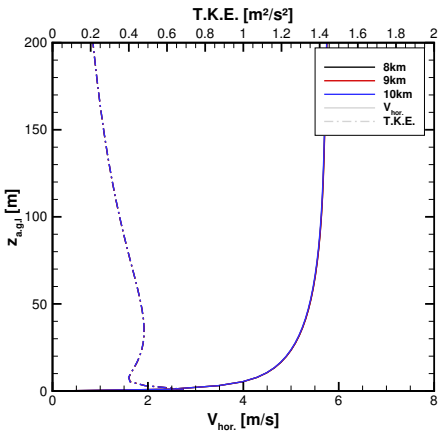

(c) Top boundary

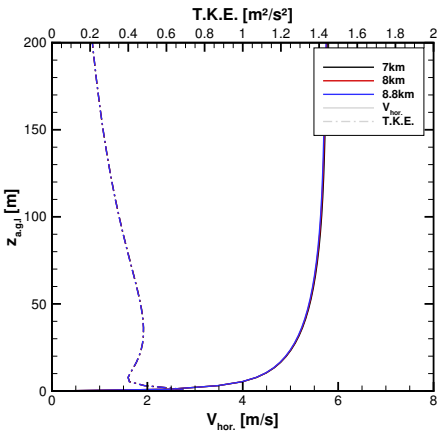

(d) Bottom boundary

Figure C.5: Simulation results for different boundaries for SW winds, wind turbine.

Appendix D

Simulation results for DTM comparison

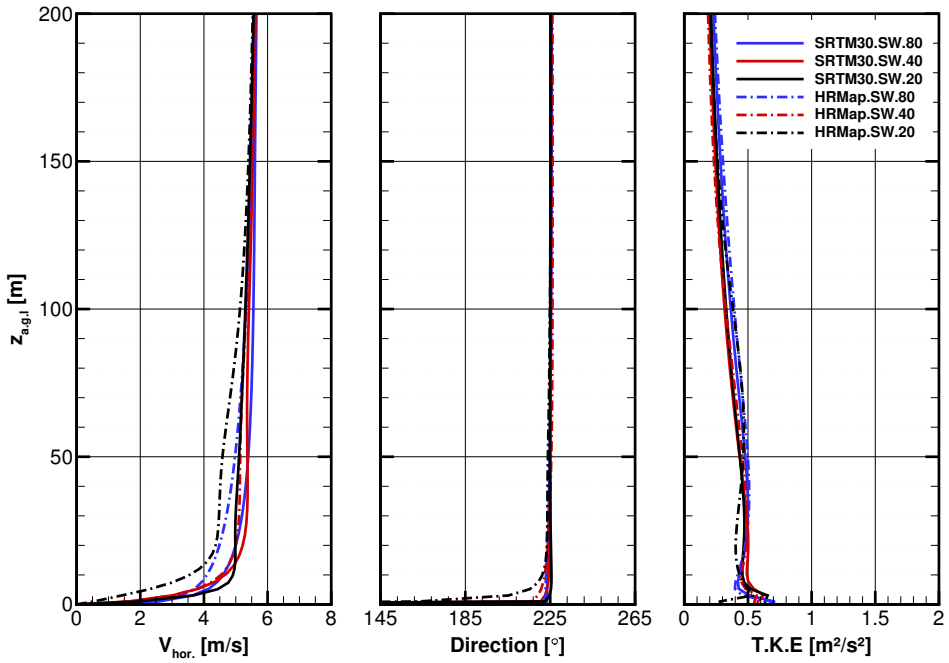

Figure D.1: Wind speed, direction and turbulent kinetic energy profile simulation results in the wind turbine for SW winds.

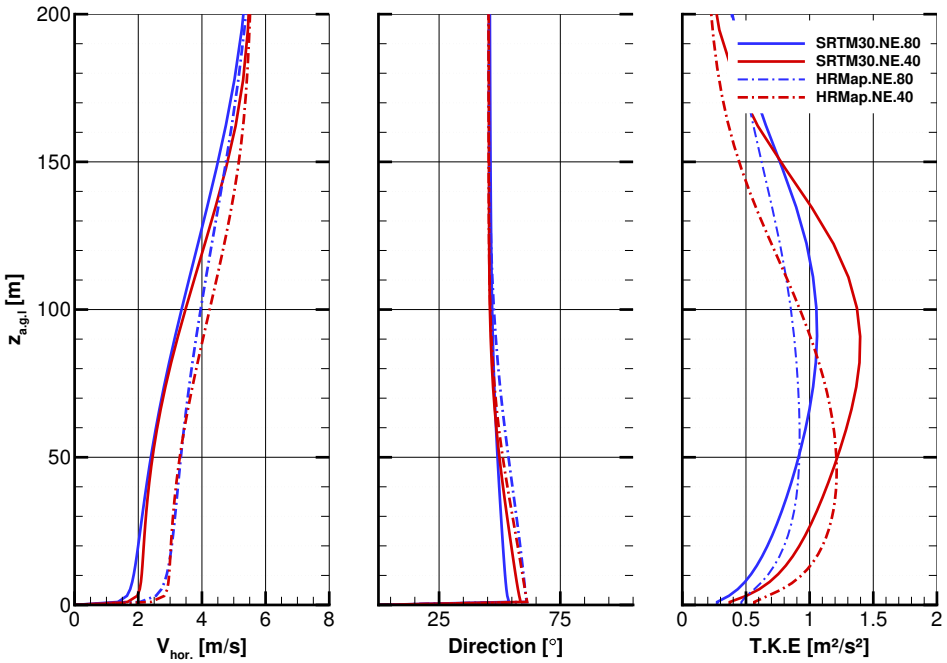

Figure D.2: Wind speed, direction and turbulent kinetic energy profile simulation results in the wind turbine for NE winds.

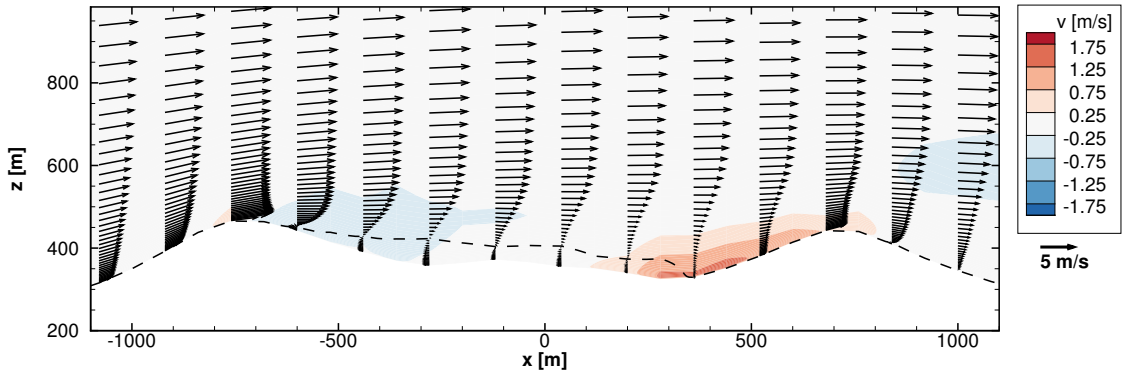

(a) 80x80

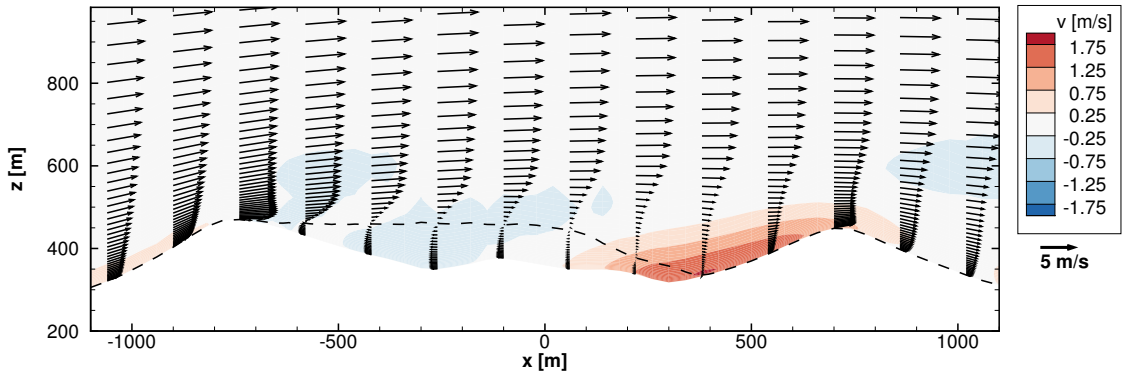

(b) 40x40

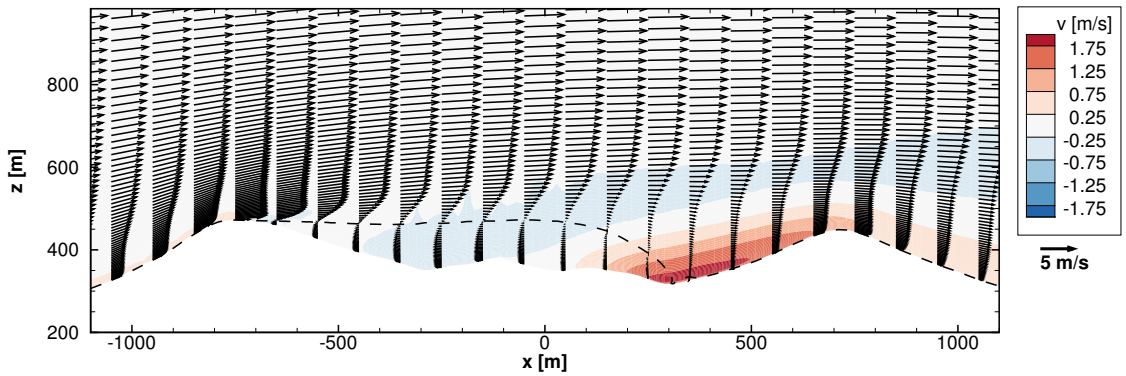

(c) 20x20

Figure D.3: Wind velocity profile along the double ridge (Tower 32).

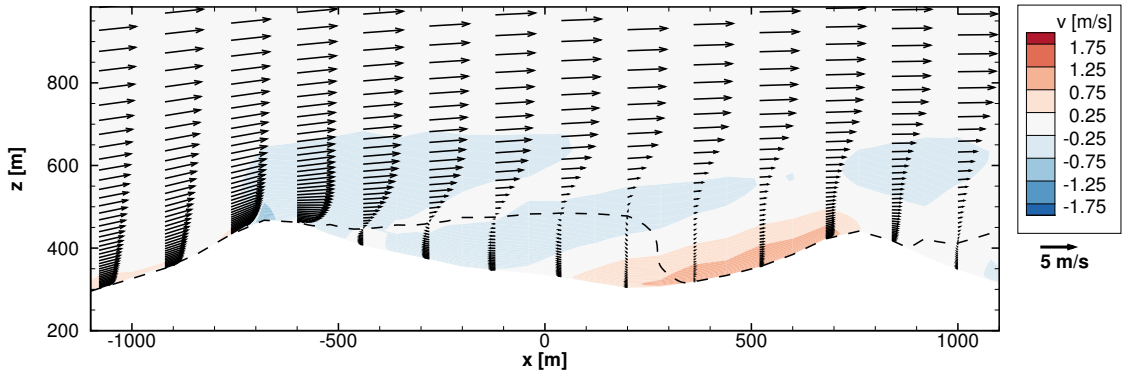

(a) 80x80

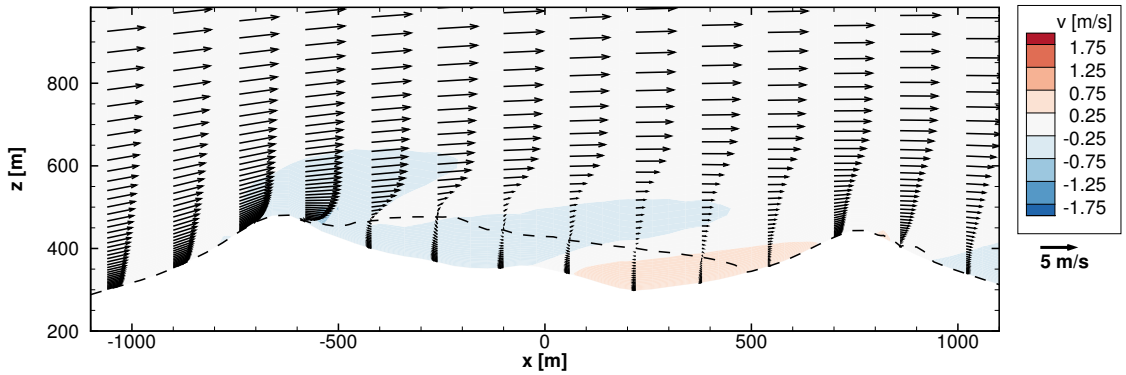

(b) 40x40

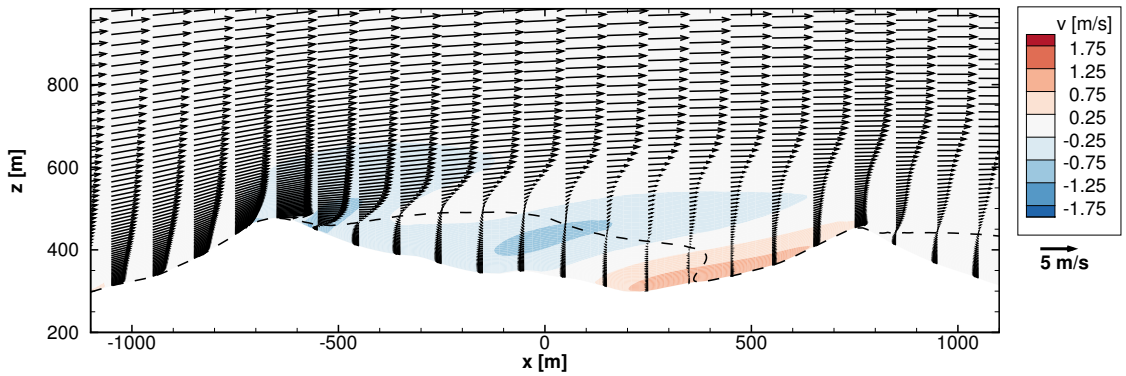

(c) 20x20

Figure D.4: Wind velocity profile along the double ridge (Tower 20).

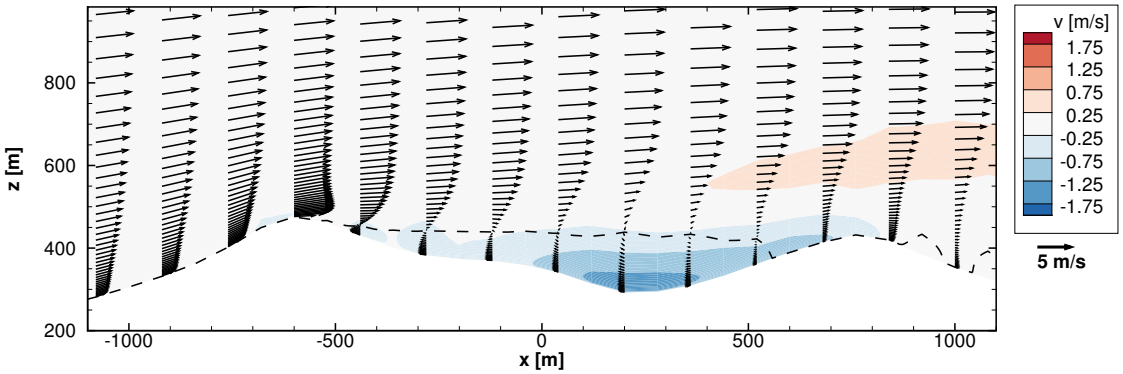

(a) 80x80

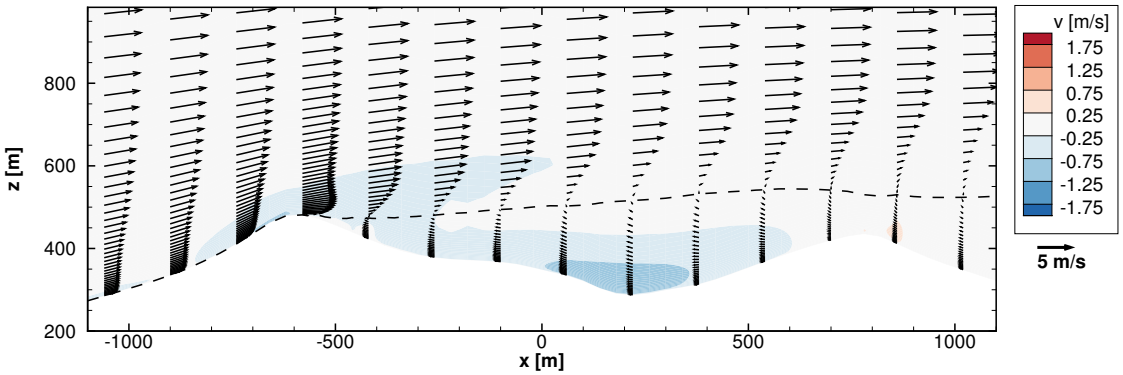

(b) 40x40

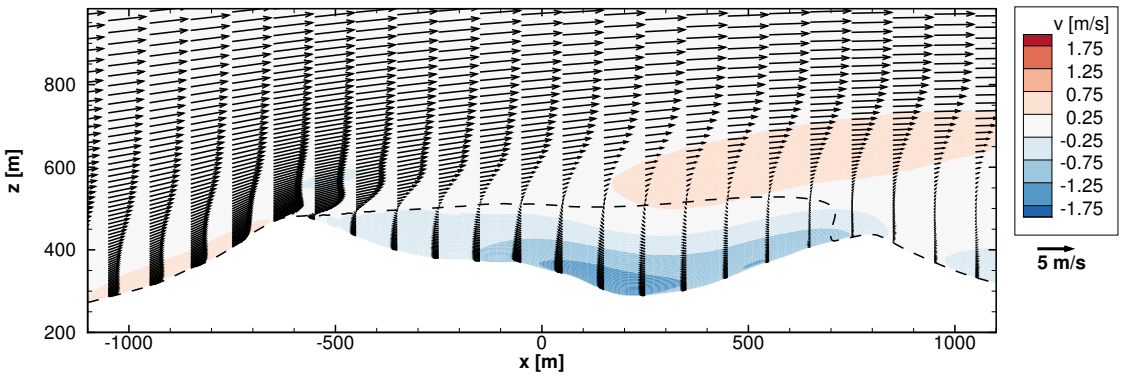

(c) 20x20

Figure D.5: Wind velocity profile along the double ridge (Tower 37).

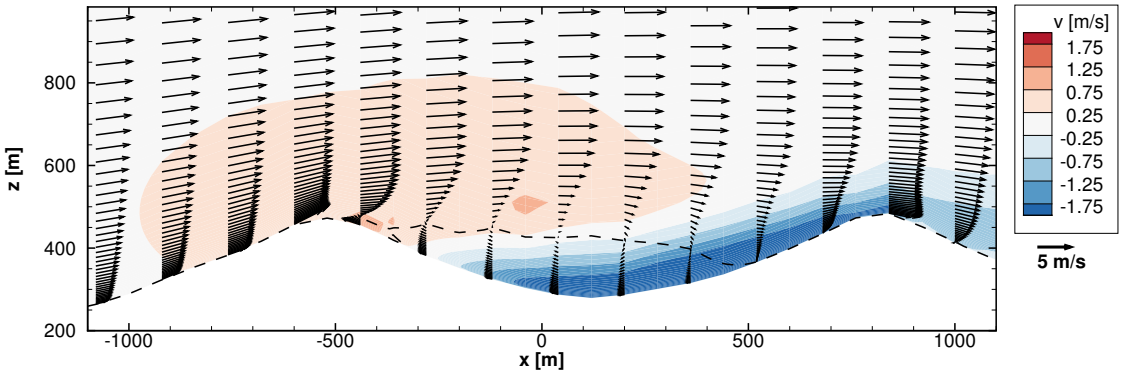

(a) 80x80

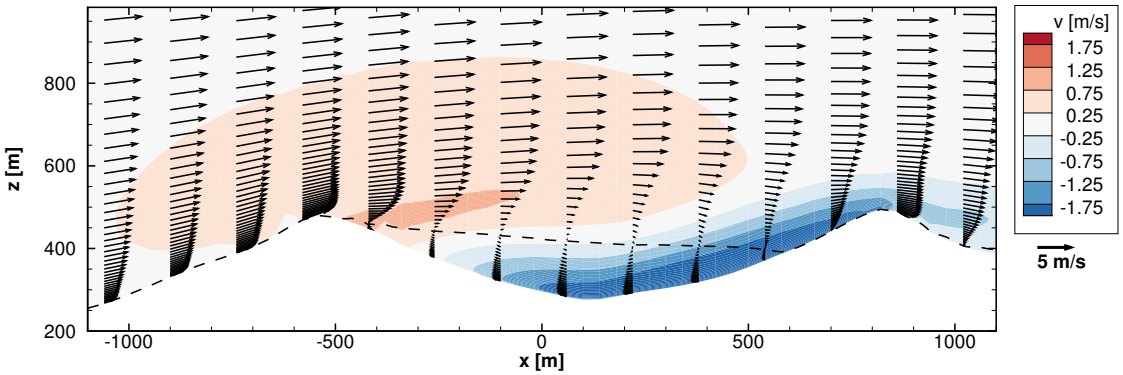

(b) 40x40

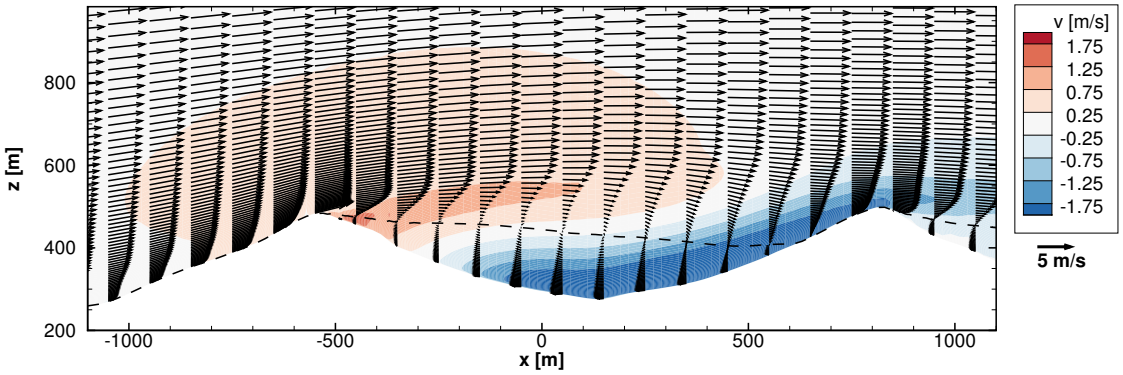

(c) 20x20

Figure D.6: Wind velocity profile along the double ridge (Tower 39).

Appendix E

Simulation results for surface cover model

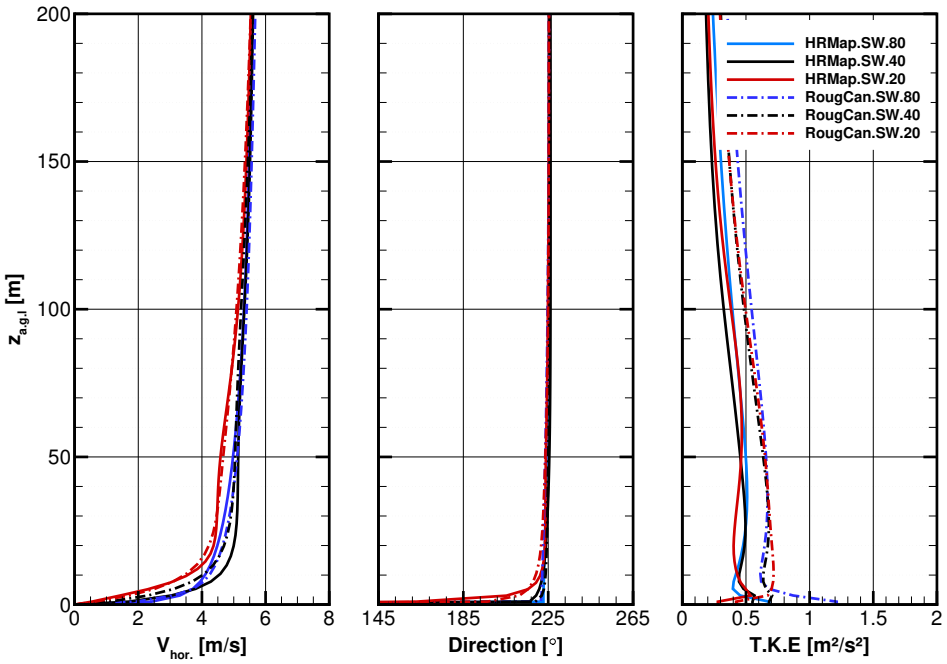

Figure E.1: Profile comparison with and without variable roughness for SW winds, wind turbine.

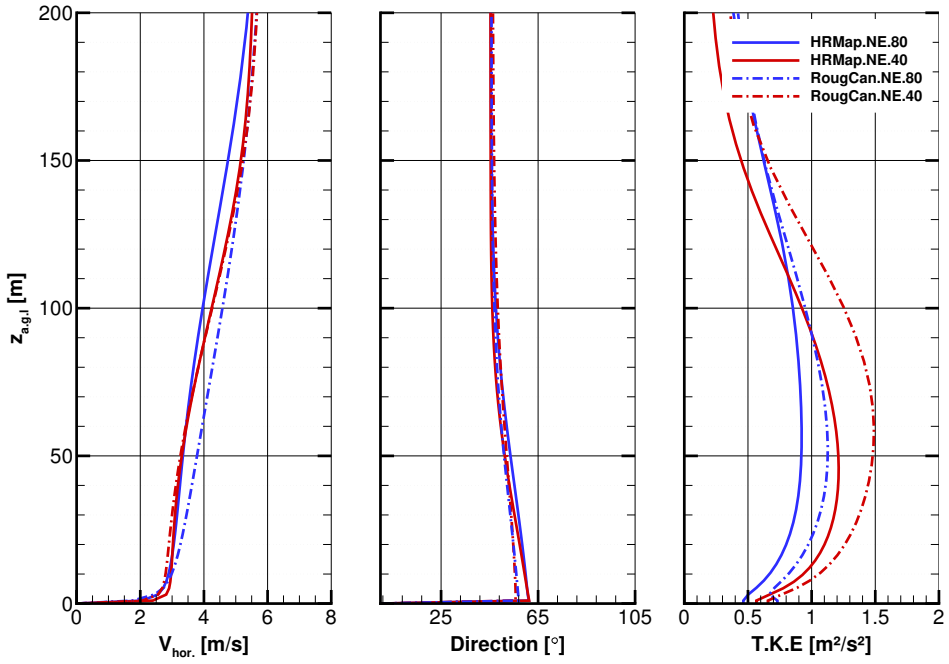

Figure E.2: Wind speed, direction and turbulent kinetic energy profile simulation results in the wind turbine for NE winds.

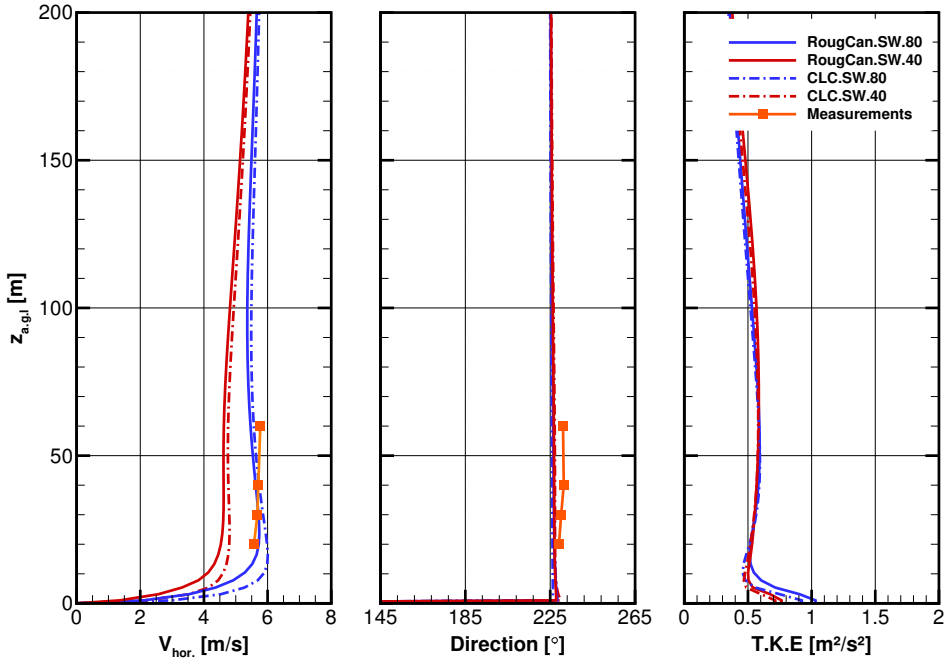

Figure E.3: Profile comparison between CLC and RougCan simulations for SW winds, tower 37.

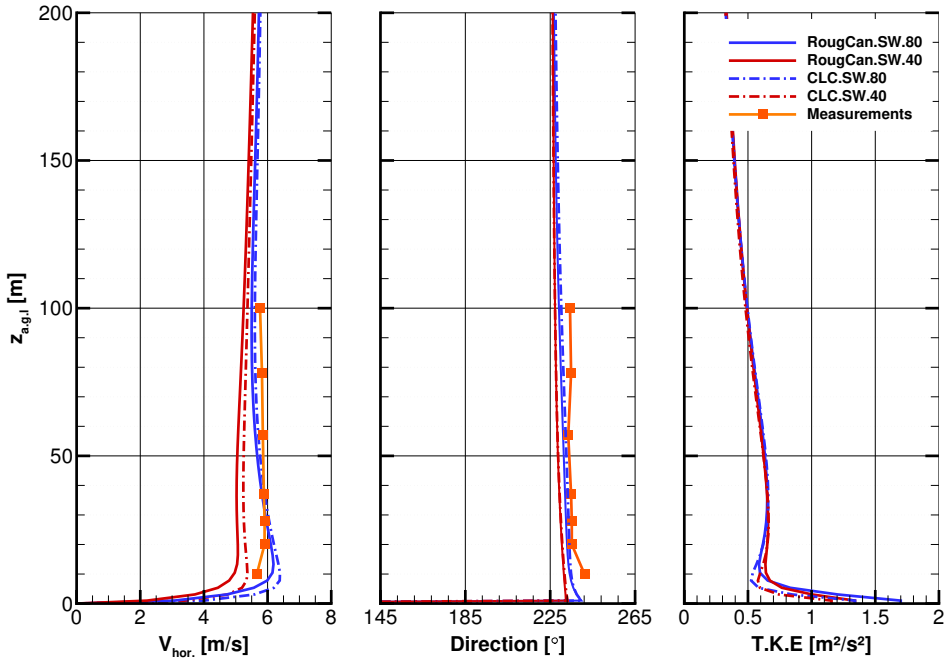

Figure E.4: Profile comparison between CLC and RougCan simulations for SW winds, tower 20.

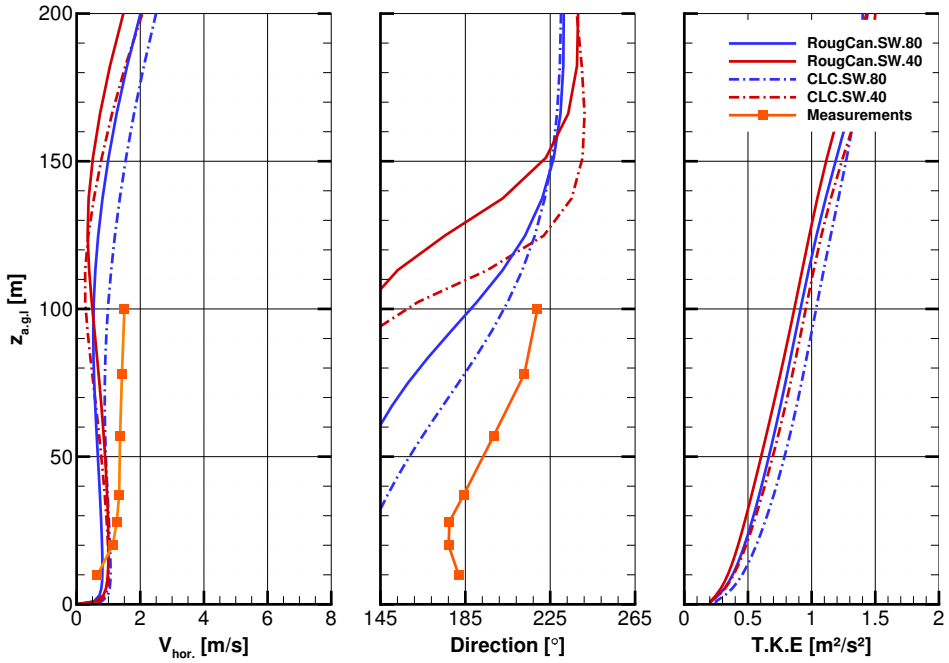

Figure E.5: Profile comparison between CLC and RougCan simulations for SW winds, tower 25.

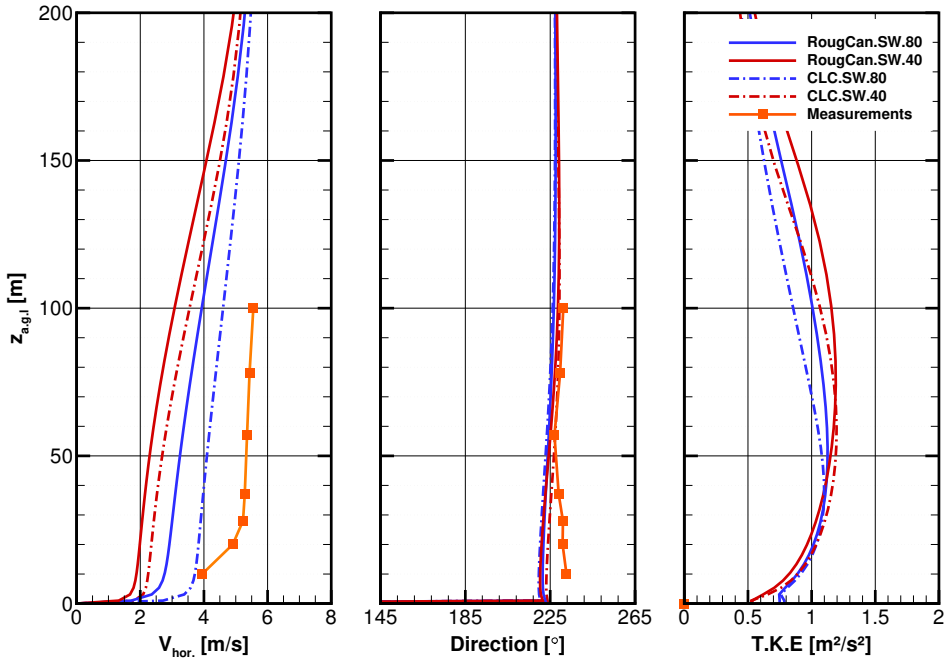

Figure E.6: Profile comparison between CLC and RougCan simulations for SW winds, tower 29.

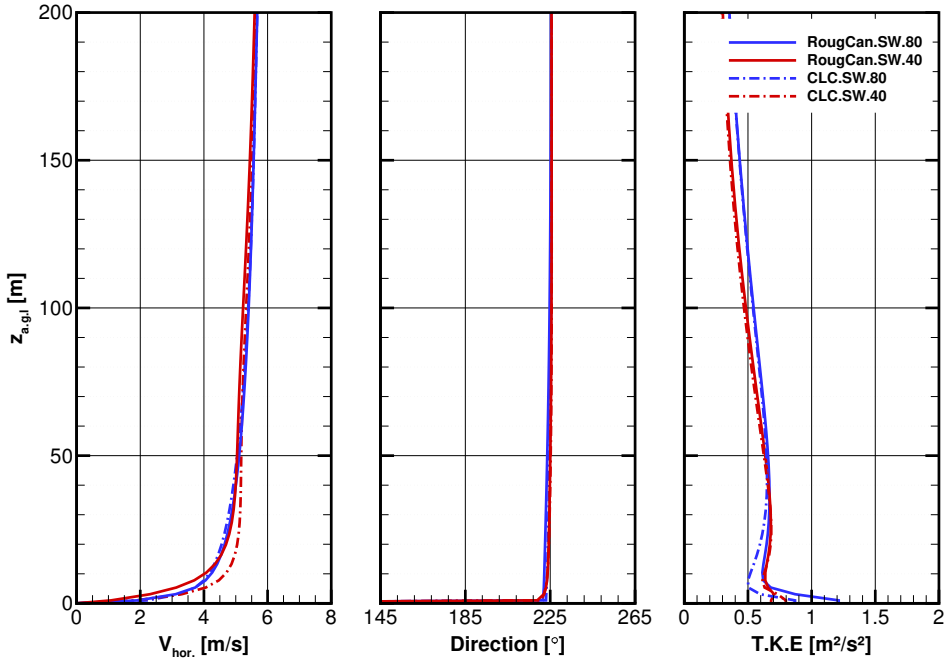

Figure E.7: Profile comparison between CLC and RougCan simulations for SW winds, wind turbine.

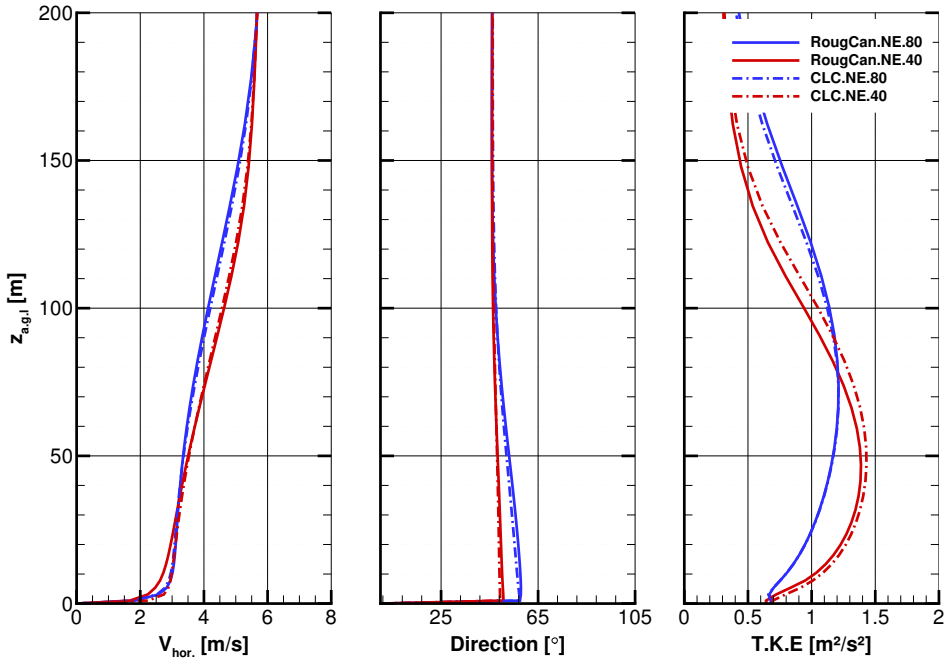

Figure E.8: Profile comparison between CLC and RougCan simulations for NE winds, tower 37.

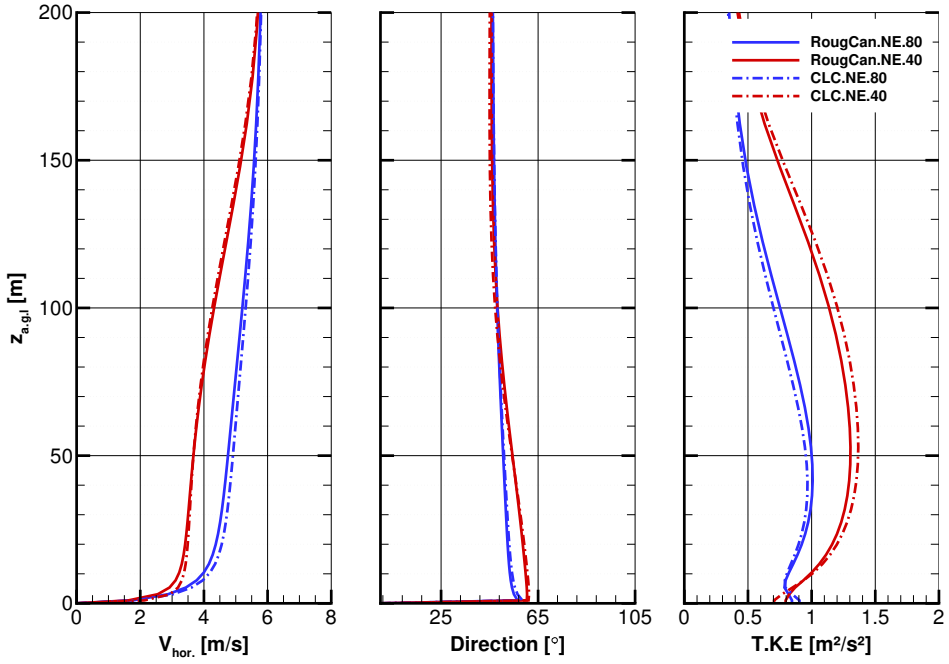

Figure E.9: Profile comparison between CLC and RougCan simulations for NE winds, tower 20.

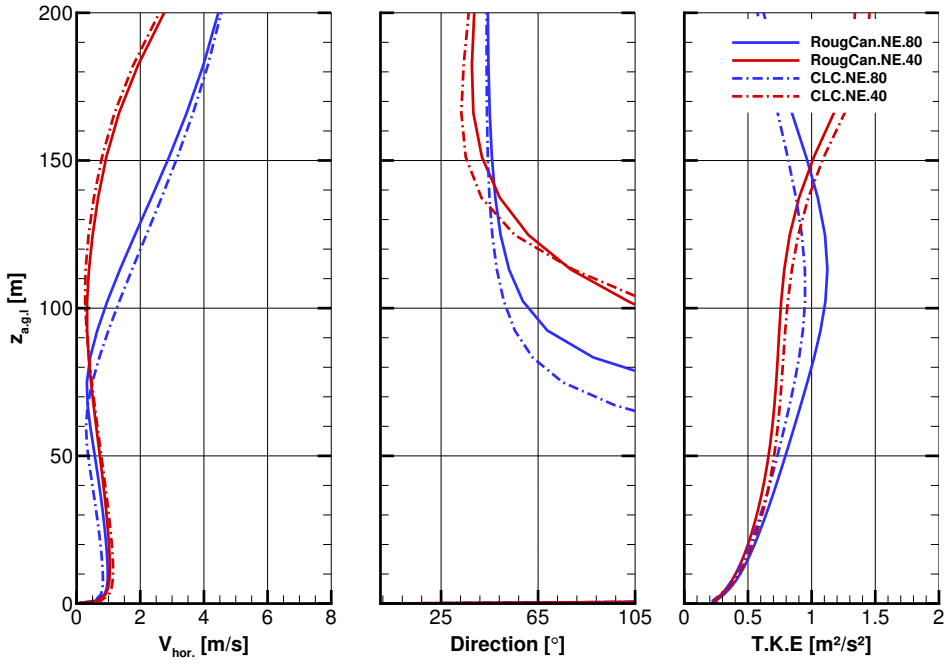

Figure E.10: Profile comparison between CLC and RougCan simulations for NE winds, tower 25.

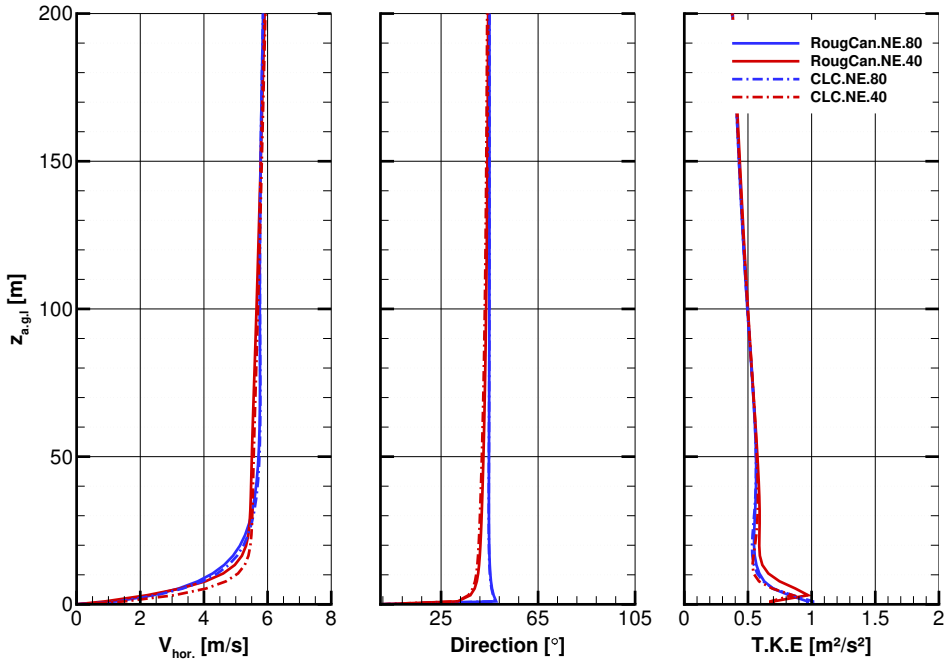

Figure E.11: Profile comparison between CLC and RougCan simulations for NE winds, tower 29.

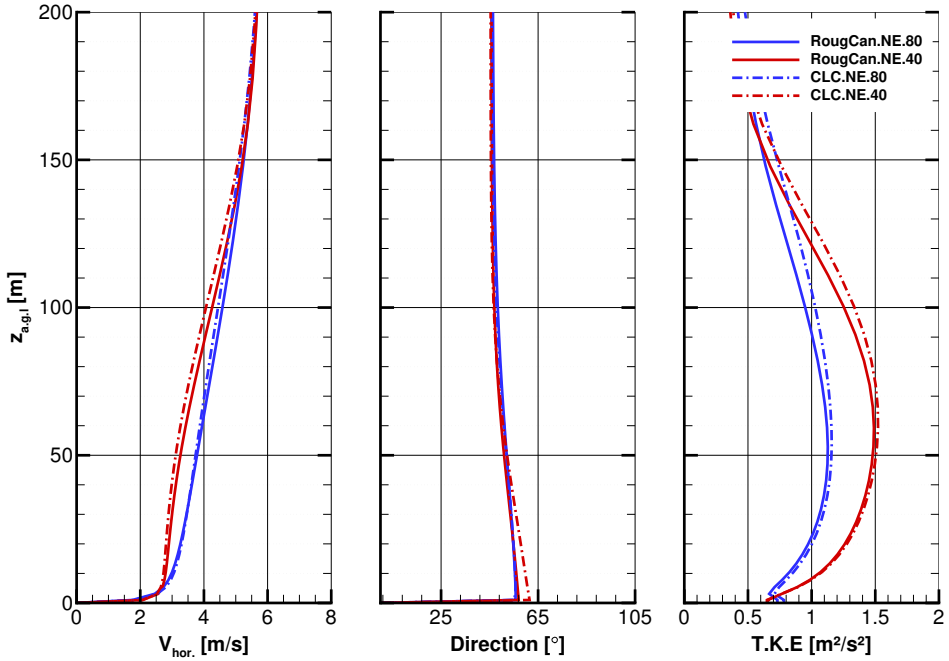

Figure E.12: Profile comparison between CLC and RougCan simulations for NE winds, wind turbine.